THESIS FOR THE DEGREE OF DOCTOR OF PHILOSOPHY

Strong Light-Matter Interactions and Formation of Hybrid States at the Nanoscale

MARTIN WERSÄLL

Department of Physics

CHALMERS UNIVERSITY OF TECHNOLOGY

Göteborg, Sweden 2018

Strong Light-Matter Interactions and Formation of Hybrid States at the Nanoscale

MARTIN WERSÄLL

Department of Physics

Chalmers University of Technology

SE-412 96 Göteborg

Sweden

Telephone +46 (0)317721000

E-mail: martinwersall@gmail.com

Cover:
(Left): Graphic inelastic relaxation scheme in plasmon-exciton hybrid structures. (Down): Dark-field scattering and photoluminescence spectra of both uncoupled and coupled nanoscale systems. (Upper): Graphic sketch of a hybrid system pumped with photons of different energies, together with indications of temperature alterations and lifetime measurements. (Lower Right): Graphic sketch of a silver nanoprism on top of a sheet of J-aggregated TDBC dye molecules. (Upper Right): Graphic sketch of the population decay in both weakly- and strongly coupled cavity-emitter systems.

Strong Light-Matter Interactions and
Formation of Hybrid States at the Nanoscale

Martin Wersäll

Department of Physics

Chalmers University of Technology

Abstract

Noble metallic nanoparticles, which support *localized surface plasmon resonances (LSPR)*, offer a variety of potential scientific and industrial utilizations. Due to their remarkable ability to confine light at nanoscale dimensions, far below the optical diffraction limit, plasmonic nanoparticles enable intricate light manipulations, which may be performed and exploited for a wide range of future revolutionary applications.

For instance, LSPR in noble metal nanoparticles may be coupled to and coherently interact with exciton resonances in semiconducting nanocrystals and/or dye molecules. If the coupling strength is strong enough it is possible to create nanoscale systems, which support a new type of hybrid excitations. These excitations cannot be thought of as neither plasmonic nor excitonic, but rather an indistinguishable mixture of both. These type of excitations need to be considered as being half-light/half-matter entities and may be treated as quasiparticles, referred to as polaritons. Such quasiparticles have shown to possess properties, which open up completely new routes toward light manipulation at the nanoscale and have recently attracted tremendous attention and interest within the scientific nano-optics and nano-photonics communities.

The subject of this thesis is to both experimentally and theoretically demonstrate strong light-matter interactions in isolated single particle nanoscale plasmon-exciton systems, as well as discussing possible applications. The systems described and presented in this thesis are composed of single crystalline Ag nanoprisms attached to J-aggregated dye molecules, as well as Ag nanoprisms coupled to excitons in 2D material *transition metal dichalcogenides (TMDC)* monolayers. The experimental results presented in this thesis support promising outlooks for future plasmonic molecular manipulations as well as room temperature quantum plasmonics and quantum optics.

Keywords: *localized surface plasmon resonances, strong coupling, coherent interactions.*

APPENDED PAPERS

The following publications are included in this thesis:

Paper I:
Realizing Strong Light-Matter Interactions between Single-Nanoparticle Plasmons and Molecular Excitons at Ambient Conditions

G. Zengin [1], **M. Wersäll** [1], S. Nilsson, T. J. Antosiewicz, M. Käll and T. Shegai
Physical Review Letters **2015**, 114, 157401

[1] Shared 1st authors.

Paper II:
Observation of Mode Splitting in Photoluminescence of Individual Plasmonic Nanoparticles Strongly Coupled to Molecular Excitons

M. Wersäll, J. Cuadra, T. J. Antosiewicz, S. Balci, and T. Shegai
Nano Letters **2016**, 17 (1), 551-558

Paper III:
Inelastic Relaxations and Thermal Properties in Strongly Coupled Plasmon-Exciton Hybrid Nanostructures

M. Wersäll, B. Munkhbat, J. Cuadra, D. G. Baranov, T. J. Antosiewicz, and T. Shegai
Manuscript **2018**

Paper IV:
Suppression of Photo-Oxidation of Organic Chromophores by Strong Coupling to Plasmonic Nanoantennas

B. Munkhbat, **M. Wersäll**, D. G. Baranov, T. J. Antosiewicz, and T. Shegai
Science Advances **2018** *(Accepted)*

Paper V:
Observation of Tunable Charged Exciton Polaritons in Hybrid Monolayer WS_2 - Plasmonic Antenna System

J. Cuadra, D. G. Baranov, **M. Wersäll**, R. Verre, T. J. Antosiewicz, and T. Shegai
Nano Letters **2018,** 18, 1777-1785

My contributions:

Paper I:

I am noted as an equal contributor to G. Zengin in this work. I helped devising the experimental measurement concept, as well as establishing a method for fabricating the nanoscale hybrid structures. Together with G. Zengin, I collected and analyzed all spectral and SEM experimental data. Finally, I co-wrote the final manuscript.

Paper II:

I acted as a project leader, devising the concept of measuring both photoluminescence and dark-field scattering at low temperatures from a sample inside the cryostat chamber. I collected and analyzed all spectral and SEM experimental data. I co-wrote the final manuscript.

Paper III:

I acted as a project leader, devising the concept of measuring both photoluminescence and dark-field scattering at low temperatures from a sample inside the cryostat chamber. I collected and analyzed all spectral and SEM experimental data. I am the only author to this manuscript.

Paper IV:

I assisted B. Munkhbat with experimental measurement techniques, collected and analyzed a substantial part of the experimental data, and participated in establishing the theoretical framework, which explains the physical dynamics within this study. Moreover, I co-wrote the final manuscript.

Paper V:

I assisted J. Cuadra with initial optical measurements as well as, producing the nanoprisms structures within this study. Moreover I performed theoretical simulations on excitation populations for different polariton branches, with a self-designed theoretical framework. I furthermore co-wrote parts of the final manuscript.

NOT APPENDED PAPERS

The following works were published during my doctoral studies but are not included in this thesis:

Paper VI:

Universal Method for Realization of Strong Light-Matter Coupling Using Oscillator Strength Borrowing in Microcavity-Plasmon-Exciton Systems

A. Bisht, J. Cuadra, **M. Wersäll**, A. Canales, and T. Shegai
Submitted **2018**

Paper VII:

Hybrid Dielectric Waveguide Spectroscopy of Individual Plasmonic Nanoparticles

J. Cuadra, R. Verre, **M. Wersäll**, C. Krückel, V. Torres-Company, T. J. Antosiewicz, and T. Shegai
AIP Advances **2017**, 7, 075207.

Paper VIII:

Novel Nanostructures and Materials for Strong Light-Matter Interactions
D. G. Baranov, **M. Wersäll**, J. Cuadra, T. J. Antosiewicz, and T. Shegai
ACS Photonics **2018**, 5, 24-42.

Paper IX:

Directional Nanoplasmonic Antennas for Self-Referenced Refractometric Molecular Analysis

M. Wersäll, R. Verre, M. Svedendahl, P. Johansson, M. Käll and T. Shegai
The Journal of Physical Chemistry C **2014**, 118, 36, 21075-21080.

Contents

Chapter 1

Introduction

The interaction between light and matter has been a source of mystery and excitement for humans throughout history. Our perception of the surrounding environment as well as numerous processes in nature depend heavily on light-matter interactions and evolution has accordingly shaped much of the world around us. One of the first recorded attempts in developing a theory to describe the underlying dynamics of light-matter interactions was made already in ancient Greece by the pre-Socratic philosopher Empedocles (490-430 BC) [1]. Even though theories have advanced and progressed during the elapse of time, some aspects regarding the fundamental nature of light, and hence light-matter interactions, is still a subject for debate within the scientific community.

Ever since the birth of quantum mechanics in the beginning of the 20th century, scientists have been able to deduce theoretical outcomes, which matches optical experimental observations in an astoundingly satisfying manner. This has resulted in many modern day essential technical inventions such as lasers, light-emitting diodes (LEDs) and photovoltaics [2-4]. Despite these immense progresses there is still a plethora of problems related to understanding the quantum reality of light and its interaction with matter. One example is the fundamental interpretation of quantum entanglement [5]. Even though there is sufficient theoretical understanding to predict outcomes on this matter, the true underlying mechanism is still a question of debate [6].

Since visible light has wavelengths in the range of 390-700 nanometers it was previously widely regarded a mere impossibility to focus light to spatial dimensions much smaller than the resolution limit, dictated by 19th century physicist Ernts Abbe [7]. Much of this changed with the discovery and introduction of *localized surface plasmon resonances (LSPR)*, where visible light couples strongly to collective oscillations of surface charge densities in nanoscale entities of noble metals [8]. The discovery of surface plasmons eventuated in completely new possibilities to affect and manipulate light at spatial nanoscale dimensions. In addition, the surface charge density oscillations associated with surface plasmons at the interface, between the metal and the dielectric environment, leads to strongly enhanced optical evanescent fields [9]. This makes their optical properties highly susceptible to minute alterations in the local dielectric environment, a very crucial point for light manipulation [10]. As a result,

completely new scientific research fields within optics and nanotechnology emerged. Thus, several new ideas on how to for example exploit light-matter interactions to achieve efficient energy harvesting [11], molecular sensing [12] and new and intriguing nano-optics [13], were established and reported.

Ever since the discovery of surface plasmons there has been an immense progress in nanofabrication and sample manufacturing. For instance, techniques such as electron-beam lithography [14], hole-mask colloidal lithography [15] and/or drop-casting colloidal nanoparticles suspended in solutions on to a substrate [16], give the ability to create macroscopic surfaces composed of a multitude of separated distinct high-quality nanoscale structures.

A phenomenon in nano-optics and nano-photonics, which has recently gained a lot of attention and recognition, is *plasmon-exciton strong coupling*. What this term refers to is the situation where a plasmonic particle (which in many aspects can be thought of as an optical resonant cavity) and quantum emitters (molecules, quantum dots etc.), under right conditions are able to exchange energies on a time scale faster than any other dissipation or decoherence processes within the system. As a result the energy will oscillate back and forth between the cavity and emitter(s) several times before it finally decays to the surrounding environment [17]. These type of oscillations are generally referred to as vacuum Rabi oscillations, and is one of the most crucial parameters to extract in order to quantify the coupling strength within such nanoscale systems. When systems possess this ability they are generally referred to as *hybrid structures*, since the supported excitations is now hybridized and shared between the modes of both cavity and emitter(s). This phenomenon is vastly different from the case of weak coupling, where the so-called *Purcell effect* governs and alters the cavity-emitter dynamics. In the case of weak coupling, a one-way energy transfer from cavity to emitter is present rather than Rabi oscillations, which leads to further modifications in the spontaneous decay rate of the emitter [18].

Recent studies have demonstrated strong coupling mainly on an ensemble level of particles and molecules, or in various nanoparticle arrays or assemblies coupled to a large number of excitons [19, 20]. Even though there have been a few demonstrations of strong light-matter interactions at the single-particle level [21-23], there still remain ambiguities in the interpretation of plasmon-exciton interactions present within these studies. From a quantum optical perspective this indicates an uncertainty in the number of excitons involved in the interactions, as well as a question if plasmonic structures are capable of realizing strong light-

matter interactions at its fundamental limit. Since questions of this kind are essential to address for future quantum optics applications, it is of great importance that these aspects are investigated further [24, 25].

Utilizing plasmonic nanoparticles as resonant optical cavities opens up promising expectations for quantum optical systems, operating at room temperatures [26, 27]. In addition, strongly coupled nanoscale systems might be possible candidates in future quantum information processing networks [28-30], quantum cryptography [31] and ultrafast single-photon switches [32] to name a few. This indicates that nanoscale hybrid systems will perhaps play a key role to push the society into a whole new scientific/technical/sustainable era.

In this thesis theoretical derivations as well as experimental observations of strong light-matter interactions in single isolated plasmonic nanoscale structures are presented and discussed.

To begin with, in Chapter 2 the most fundamental aspects of coherence, which is an essential ingredient in light-matter interactions, are presented and discussed.

Thereafter, Chapter 3 deals with basic phenomena such as plasmonic resonances in metal nanoparticles as well as molecular resonances and excitonic resonances in semiconducting nanocrystals (quantum dots), as well as in molecular aggregates. Several core concepts in the field of nano-photonics and plasmonics are derived, presented and discussed to give the reader a fundamental introduction to this research field.

In Chapter 4, which is one of the main chapters of this thesis, the concepts and underlying dynamics of strong plasmon-exciton coupling mechanisms are addressed. This will be the most extensive chapter within this thesis, presenting various theoretical frameworks on how to perceive the phenomenon of strong coupling from various viewpoints, all from a purely classical to purely quantum mechanical approaches.

Since the studies, on which the content of this thesis are based on, are experimental different methods on how to fabricate suitable nanostructures as well as quantifying their optical properties, together with imaging nanostructures in a scanning electron microscopy (SEM), are thoroughly described and presented within Chapter 5.

Finally in Chapter 6, sections including a summary of the thesis content as well as some future outlooks for this research field will be presented and discussed.

An appendix with the specific scientific publications, on which the content of this thesis is based, can be found at the end. The reader can turn to this section for more detailed information regarding the topic of interest.

Chapter 2

Coherent Interactions between Dipole Emitters

The term coherence stems from the Latin word *cohaerens*, which approximately means, "*to unite*" [33]. In the case of electromagnetism it refers to correlations of certain properties between two different electromagnetic fields, and is mathematically quantified by the so-called *cross-correlation function* [34]. More generally optimal coherence implies constant intrinsic and spatial phase difference, as well as the requirement that waves emitted from different sources acquire the same frequency. The notion of coherence can be generalized further to encapsulate a wide range of concepts such as microscopic quantum states within the framework of quantum mechanics.

2.1 Radiated intensity from numerous coherently emitting dipoles

The total radiation pattern from numerous emitting oscillating dipoles can be derived by imposing the so-called *superposition principle* [7]. Within this framework, the total radiated intensity from N coherently emitting oscillating dipoles may be expressed according to the relation

$$I_{tot} \sim \left| \sum_{i=1}^{N} \boldsymbol{p}_i \right|^2 = \sum_{i=1}^{N} |\boldsymbol{p}_i|^2 + \sum_{i=1}^{N-1} \sum_{j=i+1}^{N} 2|\boldsymbol{p}_i||\boldsymbol{p}_j| \cos(\boldsymbol{k} \cdot \boldsymbol{R}_{ij} + \Delta\varphi_{ij}) \qquad (2.1)$$

Here $\boldsymbol{p}_{i,j}$ refers to the complex dipole moment vector of sources located at points in space with indices i and j, $|\boldsymbol{k}| = \frac{2\pi}{\lambda}$ and $\boldsymbol{R}_{ij} = \boldsymbol{R}_i - \boldsymbol{R}_j$ is a vector, which magnitude and direction corresponds to the distance and direction between these dipole sources. The corresponding intrinsic phase difference between dipoles p_i and p_j can be written as

$$\Delta\varphi_{ij} = \arctan\left(\frac{Re\{p_i\}Im\{p_j\} - Re\{p_j\}Im\{p_i\}}{Re\{p_i\}Re\{p_j\} + Im\{p_i\}Im\{p_j\}} \right) \qquad (2.2)$$

The first term in (2.1) describes light emitted by individual dipoles whereas the second term depicts interference between radiated fields originating from separate distinct dipoles. If instead these sources were radiating in an incoherent manner the net intensity would exclusively be accounted for by the first term in (2.1). In that case the intrinsic phase

difference between the sources would be completely random and all intrinsic phase differences would be averaged out so that no interference effects would occur. Since the interplay and efficient coupling between different microscopic states often requires coherent interactions, this concept is vital to understand in order to get a deeper picture of the intrinsic dynamics within nanoscale systems.

From expression (2.2) it is moreover obvious that two identical dipoles ($Re\{p_i\} = Re\{p_j\}$ and $Im\{p_i\} = Im\{p_j\}$) reveal no intrinsic phase difference, which means that the net phase difference is fully dictated by the spatial phase term $\boldsymbol{k} \cdot \boldsymbol{R}_{ij}$. Therefore it is possible to tune the interference conditions between identical dipole emitters just by wisely choosing the correct intermediate distance between them.

A graphic illustration of fields from dipolar emitters, as well as a graph showing the total intensities for N emitters for both random and coherent phases, may be seen in Figure 2.1. Notice how the total intensity is either enhanced ($\phi = 2\pi$) or extinct ($\phi = \pi$) in the cases when the dipoles are emitting coherently, whereas the random-phase situation is not tunable in the same way. This is a clear sign to prove the point that coherence is required in order for modes to significantly interact and influence each other.
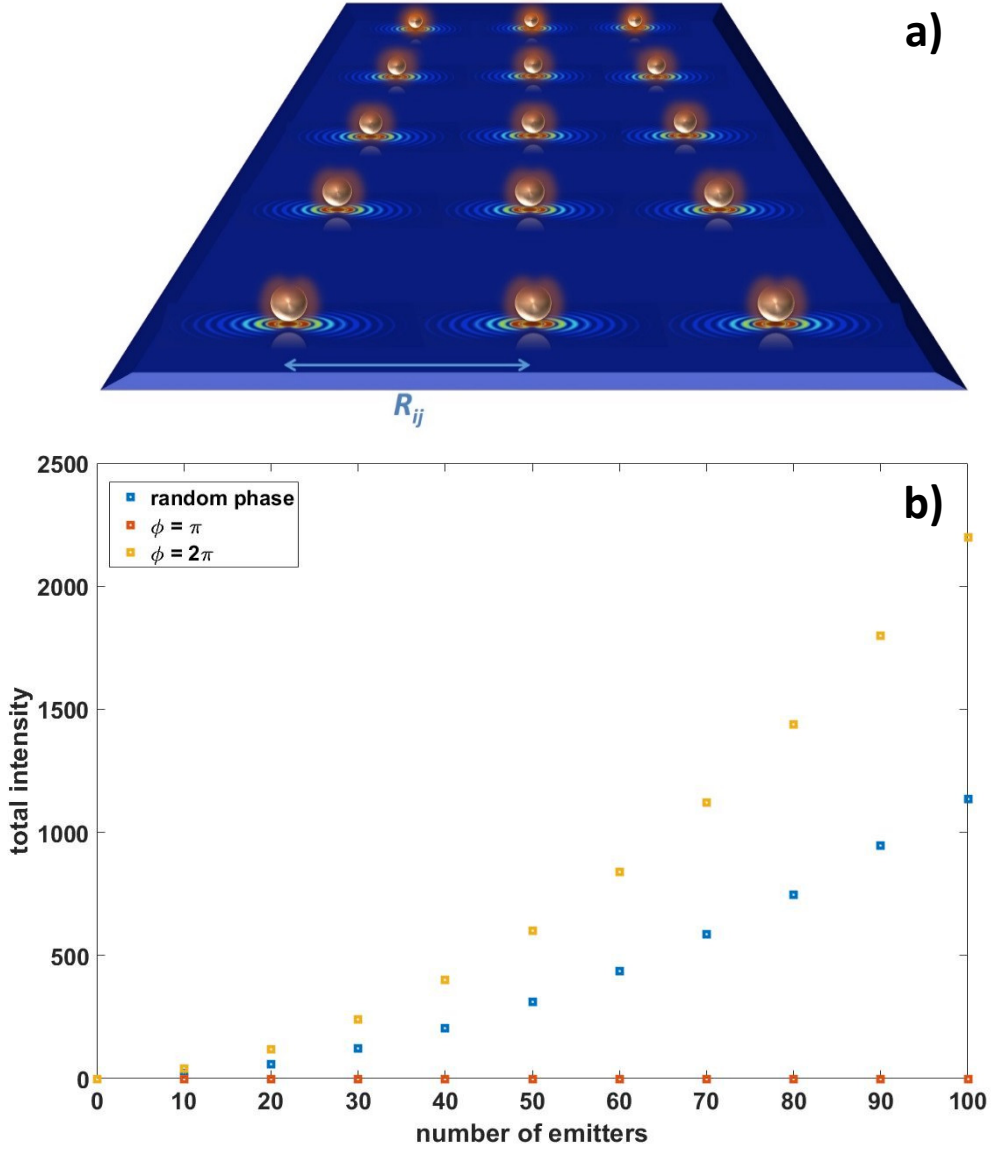
Figure 2.1. *(a) Illustration of many dipolar emitters located on a two dimensional surface. The radiation pattern from each individual dipole is projected on to the plane, which collectively forms a total radiation pattern dependent on intrinsic phase difference and intermediate spacing. (b) The total intensity from N emitters with random phase (blue), and with a coherent phase difference of either $\phi = \pi$ (red) or $\phi = 2\pi$ (yellow), according to expression (2.1).*

2.2 A quantum mechanical notion of coherence

The notion of coherence may be expanded to incorporate a wide range of physical microscopic objects besides describing properties of waves.

In the framework of quantum mechanics dynamics and properties of all microscopic particles (electrons, atoms etc.), as well as many excitations, are governed by a so-called *wave function* [35]. A wave function is a complex-valued mathematical function, which reflects the probabilistic nature of properties (such as position, linear momentum etc.) for microscopic objects in certain quantum states.

The notion of quantum coherence is exploited to signify the strength and correlation of quantum properties. So, as long as there exists a definite phase relation between different quantum states, one may define that system as possessing quantum coherence. Due to the fact that realistic quantum systems are never fully isolated, but rather interacting with their surrounding environments, the quantum coherence will eventually be lost. One may view this process as loss of "quantum information" to the environment. The process of losing quantum coherence is generally referred to as *decoherence* and relates to the collapse of the quantum mechanical wave function [36]. When components of the quantum mechanical wave function couples to the external environment it will lose its coherence by acquiring phases from the neighboring surroundings. Phenomena such as stimulated emission in lasers, Cooper-pairs in superconducting circuits and superfluid He are all examples where quantum coherence yields macroscopic effects [37].

To sum up, coherence play an important role in describing properties at the most fundamental level of nature, and in many ways guides and dictates the way reality works. In the upcoming sections, a detailed description of how coherence is vital for strong light-matter interactions will be addressed.

Chapter 3

Optical Resonances in Metal Nanoparticles, Molecules and Quantum Dots

In this chapter, the fundamental concepts of plasmon resonances in metallic nanoparticles, optical matter excitations in molecules and semiconducting nanocrystals (quantum dots), as well as in molecular aggregates are presented and described.

3.1 Optical properties of metallic nanoparticles

In nanoscale metallic entities the surface electrons are confined to spatial regions much smaller than the wavelength of electromagnetic fields with frequencies in the THz regime, i.e. including visible light.

In the presence of an oscillating incident electromagnetic field, an overall displacement of the surface electrons will transpire. This will in turn give rise to a restoring force caused by charge separation between the displaced electron cloud and positively charged lattice. These forces will result in coherent periodic oscillations of surface charge densities, which are greatly enhanced at specific frequencies. It will be shown that those specific frequencies will depend on factors such as particle geometry, as well as the surrounding dielectric environment. The phenomenon where such oscillations in surface charge densities occur, are generally referred to as *localized surface plasmon resonances (LSPR)* [8], a concept already briefly introduced in Chapter 1. What follows in this section are thorough theoretical derivations on this matter in order to understand why such phenomena takes place in metallic nanoparticles.

To begin with, the electric displacement field in a linear isotropic homogenous medium with dielectric function $\varepsilon(k, \omega)$ can be written according to

$$\boldsymbol{D}(k, \omega) = \varepsilon_0 \boldsymbol{E}(k, \omega) + \boldsymbol{P}(k, \omega) = \varepsilon_0 \varepsilon(k, \omega) \boldsymbol{E}(k, \omega) \tag{3.1}$$

The parameters ε_0, $\mathbf{E}(k, \omega)$ and $\mathbf{P}(k, \omega)$ are vacuum permittivity, electric field vector and polarizability vector respectively [9].

The equation of motion for a single conduction electron within the metal may further be denoted, according to Drude-Sommerfeld theory [38], in the time domain as

$$m\frac{\partial^2 \boldsymbol{r}(t)}{\partial t^2} + m\gamma\frac{\partial \boldsymbol{r}(t)}{\partial t} = -e\boldsymbol{E}(t) \qquad (3.2)$$

Here m, γ, e and $\boldsymbol{r}(t)$ are electron mass, damping parameter, elementary charge and spatial displacement coordinate respectively. By then applying a Fourier transform to differential equation (3.2), the resulting expression for the frequency dependent displacement coordinate becomes

$$r(\omega) = \frac{e/m}{\omega^2 + i\gamma\omega}E(\omega) \qquad (3.3)$$

In this expression i denotes the imaginary unit. Next we express the macroscopic polarizability vector, which may furthermore be interpreted as the number of dipole moments per unit volume. It is therefore suitable to write such a quantity according to the expression $\boldsymbol{P}(\omega) = -n_e e\boldsymbol{r}(\omega)$ where n_e represent the electron density in the metal. By now combining equation (3.1) and (3.3) together with the polarizability vector, the resulting form for the dielectric function of the metal may be written as

$$\varepsilon(\omega) = 1 - \frac{\omega_p^2}{\omega^2 + i\gamma\omega} \qquad (3.4)$$

$$\omega_p = \sqrt{\frac{n_e}{\varepsilon_0 m}}e \qquad (3.5)$$

Here ω_p describes the *plasma frequency* of the metal. The derivation is preceded by applying the so-called *quasi-static (Rayleigh) approximation*, which is suitable when electrons are confined to a spatial region much shorter than the wavelength of the incident field [9].

Finally, it is possible to obtain a net polarizability function valid for spheroidal shaped metallic nanoparticles according to

$$\alpha_{x,y,z}(\omega) = V\frac{\varepsilon(\omega) - \varepsilon_d}{\varepsilon_d + L_{x,y,z}[\varepsilon(\omega) - \varepsilon_d]} \qquad (3.6)$$

where $\varepsilon(\omega)$ is the function described in (3.4). The parameters V, $L_{x,y,z}$, and ε_d in expression (3.6) are the geometrical volume, geometrical form factor in the x, y or z direction which

depends exclusively on the geometrical aspect ratio, and dielectric constant of the surrounding medium respectively [9].

The expression in (3.6) does not account for factors such as radiation damping and dynamic depolarization, which are real effects to take in to account in the case of optical plasmonic resonances in metal nanoparticles [39]. In order to get more accurate theoretical estimations of the resonance position and overall spectral features, when studying light scattered from metallic nanoparticles, these factors must be paid attention to.

In order to account for these phenomena a suited tactic is to go beyond the quasi-statical Rayleigh approach and instead utilize the *modified long-wavelength approximation (MLWA)* [40]. The polarizability function in (3.6) is then altered according to the expression

$$\alpha_{MLWA}(\omega) = \frac{\alpha_{x,y,z}(\omega)}{4\pi - \frac{k^2}{r_n}\alpha_{x,y,z}(\omega) - i\frac{2}{3}k^3\alpha_{x,y,z}(\omega)} \tag{3.7}$$

The parameters $r_n \in \{r_x, r_y, r_z\}$ are lengths of each corresponding axis of the spheroid. The second term in the denominator of expression (3.7) accounts for the appearance of an enhancement maximum for particles with small finite volumes. The third term reflects radiation damping which give rise to dissipation and hence both broadens and decreases the magnitude of the spectral resonance peak for larger nanoparticle volumes.

Finally, scattering- and extinction cross-sections can be deduced and expressed from (3.7) in pursuance with the expressions

$$\sigma_{sca}(\omega) = \frac{\omega^4 n^4}{6\pi c^4}|\alpha_{MLWA}(\omega)|^2 \tag{3.8}$$

$$\sigma_{ext}(\omega) = \frac{\omega n}{c}Im\{\alpha_{MLWA}(\omega)\} \tag{3.9}$$

Parameters n and c denotes the refractive index of the surrounding medium and the vacuum speed of light respectively. The absorption cross section is consequently calculated as the result $\sigma_{abs}(\omega) = \sigma_{ext}(\omega) - \sigma_{sca}(\omega)$. These cross-sections are maximized at specific *localized surface plasmon resonance (LSPR)* frequencies

$$\omega_{\text{LSPR}} = \frac{\omega_p}{\sqrt{1 + \left(1/L_{x,y,z} - 1\right)n^2}} \tag{3.10}$$

11

At this frequency the interaction with electromagnetic fields reaches a maximum, and energy from the electromagnetic field modes may efficiently be coupled to the surface charge density oscillatory motions in the metallic nanoparticles.

Scattering- and extinction cross-sections for spheroidal nanoparticles, with 3 different aspect ratios, based on expressions (3.8) and (3.9) are plotted in Figure 3.1. Notice that the y-axis of both plots have same scale, which makes it rather straight forward to estimate how much of the extinction that can be attributed to scattering and absorption respectively.

At the LSPR frequencies, very high local field intensities are produced. If the geometry of a nanoparticle is of such a kind that it contains sharp edges, the field enhancement becomes extremely large at close vicinities to these apexes. These regions with extreme field enhancements are generally referred to as *hot spots* [41].

An illustration of the charge density distributions and hot spot regions, for several different nanoscale geometries, may be seen in Figure 3.2. Note that the polarizations of the incident field, as well as the field lines due to LSPR, are also indicated in each depicted structure.
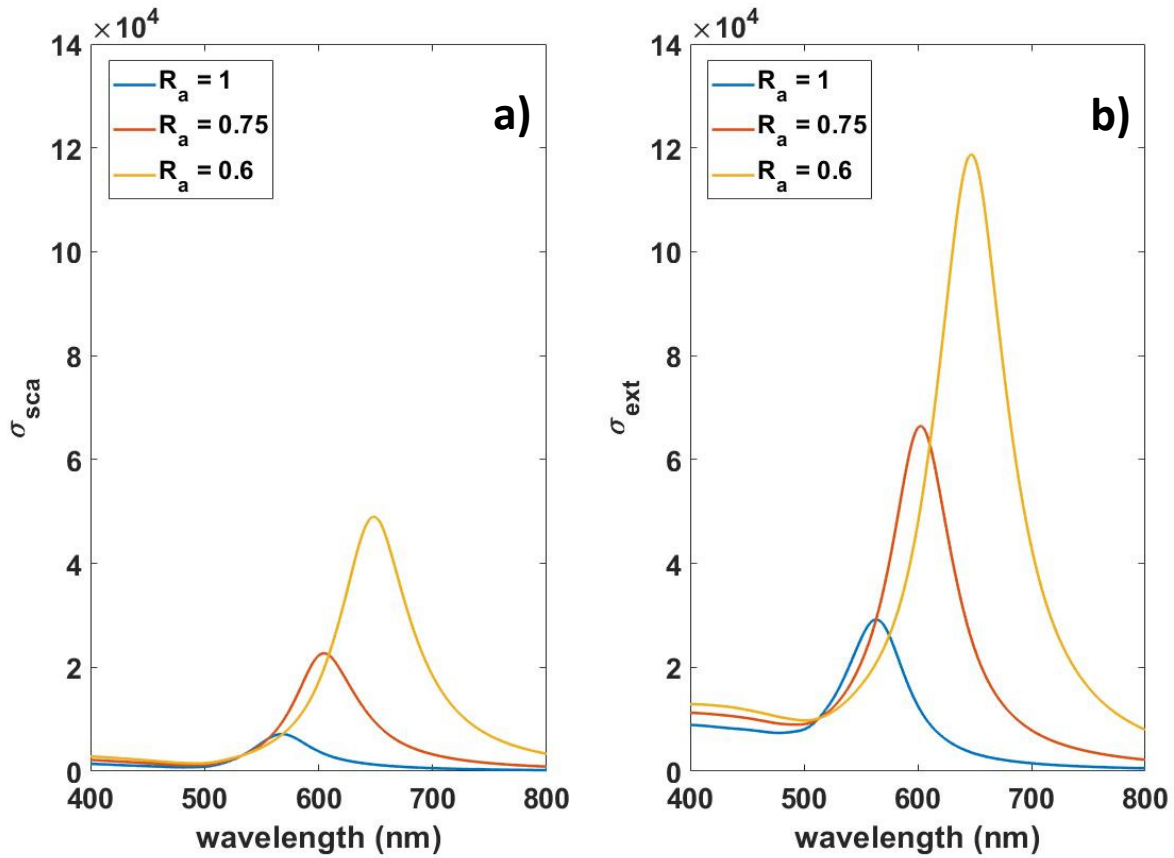

Figure 3.1. *Simulated scattering (a) and extinction (b) cross-sections based on MLWA theory, based on 3 different values of aspect ratios in spheroidal shaped nanoparticles. The units for both cross sections are given in nm².*
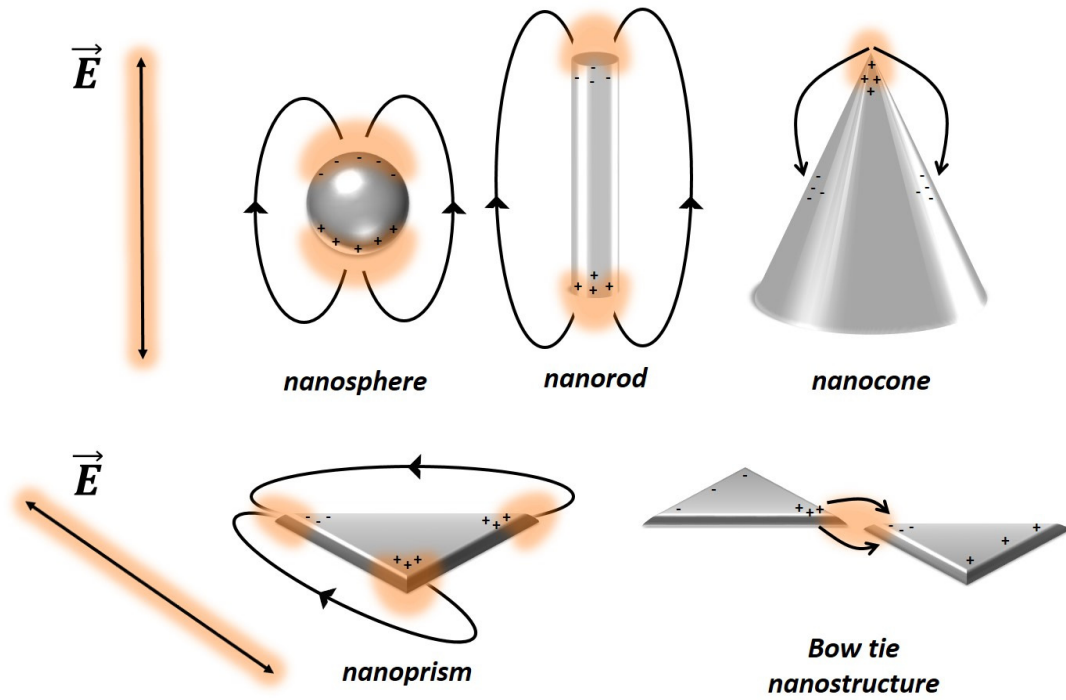
Figure 3.2. *Geometrical shapes often used as plasmonic nanoparticles. On each shape the induced charge distribution, "hot spots" and electric field lines are added for the corresponding incident polarization of an external field (indicated on the left side of the figure).*

The fact that metallic nanoparticles interacts with light predominantly at specific resonance frequencies have been utilized by humans for centuries. Unaware of the underlying fundamental mechanisms of LSPR, this phenomenon was exploited already by ancient romans where tiny particles of gold and silver where embedded in glass and admired for its remarkable light performances [42].

In Figure 3.3 (b), the famous 4th century roman Lycurgus cup is displayed, together with a graphic illustration of the displacement of the surface electron cloud associated with LSPR (Figure 3.3 (a)). Pay attention to that the Lycurgus cup is shown without/with (left/right part of Figure 3.3 (b)) a light source placed at its inner section. Note the staggering difference in colors between these two cases, which is a direct consequence of LSPR in noble metal nanoparticles. The reason for this phenomenon is that the light seen in the case displayed on the left part of Figure 3.3 (b) is reflected, whereas the light seen in the case displayed on the right part of the same figure is transmitted. The LSPR will reflect certain wavelengths and transmit other wavelengths and this is the underlying mechanism behind this distinct difference.

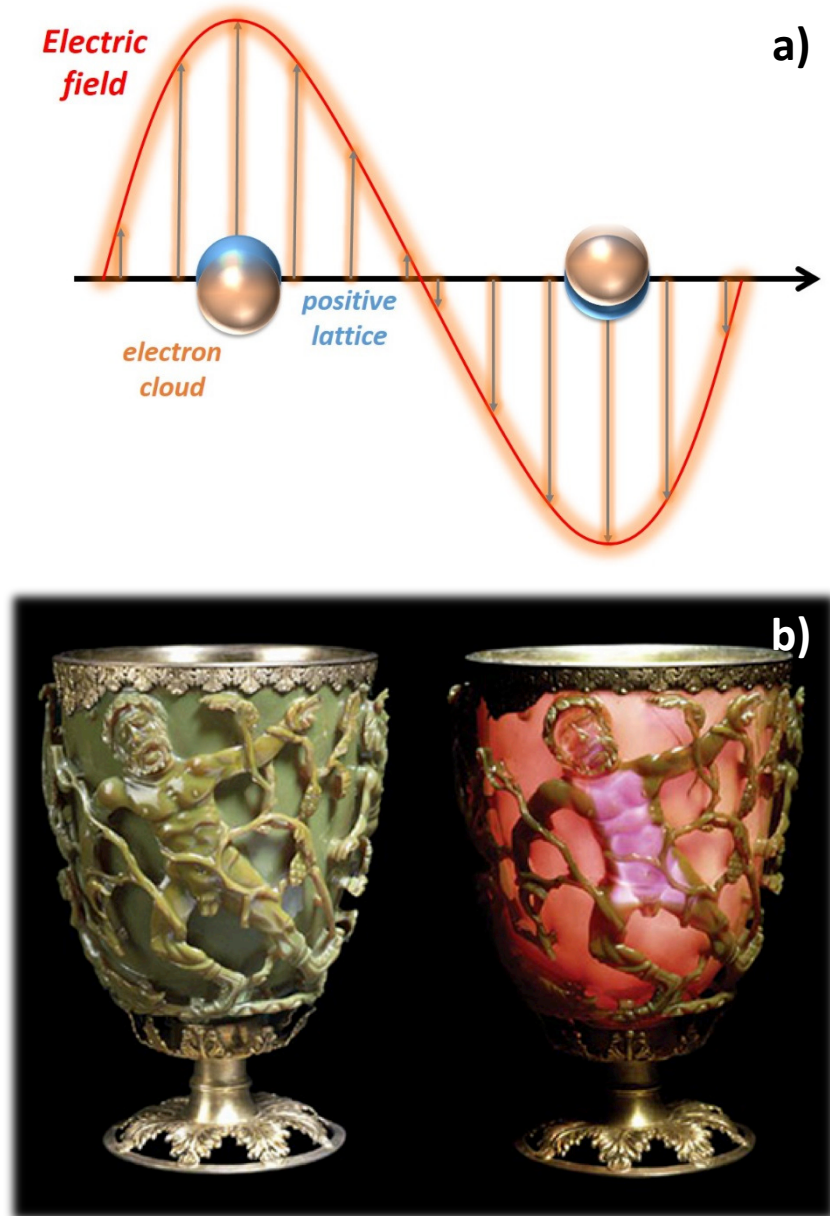**Figure 3.3**. *(a) Illustration of the LSPR phenomenon. The whole electron cloud is displaced with respect to the positively charged lattice, and will oscillate back and forth until it finally reaches its equilibrium. (b) The 4th century roman Lycurgus cup. Picture taken from [42].*

3.2 Delocalized electrons and optical resonances in molecules

Polyatomic molecules consist of microscopic structures where electrons in many cases are not spatially localized at a single atomic nucleus, but rather having the ability to move between several adjacent atomic sites. In other words, the quantum mechanical wave function describing the electron dynamics spatially extends over several adjacent atomic sites. Molecular electrons with such properties are generally referred to as being *delocalized*.

In quantum mechanics, the most frequent mathematical method to describe dynamics and additional properties of molecular electrons is to apply the concept of *molecular orbitals* [43]. In this model, the probabilistic nature of electrons is utilized and further described by a wave function, composed as a superposition of individual electron wave functions. A general expression for such a wave function can be written in the following form

$$\psi_n(r, \theta, \phi) = \sum_{l,m} R_{nl}(r) Y_{lm}(\theta, \phi) \tag{3.11}$$

Here the index n relates to the so-called orbital number. $R_{nl}(r)$ and $Y_{lm}(\theta, \phi)$ are radial hydrogen-like functions and spherical harmonics respectively. In order to further relate these orbitals to probabilistic outcomes, it is crucial that each orbital should be normalized according to

$$P_{tot} = \int_{r=0}^{\infty} \int_{\theta=0}^{\pi} \int_{\phi=0}^{2\pi} |\psi_n(r, \theta, \phi)|^2 r^2 \sin\theta \, dr d\theta d\phi = 1 \tag{3.12}$$

The knowledge of such a wave function makes it possible to extract the probability for a molecular electron to occupy a certain quantum state, with a certain energy value. A graphic sketch to illustrate the formation of molecular orbitals from atomic orbitals is shown in Figure 3.4. Note that this figure depicts both bonding and anti-bonding orbitals.

An important notification to point out here is the concept of hybridization in formation of molecular orbitals. Polariton quasiparticles, which will be emphasized strongly within this thesis, can in many aspects be thought of as hybrids between cavity and an emitter states. Hence the interaction mechanisms between the cavity and emitter in polaritons resembles in many ways chemical bonds in molecular orbitals.

The energy relaxation between an excited quantum state to a lower lying state is often possible through a release in energy via an emitted photon. The angular frequency of a photon emitted from a system with atomic energy levels E_1 and E_2 corresponds to $\omega_{12} = \frac{|E_2 - E_1|}{\hbar}$, see Figure 3.5.
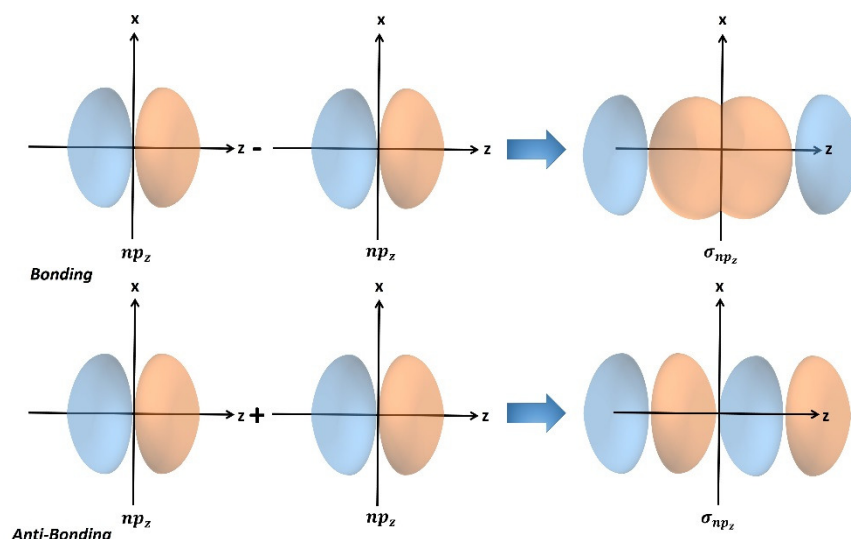
Figure 3.4. *Sketch on how molecular orbitals are formed from atomic orbitals. Note the two different cases of bonding and anti-bonding orbitals.*
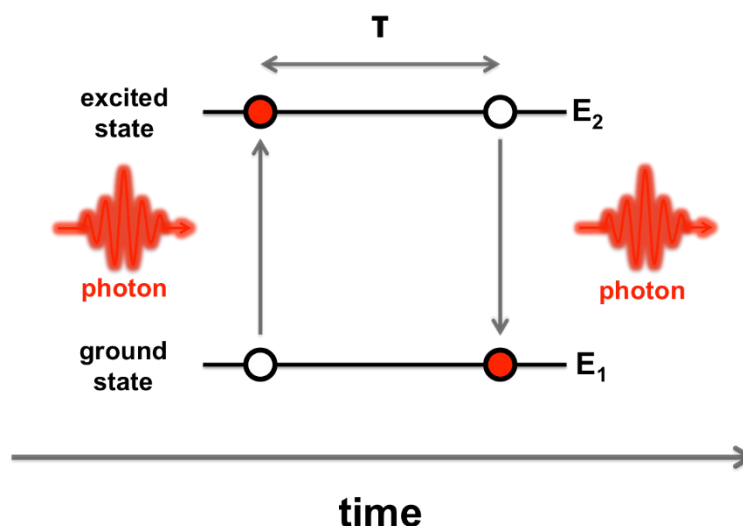
Figure 3.5. *Schematic drawing of the light-matter interaction process in molecules. The molecular electrons absorb a photon and the system enters an excited quantum state for a time period τ, before it relaxes to its energetic ground state through the emission of a photon. This photon energy corresponds to the energy difference between the excited and ground quantum states.*

This result is obtained rather easily by solving the time-dependent Schrödinger equation, which relies on unitary operations and doesn't take any energy dissipation or interactions with the surrounding environment into account. In reality atomic energy levels experiences a finite lifetime τ due to factors such as perturbation from the surrounding environment. Hence, each state-relaxation is assigned to a spectral distribution with a linewidth symmetrically distributed around the resonance frequency [43].

The intensity distribution of an excited molecular quantum state will hence be proportional to a *Lorentzian function* of the form

$$I(\omega) \sim |f(\omega)|^2 \sim \frac{\gamma^2/4}{(\omega - \omega_0)^2 + \gamma^2/4} \tag{3.13}$$

Here, the dissipation parameter $\gamma = \gamma_{rad} + \gamma_{nr}$ depends on both radiative and non-radiative processes which accounts for energy dissipation in the system. From (3.13) it is self-evident that a maximum occur at the spectral position ω_0 which is the optical *resonance frequency*.

Moreover, at frequencies $\omega = \omega_0 \pm \frac{\gamma}{2}$ the spectral function reaches its half-maximum value, which indicates that the width of the spectral line, dictated by (3.13), has a value of γ and can be defined as a *full-width half maximum (FWHM)*.

The expression for the population probability of the excited state in the time-domain may then be written according to

$$P(t) \sim |f(t)|^2 \sim \left| e^{-\frac{\gamma}{2}t} e^{i\omega_0 t} \right|^2 = e^{-\gamma t} \tag{3.14}$$

The lifetime of the excited quantum state is hence related to the damping parameter according to $\tau = \gamma^{-1}$ since the population probability $P(t)$, described by (3.14), becomes negligible for times $t > \tau$.

The probability for an excited quantum state as a function of both frequency and time, with different damping parameters, are displayed in Figure 3.6.

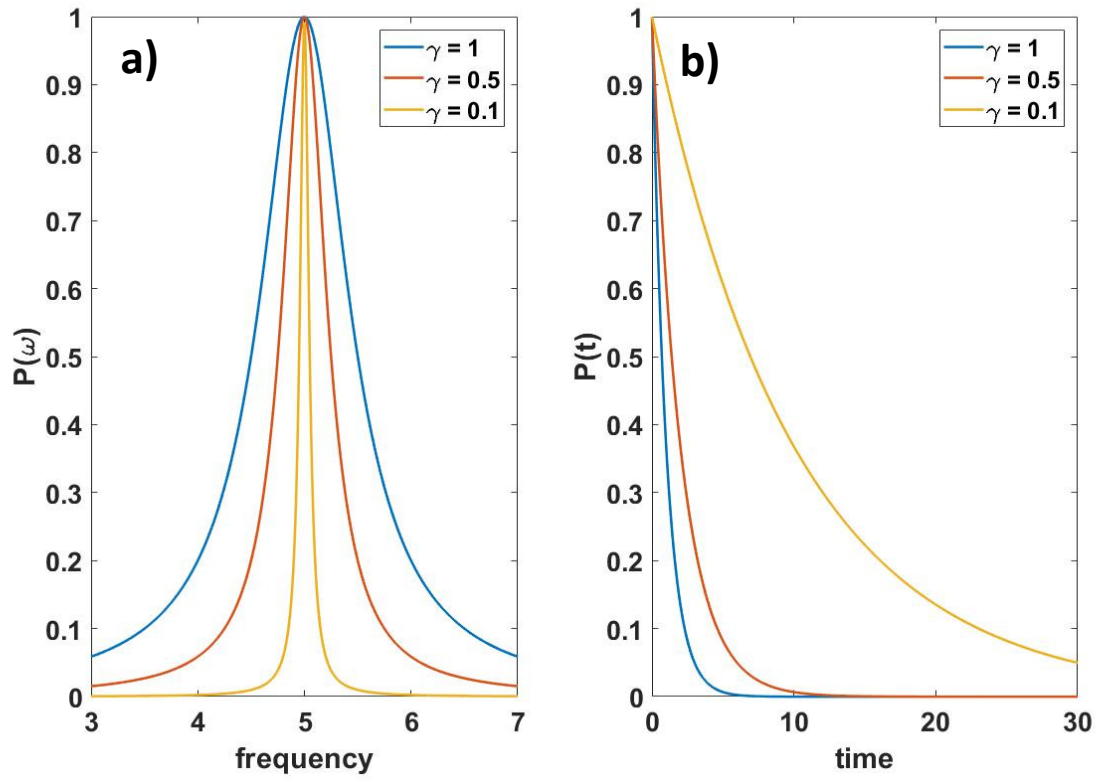**Figure 3.6.** *(a) Lorentzian function in frequency space with three different damping parameters. (b) Probability as a function of time for the same damping parameters as in figure (a). All parameters may be considered to possess arbitrary units.*

3.3 Quantum confinement and excitons in semiconducting nanocrystals

In this section the notion of quasiparticles, as well as the concept of both neutral and charged excitons, will be presented and discussed in order to give the reader some basic understanding on how to view excitations within solid-state systems. Moreover, a section devoted to illustrate the notion of delocalized excitations in molecular aggregates will be presented.

3.3.1 Treating excitations in solid-state physics as quasiparticles

Consider a microscopic system containing plenty of particles, which interacts with each other in a complex and intricate manner. In order to simplify this many-body problem one may take advantage of the fact that particles within these systems behave as if they were weakly interacting particles in free space [38].

For instance, when studying the dynamics of an electron within a semiconducting crystal, its complicated interaction with other electrons and the lattice potential can approximately be described as a free electron with a different mass, a so-called *effective mass* [44]. This "new" electron may then be considered as a *quasiparticle*. The same approach can be applied for various systems, to create quasi-particles such as *phonons* (quantization of collective lattice oscillations), as well as *surface plasmons* (quantization of surface charge density oscillations in noble metal nanoparticles). Plasmon-exciton hybrid excitations, also known as *polaritons*, also fit well to the notion of quasiparticles [45].

3.3.2 The concept of excitons

As previously described, it is suitable to treat an electronic excitation in a semiconducting crystal as a quasiparticle. An unavoidable consequence of exciting an electron from the valence band to the conduction band in a semiconductor system is the creation of a hole in the valence band [46]. The resulting two-body system is generally referred to as an *exciton*. In other words, an exciton is comprised of an electron-hole pair, bound together via attractive Coulomb interaction [8]. Hence, an exciton has to be regarded as a neutrally charged quasiparticle. The total Hamiltonian for the exciton may thus be written as

$$\hat{H}_{exciton} = \underbrace{-\frac{\hbar^2}{2m_h}\nabla_h^2}_{\substack{hole \\ kinetic \\ energy}} \underbrace{-\frac{\hbar^2}{2m_e}\nabla_e^2}_{\substack{electron \\ kinetic \\ energy}} \underbrace{-\frac{e^2}{4\pi\varepsilon_0\varepsilon_s|R_h - R_e|}}_{\substack{electron-hole \\ Coloumb \\ interaction}} \tag{3.15}$$

Here m_h and m_e describes the effective band masses of the hole and electron within the exciton, and ε_s the dielectric constant of the semiconductor material respectively. A graphic sketch illustrating the bound electron-hole pair in an exciton can be seen in Figure 3.7.

The term representing the electron-hole Coulomb interaction in (3.15) doesn't need to be taken into account when studying small semiconducting quantum dots, since the exciton is spatially confined to a very restricted region. Hence, both hole and electron may be treated theoretically as a particle-in-a-box scenario [8]. By solving the time-independent Schrödinger equation, the energy values for the system appears as discretized levels according to the expression

$$E_{e,h} = \frac{\hbar^2 \pi^2}{2m_{e,h}} \left[\left(\frac{n_x}{L_x}\right)^2 + \left(\frac{n_y}{L_y}\right)^2 + \left(\frac{n_z}{L_z}\right)^2 \right] \tag{3.16}$$

The box volume is described by $V = L_x L_y L_z$ and the different energy levels, described by (3.16), are determined by the parameters $\{n_x, n_y, n_z\} \in \mathbb{N}$. Hence, smaller side lengths of the box result in higher the energies [35]. This phenomenon is a consequence of Heisenberg's uncertainty principle, which states that the uncertainty in linear momentum of a quantum object increases (hence also uncertainty in kinetic energy) when restricted to a more well defined spatial region [8].
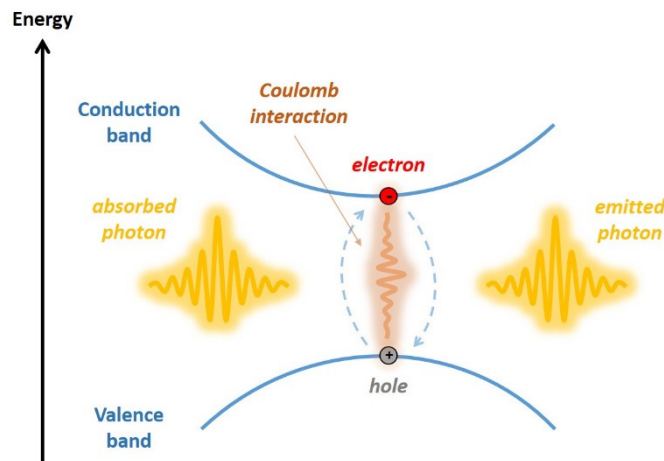

Figure 3.7. *Graphic sketch of electron-hole pair formation, held together via Coulomb interaction, in an exciton.*

By exploiting the *effective mass approximation* model [44], one may furthermore derive the shift of band-gap energy ΔE_{bg} due to exciton confinement according to the expression

$$\Delta E_{bg} = \frac{\hbar^2 \pi^2}{2\mu R^2} - \frac{1.8 e^2}{\varepsilon R}$$

(3.17)

where μ is the reduced mass of the electron-hole pair and R the radius of the spherical quantum dot. An additional factor to mention is that the non-radiative decay increases with size of the quantum dot [47]. Due to this fact, small quantum dots have rather high quantum efficiencies for radiative decay and are hence considered to be very suitable for optoelectronic applications at the nanoscale [8].

The interior building blocks of a typical CdSe/ZnS quantum dot, together with liquid solutions containing such quantum dots of various sizes, may be seen in Figure 3.8. The bottles containing the solutions are arranged from left to right in an ascending average size of spherical quantum dots. Notice further how the emission energies, in accordance with (3.16) and (3.17), decrease (violet to red) when the average geometrical size (particle-in-a-box volume) of the quantum dots increases.

3.3.3 Frenkel and Wannier-Mott excitons

The exciton is, as previously described in this section, a neutral charged bound electron-hole pair with the ability to transport energy without transporting a net charge [46]. The notion of an exciton is often further categorized into different types depending on certain inherent properties, dictated by conditions within the semiconducting material.

If a material possesses a high or low value on the dielectric constant, the Coulomb interaction between the electron and hole varies significantly, see (3.15). For instance, a high Coulomb interaction leads to a more confined and smaller exciton. Such excitons are often found in organic molecular crystals composed of aromatic molecules and are generally referred to as *Frenkel excitons* [38]. Frenkel excitons are localized at single molecular sites. These excitons are moreover often stable in room temperature environments.

However, in semiconducting crystals (such as GaAs) the dielectric constant is usually a large quantity, which according to (3.15) generates small Coulomb interactions. The corresponding exciton radii in these cases exceed the lattice spacing parameter. Quasiparticles of this type are referred to as propagating *Wannier-Mott* excitons, and are often found within semiconducting crystals with small energy gaps [38]. These types of excitons, in contrast to

Frenkel excitons, are often unstable at room temperature environments due to their relatively low binding energies, and thus require cryogenic conditions.

3.3.4 Trion excitations and possible exploitations

Similar to the previously described exciton, there are other forms of localized matter excitations in solid-state semiconductor systems. A specific type of quasiparticle (commonly appearing in quantum dots, 2D materials etc.) is the *trion*.

A trion is a three-particle system, which consists of either two electrons and one hole (negative), or 1 electron plus 2 holes (positive) [48]. Thus, the trion may be regarded as a charged exciton. Hence, in contrast to an exciton the trion is a charged quasiparticle, which might be exploited for intricate charged polariton manipulations when a trion is strongly coupled to a plasmonic nano-cavity (see Paper V). This would imply a future possibility to manipulate light with electricity and vice versa.

In many 2D materials the trion quasiparticle is rather unstable at room temperatures due to low binding energies. This implies that a decrease in temperature to cryogenic environments is often required for the trion to emerge. This furthermore entails that plasmon-trion polaritons are tunable with respect to temperature, which is yet another profitable property to exploit and widens the versatility aspect of such nanoscale systems.

Some further characteristics of plasmon-exciton-trion polariton branches, when a resonant cavity couples to both excitons and trions, will be theoretically derived and discussed in section 4.3.8.
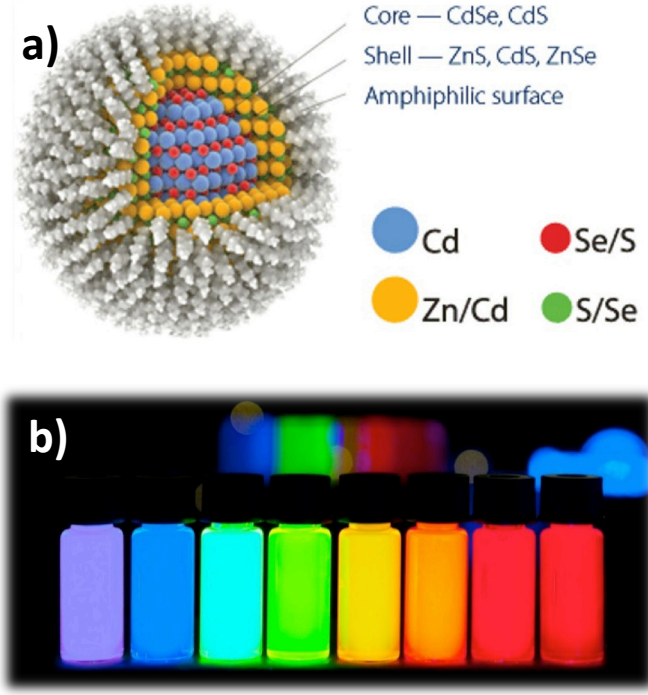
Figure 3.8. *(a) A graphic sketch of different segments in the interior of a CdSe/ZnS quantum dot. Picture taken from [49].* ***(b)*** *Liquid solutions containing CdSe/ZnS quantum dots of various sizes. In the image the average size of quantum dots in the solutions are increasing from left to right. Picture taken from [50].*

3.3.5 Temperature effects on excitons

Since excitons exist in semiconductor materials they will interact with the surrounding local environment. This indicates that exciton dynamics will be affected by the conditions of the neighboring surroundings [51]. For instance, the total dissipation of excitons depend on the temperature of the local environment in a manner described by the following expression

$$\gamma(T) = \gamma(0) + \alpha T + \beta N(T) \tag{3.18}$$

The first term, which indicates the dissipation at $T = 0$ has still a non-zero value due to scattering from imperfections and further impurities within the semiconductor material. The second term in expression (3.18) refers to the linear temperature dependence, which arises as a result of that the exciton interacts with acoustic phonons. The parameter α quantifies the strength of this interaction. The third term describes interactions between the exciton and longitudinal optical phonons where β regulates the strength of the interaction and $N(T)$ is the average occupation number, given by Bose-Einstein statistics according to the expression

$$N(T) = \frac{1}{exp\left(\frac{\hbar\omega_{ph}}{k_b T}\right) - 1}$$

(3.19)

Here, $\hbar\omega_{ph}$ and $k_b T$ describes the phonon- and thermal energies of the surrounding environment respectively.

It turns out that the temperature dependence of exciton dissipation might be utilized to play an important role in affecting the photo-response in plasmon-exciton hybrid systems, see Paper II, Paper III and Paper V.

3.3.6 Delocalized excitations in molecular J-aggregates

Besides the previously mentioned optical resonances in molecules and semiconducting nanocrystals, there is yet another type of optical excitation that might occur in systems when certain molecular structures aggregate to form ordered clusters [52].

When molecules assemble themselves in aggregated structures their optical properties changes dramatically [53]. For example TDBC dye monomers, which molecular structure can be seen in Figure 3.9 (a), experience a substantial spectral shift upon interaction with adjacent molecules. It may arrange itself in a head-to-head or a head-to-tail configuration, which leads to different energy states (see Figure 3.9 (b)). In the head-to-tail configuration the optical resonances of the adjacent monomers are in-phase which results in electrostatic attraction [54]. As a result the energy level of such a configuration is hence lowered, which implies a spectral red shift. With the same reasoning, the head-to-head configuration causes a blue shift due to electrostatic repulsion from out-of-phase optical resonances in contiguous monomers.

In addition to the spectral red shift in the head-to-tail configuration, the spectral peak furthermore experience narrowing upon aggregation. The reason for this is that the optical excitations (excitons) in coupled head-to-tail TDBC monomers are delocalized over as many as 15 adjacent monomers at room temperature [53], rather than being localized on a single molecule as in the case with isolated monomers. Besides spectral narrowing, this also results in larger transition dipole moments. In fact, the narrowing of linewidths in J-aggregates with respect to monomers can be related as

$$\gamma_J \propto \frac{\gamma_m}{\sqrt{N}}$$

(3.20)

where *N* denotes the number of molecules over which the molecular exciton is delocalized. The delocalization number in J-aggregates does increase further upon cooling to cryogenic temperatures.

The extinction spectrum of both TDBC monomers and J-aggregated dissolved in an aqueous solution can be seen in Figure 3.9 (c). Notice the difference in both spectral position and morphology between extinction in monomers and J-aggregates.

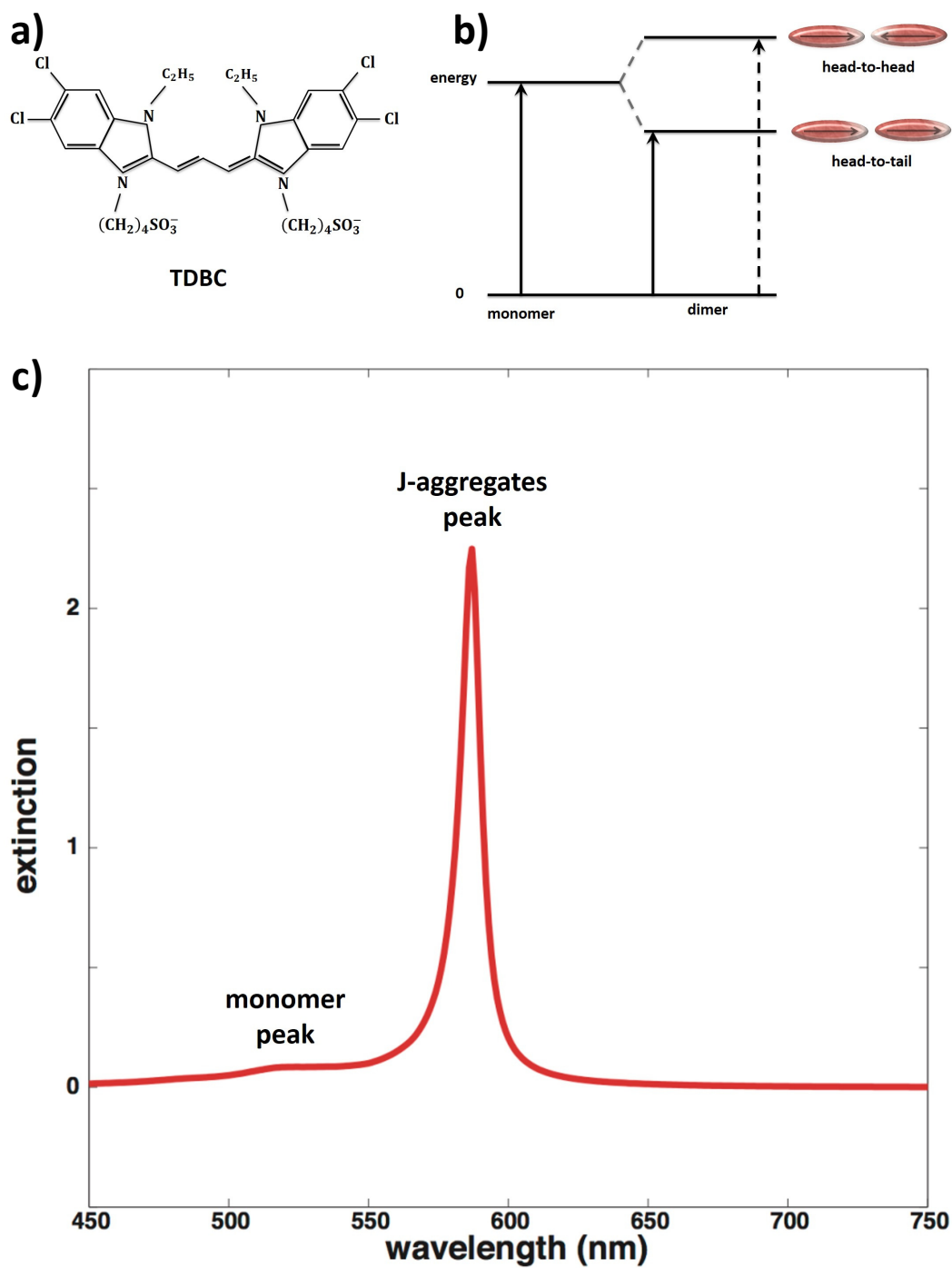**Figure 3.9.** *(a) Molecular structure of the TDBC monomer. (b) Energy structure of both monomers and J-aggregates in a head-to-tail and head-to-head configuration. (c) Optical extinction spectrum of TDBC monomers and J-aggregates in a solution.*

Chapter 4

Interactions between a Resonant Optical Cavity and Emitters

A model widely utilized to simulate light-matter interactions is a two-level system positioned inside a resonant optical cavity [55]. This scheme predicts several experimental outcomes in modern quantum optics and nano-photonics and is accordingly widely regarded as a cornerstone for understanding strong light-matter interactions. Hence, it is one of the most reliable theoretical tools to forecast intriguing photo-dynamics and reveal intricate dynamics within nanoscale hybrid systems.

In this chapter a set of different theoretical frameworks on this matter will be presented. Initially, concepts such as weak- and strong cavity-emitter interactions are defined and presented. Thereafter, several different theoretical frameworks, which are based both on classical and quantum dynamics are displayed and discussed to give the reader a wide overview of how to treat and model photo-dynamics within hybrid systems. Finally, a separate theoretical framework on how to describe and apprehend inelastic energy relaxations within hybrid systems will be presented.

4.1 Weak cavity-emitter interactions

When the interaction between an optical cavity mode and an emitter excitation is weak the resulting dynamics may adequately be described utilizing Fermi's golden rule [56]. With this in hand an expression for the transition rate of the excited emitter, weakly coupled to a cavity mode, can be derived according to

$$\Gamma_{cav} = \frac{2\pi}{\hbar} |\langle \mu_{12} E \rangle|^2 D_{cav}(\omega)$$

(4.1)

Here, μ_{12} and E are the transition dipole moment of the emitter and electric field related to the cavity mode respectively. The function $D_{cav}(\omega)$ describes the density of states of the cavity and may explicitly be written as

$$D_{cav}(\omega) = \frac{1}{\pi V} \frac{(\gamma/2)}{(\omega - \omega_{cav})^2 + (\gamma/2)^2}$$

(4.2)

The parameters γ, ω_{cav} and V are cavity dissipation rate, resonance frequency and mode volume respectively.

To simplify further, consider a situation with a perfect matching of orientations between the cavity field and the emitter dipole as well as their frequencies being on exact resonance. Then the transition rate of an emitter coupled to a cavity mode, with respect to free space, may be written as

$$\Gamma_{cav} = F_p \Gamma_{free} \tag{4.3}$$

The relating parameter F_p in (4.3) is known as the *Purcell factor,* and can explicitly be expressed as

$$F_p = \frac{3}{4\pi^2} \left(\frac{\lambda_{cav}}{n} \right)^3 \frac{Q}{V} \tag{4.4}$$

Here Q, λ_{cav} and n are cavity quality factor, cavity field wavelength and refractive index respectively [57].

From expressions (4.3) and (4.4) it is evident that the presence of the optical cavity results in an enhancement of spontaneous emission of the emitter (as long as $F_p > 1$). The lifetime of an emitter excitation may consequently be modified considerably upon interaction with the cavity modes, since it scales inversely proportional to the transition rate.

4.2 Strong cavity-emitter interactions

In contrast to the weak-coupling regime, a situation may appear where the energy transfer rate between the cavity and emitter is more rapid than any other dissipation or decoherence processes. These interactions cannot be treated as simple perturbations, described by Fermi's golden rule as in section 4.1.

In this regime the energy will be oscillating back and forth between the cavity and emitter modes several times before it finally decays to the surrounding environment [24]. This phenomenon is called Rabi oscillations and will be covered more in detail within the upcoming sections. It is only when a system resides in this so-called *strong coupling regime* that several new intricate properties arise, and polariton physics comes in to play. In this regime plenty of previous material properties will behave in completely different ways.

In the following subsections, different theoretical frameworks on how to describe and model cavity-emitter interactions will be derived and presented.

4.3 Theoretical frameworks for describing cavity-emitter interaction dynamics

In order to describe photo-dynamics of a system composed of a plasmon coupled to an exciton, several different theoretical models may be used. Certain dynamics can be accounted for by applying purely classical physics, whereas other phenomena require quantum mechanical theoretical frameworks [55]. In this section, several different theoretical models are presented and elaborated on to give the reader a wider view on how to perceive and apprehend strong coupling dynamics.

4.3.1 The classical coupled oscillator model

In order to simulate a resonant cavity coupled to an arbitrary number of N independent emitters we utilize a classical coupled-oscillator model [26]. In this model the equilibrium-displacements coordinates are denoted x_c and x_k for the cavity and the k:th emitter $(1 \leq k \leq N)$ respectively. Moreover we may assume that the absorption from the incident field on each emitter is negligible, compared with the near field of the cavity. The force denoted with F_c in Figure 4.1 drives the cavity-oscillator (blue rod), but do not directly displace the emitter-oscillators (golden spheres).

The dynamics of a resonant oscillator coupled to N independent oscillators (see Figure 4.1), all exclusively driven by the cavity oscillator, may be described by the following set of differential equations

$$\frac{\partial^2 x_c}{\partial t^2} + \gamma_c \frac{\partial x_c}{\partial t} + \omega_c^2 x_c + \sum_{k=1}^{N} g_{0k} \frac{\partial x_k}{\partial t} = F_c$$

$$\frac{\partial^2 x_1}{\partial t^2} + \gamma_{01} \frac{\partial x_1}{\partial t} + \omega_{01}^2 x_1 - g_{01} \frac{\partial x_c}{\partial t} = 0 \qquad (4.5)$$

$$\vdots$$

$$\frac{\partial^2 x_N}{\partial t^2} + \gamma_{0N} \frac{\partial x_N}{\partial t} + \omega_{0N}^2 x_N - g_{0N} \frac{\partial x_c}{\partial t} = 0$$
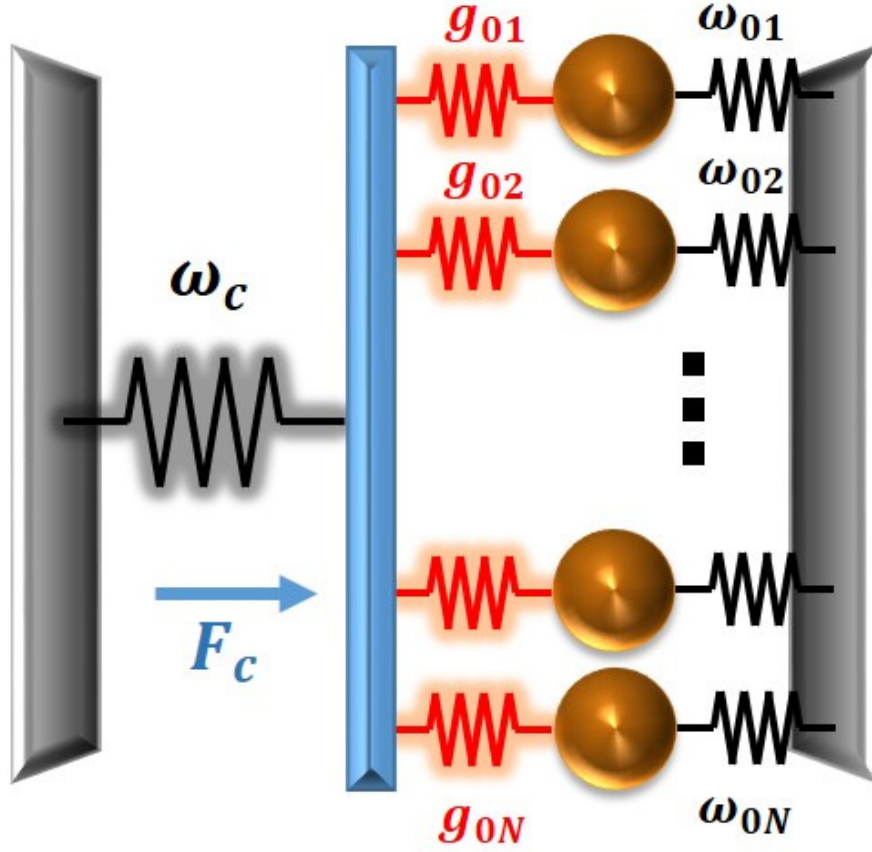
Figure 4.1. *A graphic illustration of the classical coupled oscillator model.*

Here γ_c, γ_{0k}, ω_c, ω_{0k} are dissipation rates/resonance frequencies for the cavity and the k:th emitter respectively. The parameters g_{0k} describes the coupling parameter between the cavity and the k:th emitter. The solutions for the equilibrium-deviation coordinates x_c and x_k in (4.5), may then be described in frequency space by the expressions

$$x_c \sim \frac{\prod_{j=1}^{N}(\omega^2 - \omega_{0j}^2 + i\gamma_{0j}\omega)}{(\omega^2 - \omega_c^2 + i\gamma_c\omega)\prod_{j=1}^{N}(\omega^2 - \omega_{0j}^2 + i\gamma_{0j}\omega) - \omega^2 \sum_{j=1}^{N} g_{0j}^2 \prod_{k=1}^{N}(\omega^2 - \omega_{0k}^2 + i\gamma_{0k}\omega)^{(1-\delta_{jk})}}$$

$$x_k \sim \frac{i\omega g_{0k}}{(\omega^2 - \omega_{0k}^2 + i\gamma_{0k}\omega)} x_c \tag{4.6}$$

$$\delta_{jk} = \begin{cases} 1, & j = k \\ 0, & j \neq k \end{cases}$$

The scattering cross section for the system may then be related, via equation (3.8), to the coupled classical cavity equilibrium-displacement coordinate in (4.6) as

$$\sigma_{sca}(\omega) \sim \omega^4 |x_c|^2 \tag{4.7}$$

The scattering cross section in (4.7), together with absolute value of equilibrium-displacement coordinate for a random coupled emitter, are plotted in Figure 4.2 (a) as well as absolute values (Figure 4.2 b) and phases (Figure 4.2 c) of equilibrium-deviation coordinates for all coupled emitters. This simulation is done according to expressions (4.6) and (4.7) where $N = 100$ oscillators, with a coupling strength dictated by $g_{0i} = g_0 \cos \theta_i$. The parameter θ_i is a uniformly distributed random number in the range $\left[0, \frac{\pi}{2}\right]$. The reason for this is to mimic the fact that alignment of the optical cavity field vector, with respect to molecular transition dipole moments of emitters, generally varies randomly within plasmon-exciton systems.

It is clear that the phases of each emitter in Figure 4.2 (c) coincide rather well around the resonance wavelength, which by the criteria described in Chapter 2, does imply coherence. This is a result of the fact that the cavity-oscillator, rather than the external field, drives all emitters and thus all emitters are governed by the phase of the cavity-oscillator.

Another important observation to make is that even if the coupling strength between the cavity-oscillator and a single emitter is rather small, the absolute value for the equilibrium-deviation coordinate for each emitter changes dramatically upon coupling to the cavity oscillator. Rather than displaying narrow resonances at values close to 588 nm, all spectra from emitters in Figure 4.2 (b) exhibit signs of hybridization. The reason for this is that the coherent motion of all emitters result in a collective coupling strength according to $g_{TOT} = g_0 \sqrt{\sum_{i=1}^{N} \cos^2 \theta_i}$, which can be thought of as the net coupling strength that all emitters finally experiences. Note further that the vacuum Rabi splitting parameter, which is used to determine the strength of light-matter interactions from experimental data, would then be expressed as $\Omega = 2g_{TOT}$.

How dynamics of strongly and weakly coupled systems differs in the time domain is furthermore displayed in Figure 4.3. The figure plots the cavity equilibrium-displacement coordinate over time in the cases where the cavity oscillator is coupled to either $N = 2$ (Figure 4.3 a) or $N = 80$ (Figure 4.3 b) emitters. Note how the energy oscillates back and forth several times in the case when $N = 80$, whereas this behavior is absent in the weakly coupled case ($N = 2$). Since the coupling strength of each individual oscillator is kept constant at a value of $g_0 = 80 \, meV$, this is a result of an increase in the collective coupling rate when the amount of emitters are changed from $N = 2$ to $N = 80$.
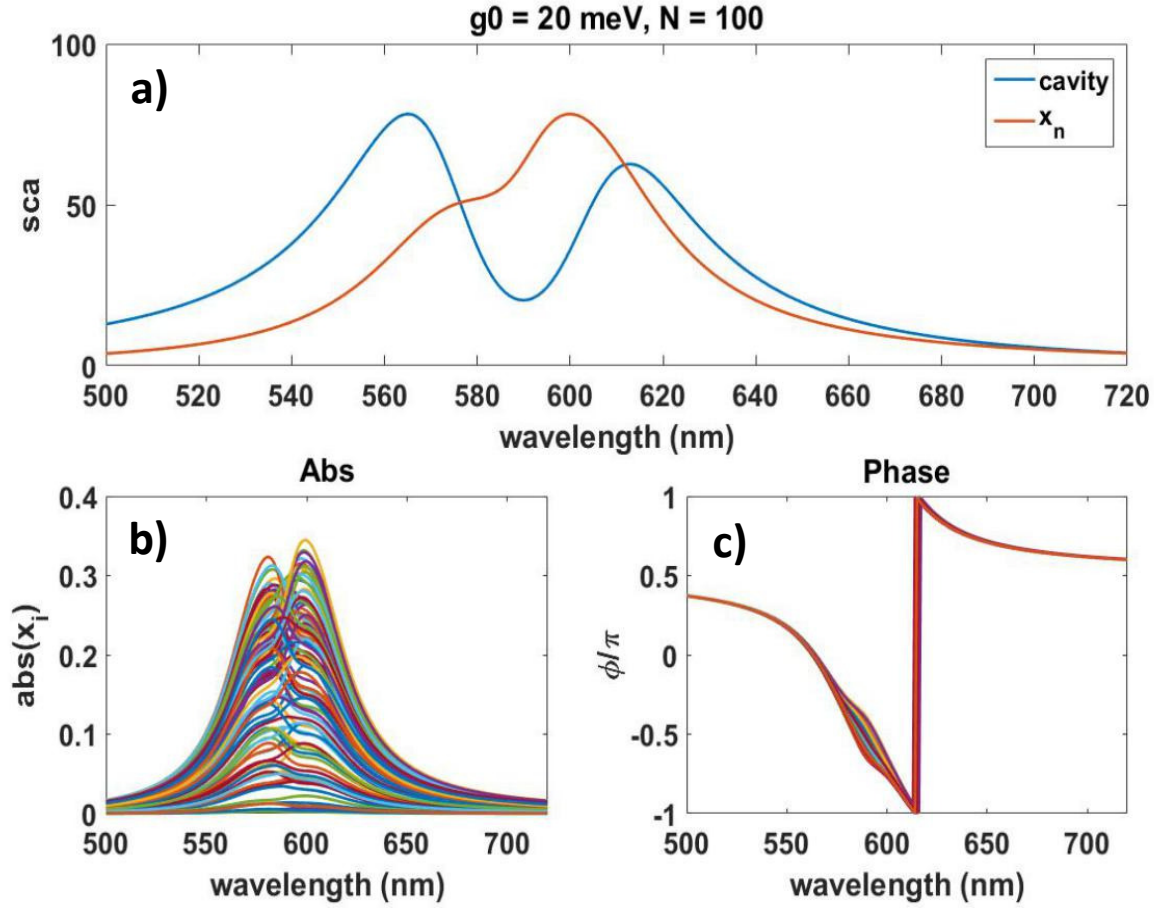
Figure 4.2 *Simulated values from the classical coupled oscillator model. (**a**) Scattering values from both cavity and a random emitter. (**b**) Absolute value of equilibrium-displacement coordinates spectra of each emitter coupled to the cavity. (**c**) Phases at different wavelengths for each emitter coupled to the cavity.*

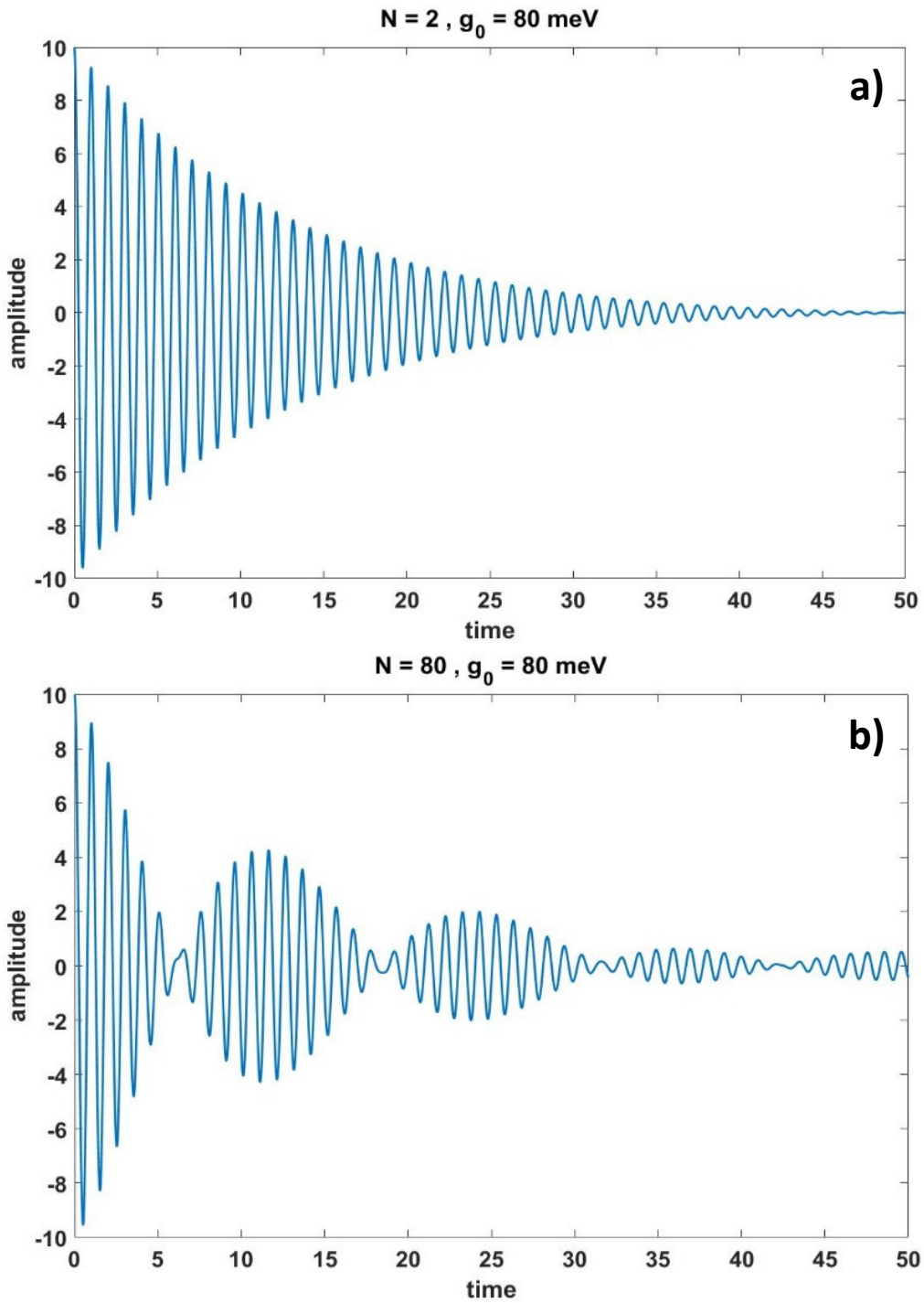**Figure 4.3** *Simulated values from the classical coupled oscillator model as a function of time. The graphs display the oscillation of the cavity oscillator equilibrium-deviation coordinate for cases where the cavity is coupled to either N=2 (**a**) or N=80 (**b**) emitter oscillators, with $g_{0k} = 80\,meV$.*

4.3.2 Coherent and incoherent polariton states

In contrast to the previously described purely classical coupled oscillator model, we may now study a system composed of a resonant cavity coupled to N distinct non-interacting emitters, all with quantized energies. Such a system may be theoretically modeled in the following way:

Initially we omit any dissipation within the system and consider only a single cavity excitation coupled to N independent emitters. By denoting resonance frequencies of the cavity and the ith emitter $(1 \leq i \leq N)$ as ω_p and ω_{0i} respectively, together with cavity-emitter coupling terms as g_i, the explicit form of the system Hamiltonian [58] may be expressed according to

$$\widehat{H} = \hbar\omega_p|p\rangle\langle p| + \hbar \sum_{i=1}^{N} \omega_{0i}|e_i\rangle\langle e_i| + \hbar \sum_{i=1}^{N} (g_i|e_i\rangle\langle p| + g_i^*|p\rangle\langle e_i|)$$

(4.8)

$$|p\rangle = |1, 0, \dots\dots, 0\rangle$$
$$|e_i\rangle = |0, \dots, \underset{i:th}{1}, \dots\rangle$$

Note that 1 and 0 inside the ket-notations in (4.8) indicates that a specific subsystem (with index between 1 and N) is either excited or in its ground state.

By applying the time-independent Schrödinger equation, with the Hamiltonian described in (4.8), the frequency eigenvalues of the system may be found as solutions to the following equation

$$(\omega_p - \omega) \prod_{i=1}^{N} (\omega_{0i} - \omega) - \sum_{i=1}^{N} |g_i|^2 \prod_{j=1}^{N} (\omega_{0j} - \omega)^{(1-\delta_{ij})} = 0$$

(4.9)

Here the parameter δ_{ij} denotes the Kronecker-delta

$$\delta_{ij} = \begin{cases} 1, & i = j \\ 0, & i \neq j \end{cases}$$

(4.10)

By further assuming that all N emitter resonance frequencies are approximately the same $(\omega_{0k} \approx \omega_0, \forall\, k, 1 \leq k \leq N)$, the eigenvalues of the system can be expressed as

$$\left[\omega_{D1}, \omega_{D2}, \omega_{D3}, \dots\dots, \omega_{D(N-1)}\right] = \omega_0$$

(4.11)

and

$$\omega_{B1} = \frac{(\omega_0 + \omega_p)}{2} + \sqrt{\sum_{i=1}^{N} |g_i|^2 + \frac{\delta^2}{4}}$$

$$\omega_{B2} = \frac{(\omega_0 + \omega_p)}{2} - \sqrt{\sum_{i=1}^{N} |g_i|^2 + \frac{\delta^2}{4}}$$

Here the parameter $\delta = \omega_p - \omega_0$ describes the detuning between the cavity and emitter resonances. From the expressions in (4.11) one may conclude that a hybrid system comprised by a cavity coupled to N distinct non-interacting emitters will result in a total of $N+1$ states. Out of the total $N+1$ states, 2 resonate at frequencies ω_{B1} and ω_{B2} (*bright polariton states*) and $N-1$ resonating at ω_0. The latter are labeled as *dark states* since the photonic component in each of these states is very small compared to the bright states. The notion of dark states didn't appear when simulating the system with purely classical oscillators in section 4.3.1, which displays that various theoretical approaches are needed in order to reveal certain aspects of hybrid systems.

To account for losses and dissipation mechanisms, quantified by rate parameters γ_p and γ_{ok}, it is possible to extend the frequencies to be complex valued according to

$$\omega_p \rightarrow \omega_p - i\frac{\gamma_p}{2}$$

(4.12)

$$\omega_{0k} \rightarrow \omega_{0k} - i\frac{\gamma_{0k}}{2}$$

By solving the Schrödinger equation for each individual state with the complex valued frequencies, presented in (4.12), each corresponding time-dependent population probability will have a decay term according to

$$P_p(t) = |c_p(t)|^2 = |c_p(0)|^2 e^{-\gamma_p t}$$

(4.13)

$$P_{0k}(t) = |c_{0k}(t)|^2 = |c_{0k}(0)|^2 e^{-\gamma_{0k} t}$$

Note that it is troublesome to introduce dissipation when treating quantum mechanical systems since there is a requirement that real-valued observables can only originate from hermitian operators $\left(\hat{H}^\dagger = \hat{H}\right)$ [35]. Still the trick in (4.12), resulting in (4.13), works sufficiently well to describe important observations such as excitation weight distribution and coherence between the constituent parts in each collective state [59]. A more thorough

description on how to accurately account for dissipation in quantum systems is described in Section 4.3.6 where the so-called *Lindblad Master-equation* is presented.

By using complex valued energies presented in (4.12), each polariton energy eigenvalue will be represented by a complex number. Thus, the real part describes the energy of the state, whereas the imaginary part reflects the dissipation of the same state. It is furthermore convenient to assign an amplitude R and a phase φ to each $N + 1$ constituent parts within an arbitrary polariton state J $(1 \leq J \leq N + 1)$ according to

$$|\Psi\rangle_J = \left[R_p e^{i\varphi_p}, R_{01} e^{i\varphi_{01}}, \ldots \ldots, R_{0N} e^{i\varphi_{0N}} \right]_J \tag{4.14}$$

The indices p and $\{01, \ldots, 0N\}$ in (4.13) denote the cavity and emitter states respectively.

Spectra together with excitation weights and phases ($|R_k|^2$ and φ_k) for each constituent part, for the two bright polariton states and a random dark polariton state, may be seen in Figure 4.4. Note that the figure displays two different situations. First, a single cavity mode is coupled to *25* emitters (Figure 4.4 a) and secondly to *100* emitters (Figure 4.4 b).

First and foremost, by comparing spectra of bright states when $N = 25$ and $N = 100$, it is obvious that a more distinct hybrid mode formation occurs when $N = 100$. This phenomenon is attributed to the fact that the collective coupling strength, embedded in parameters ω_{B1} and ω_{B2} in expression (4.11), results in a higher number when the amount of emitters increases. In fact, the mode splitting increases according to $\Omega = \omega_{B1} - \omega_{B2} = 2\sqrt{\sum_{i=1}^{N} |g_i|^2}$ (when $\delta = 0$), as a result of larger amount of emitters. Note that this result coincides rather well with what was described with the classical coupled oscillator model in Section 4.3.1.

By likewise observing the phases and excitation weights of the bright states (upper- and lower polaritons) for both cases, we may further conclude that these states force all emitters to share the same phase (coherence) and a large majority of the excitation weight resides within the cavity mode (high photonic component).

Let us now turn the attention to the dark states displayed in Figure 4.4. First it is reasonable to conclude, from noticing the absence of collective phase behavior, that dark states are highly incoherent. The excitation weights indicate that the photonic component (cavity component) is very weak. The weights are moreover mainly distributed within a few of the emitter states, which can clearly be seen in the figure.

36

The presence of both coherent and incoherent polaritonic states will turn out to be one of the key aspects in describing inelastic relaxation within hybrid systems. This will be discussed more thoroughly in Section 4.4.
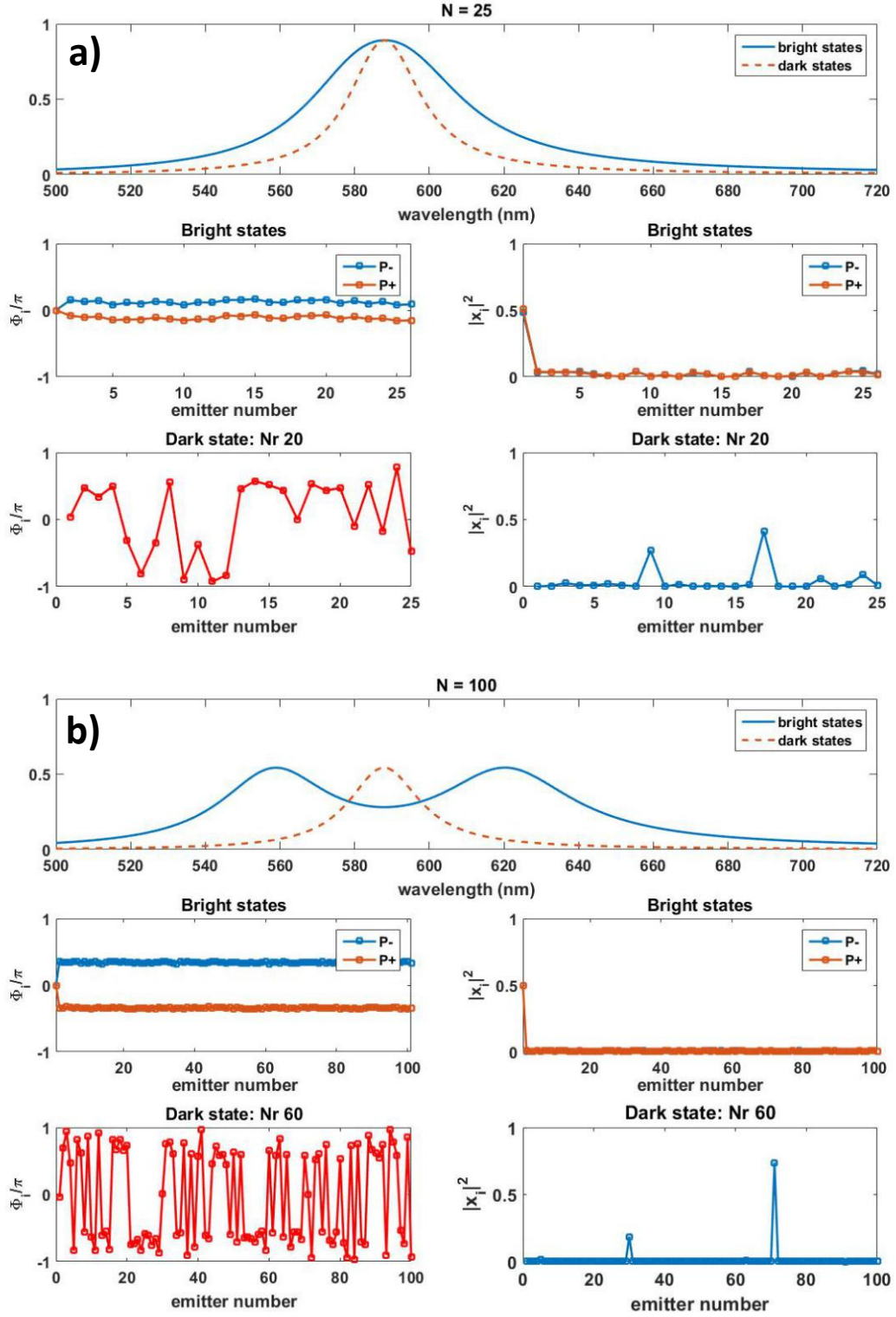
Figure 4.4 *Simulations of spectra, phases and excitation weights for both bright polariton states and a random dark polariton state. Note that the figure displays data where (**a**) N = 25 emitters are coupled to a single cavity, whereas (**b**) contains data where N = 100 emitters are coupled to a single cavity.*

4.3.3 Time domain dynamics within hybrid systems

In order to further understand the dynamics of a hybrid system some insights can be made by studying how each constituent part of the total system behaves in the time domain.

First we restrict ourselves to study a Hamiltonian of a cavity coupled to a single emitter on exact resonance. Note that this system is similar to what was presented in section 4.3.2, with the distinction that a single cavity mode is now coupled to a single emitter rather than N independent emitters.

The matrix representation of a Hamiltonian of a cavity-emitter system with resonance energy $\hbar\omega_R$ and coupling $\hbar g$, is described by

$$\hat{H} = \hbar \begin{bmatrix} \omega_R & g \\ g & \omega_R \end{bmatrix} = \underbrace{\hbar\omega_R\hat{\mathbb{I}}}_{\substack{uncoupled \\ resonances}} + \underbrace{\hbar g\hat{\sigma}_x}_{\substack{coupling \\ term}} \tag{4.15}$$

Here $\mathbb{I}$ and $\hat{\sigma}_x$ denote identity- and a Pauli x-matrix respectively. To construct a unitary time propagator $\hat{T}(t)$ we simply utilize exponentiation of the hermitian Hamiltonian matrix in (4.15). The fact that the matrices of the uncoupled resonances and coupling terms does commute ($[\hbar\omega_R\mathbb{I}, \hbar g\hat{\sigma}_x] = 0$), allow us to further exploit the Zassenhaus formula [35]. Together with Taylor-expansion, as well as the observation that $\hat{\sigma}_x^{2n} = \mathbb{I}$ and $\hat{\sigma}_x^{2n+1} = \hat{\sigma}_x$ ($n \in \mathbb{N}$), the time propagator can now be expressed according to

$$\hat{T}(t) = exp\left(-i\frac{\hat{H}}{\hbar}t\right) = \begin{bmatrix} e^{-i\omega_R t} & 0 \\ 0 & e^{-i\omega_R t} \end{bmatrix} \begin{bmatrix} \cos(gt) & -i\sin(gt) \\ -i\sin(gt) & \cos(gt) \end{bmatrix} \tag{4.16}$$

Note that in the case of non-zero detuning ($\delta = |\omega_{pl} - \omega_0| > 0$) the matrices for the uncoupled and coupled terms does not commute but rather result in a term according to

$$\left[\hat{H}_{uncoupled}, \hat{H}_{coupled}\right] = \hbar^2 g \begin{bmatrix} 0 & \delta \\ -\delta & 0 \end{bmatrix} \tag{4.17}$$

The exponentiation of the Hamiltonian in a case with non-zero detuning will consequently result in a more complex expression than in the case when cavity and emitter resonance energies coincide.

For the on-resonance case, a general expression for the wave function of the system is written according to

$$|\psi(t)\rangle = c_1(t)|1\rangle \otimes |g\rangle + c_2(t)|0\rangle \otimes |e\rangle \tag{4.18}$$

Here $c_1(t)$ and $c_2(t)$ are probability amplitudes for the excitation to be in the cavity or the emitter respectively. The ket-notations in (4.18) represent states with one cavity excitation with the emitter in the ground state ($|1\rangle \otimes |g\rangle$), and no cavity excitation with the emitter in the excited state ($|0\rangle \otimes |e\rangle$).

We now make the assumption that the excitation initially solely populates the cavity mode. This implies that the initial conditions of coefficients in (4.18) are $|c_1(0)|^2 = 1$ and $|c_2(0)|^2 = 0$. The time-dependent wave function may then be expressed, utilizing the time-propagator [35] described in (4.16), according to

$$|\psi(t)\rangle = \hat{T}(t)|\psi(0)\rangle = e^{-i\omega_R t}\cos(gt)|1\rangle \otimes |g\rangle - ie^{-i\omega_R t}\sin(gt)|0\rangle \otimes |e\rangle \tag{4.19}$$

From (4.19) we may further deduce the time-dependent population probabilities of both cavity and emitter according to

$$P_{cav}(t) = |c_1(t)|^2 = \cos^2(gt)$$

$$\tag{4.20}$$

$$P_{em}(t) = |c_2(t)|^2 = \sin^2(gt)$$

The time evolution of both cavity and emitter excitations population probabilities in a hybrid system, for different coupling-to-damping ratios based on (4.20), can be seen in Figure 4.5. Note that the damping terms in Figure 4.5 were introduced by applying the technique expressed in (4.13). Notice further how the Rabi oscillations within these figures resemble the time-dependent oscillations of the equilibrium-displacement coordinate for the cavity-oscillator in Figure 4.3 (b).
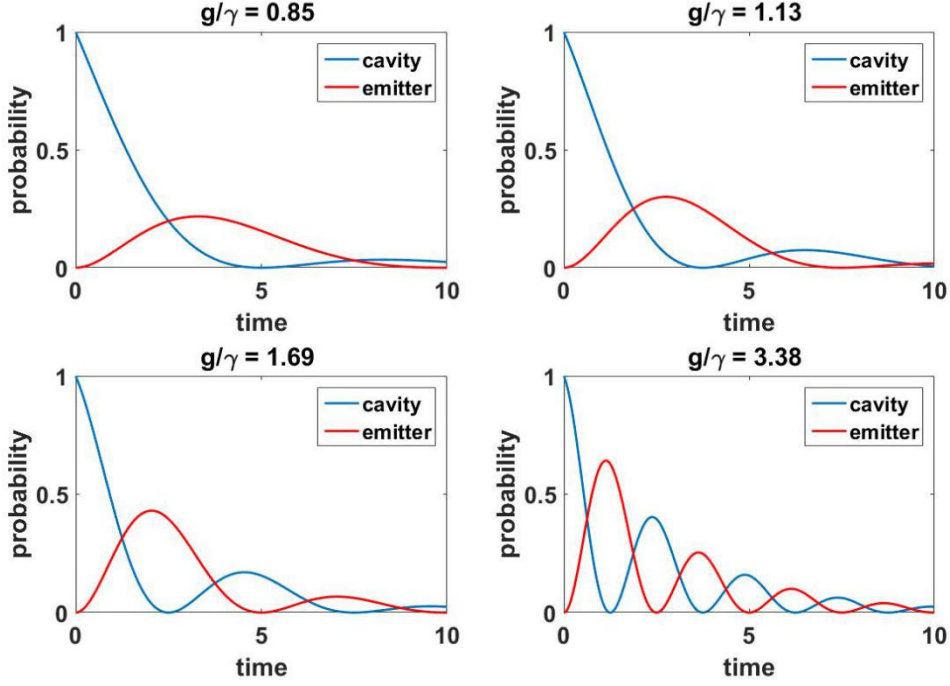
Figure 4.5. *Excitation probabilities for both cavity and emitter as a function of time for a hybrid system, with the excitation initially being exclusively in the cavity. Note the difference in coupling-to-damping ratio in each sub-figure. Time is in arbitrary units.*

The time evolution described in (4.19) and (4.20) was derived using ordinary Cartesian coordinates. It would be as valid to describe the time evolution of the system in the eigenbasis of the Hamiltonian in (4.15). From the time-dependent Schrödinger equation the time evolution of a quantum state is determined by

$$i\hbar \frac{\partial}{\partial t} |\psi\rangle = \widehat{H} |\psi\rangle \tag{4.21}$$

It is thus straightforward to write the Hamiltonian as $\widehat{H} = D^{-1} \widehat{H}_p D$, where D and $\widehat{H}_p$ are a matrix with eigenvectors and a diagonal matrix with eigenvalues respectively. Hence, it is suitable to rewrite (4.21) according to

$$i\hbar \frac{\partial}{\partial t} |\psi\rangle_p = \widehat{H}_p |\psi\rangle_p$$

with

$$\widehat{H}_p = \hbar \begin{bmatrix} \omega_+ & 0 \\ 0 & \omega_- \end{bmatrix} \tag{4.22}$$

$$|\psi\rangle_p = D |\psi\rangle$$

In this new hybrid-basis $|\psi\rangle_p$ the collective excitations are treated as new quantum objects (or quasiparticles), with their own wave functions containing information about their intrinsic properties. In accordance with the procedure in (4.19), a time-propagator approach for the expression of the wave function describing the polariton quasiparticles may be utilized. Such a wave function may then be expressed as

$$|\psi(t)\rangle_p = e^{-i\frac{\widehat{H}_p}{\hbar}t}|\psi(0)\rangle_p = e^{-i\omega_+t}|\psi(0)\rangle_{p+} + e^{-i\omega_-t}|\psi(0)\rangle_{p-} \qquad (4.23)$$

Notice that all dissipation terms have been omitted here within all calculations. The reason for this is as explained earlier simply to maintain hermicity of the exploited operators, which by the law of quantum mechanics is required in order to get real valued energies [35]. As can be seen from (4.23), the notion of Rabi oscillation is only valid in the initial basis but not in the new basis. In this basis there are no longer any cavity or emitter modes but rather an inseparable mixture of both, which behave as new quasiparticles referred to as cavity-emitter *polaritons*.

To explore different types of quantum effects and nonlinearities in hybrid systems, we need to push our derivations further and apply operator-based algebra. Then both cavity and emitter excitations may be described by creation- and annihilation operators. In upcoming Sections 4.3.4 – 4.3.7 more solid quantum mechanical approaches will be taken, with respect to Sections 4.3.1 – 4.3.3. The reason for this is to reveal effects such as nonlinear dynamics within hybrid systems.

4.3.4 Quantized cavity-field interactions with a quantum emitter

The interaction between a quantum emitter (atom, molecule, quantum dot etc.) and a spatially confined cavity field can initially be understood by studying an atomic electron in the presence of a quantized non-relativistic external electromagnetic field [55]. The resulting Hamiltonian for such a system may be written according to

$$\widehat{H} = \frac{\left[\hat{p} + e\widehat{A}(r,t)\right]^2}{2m} - e\phi(r,t) + V(r) \qquad (4.24)$$

where $\hat{p} = -i\hbar\nabla$, $\widehat{A}(r,t)$, $\phi(r,t)$ and $V(r)$ are linear momentum operator, field vector potential, field scalar potential and the atomic nucleus energy potential. By applying gauge invariance and selecting the *Coulomb gauge* ($\nabla \cdot \widehat{A}(r,t) = 0$) together with exploiting the

dipole-approximation $(\widehat{A}(r,t) \approx \widehat{A}(t))$, the Hamiltonian in (4.24) may be rewritten according to

$$\widehat{H} = \frac{\hat{p} \cdot \hat{p}}{2m} + V(r) - \hat{\mu} \cdot \widehat{E} \tag{4.25}$$

Here the parameter $\hat{\mu} = e\hat{r}$ describes the transition dipole moment operator for the quantum emitter. The last term in expression (4.25) describes interaction between the electron and the external electric field.

Finally, we may utilize a general expression for a quantized electric field inside a cavity, together with the *rotating wave approximation (RWA)* [55], and write the resulting Hamiltonian as

$$\widehat{H} = \widehat{H}_0 + \hbar g(\hat{c}\hat{\sigma}_+ + \hat{c}^\dagger \hat{\sigma}_-) \tag{4.26}$$

This is generally referred to as the *Jaynes-Cummings Hamiltonian* [60]. The first term in (4.26) relates to the intrinsic energy of both electron and cavity-field, and the second term corresponds to the interaction energy. The different interaction parameters are further explicitly expressed as

$$g = \mu \underbrace{\sqrt{\frac{\hbar\omega}{2\varepsilon_0\varepsilon V_m}}}_{=|E_{vac}|}$$

$$\hat{c} = \frac{\omega\hat{q} + i\hat{p}}{\sqrt{2\hbar\omega}} , \hat{c}^\dagger = \frac{\omega\hat{q} - i\hat{p}}{\sqrt{2\hbar\omega}} \tag{4.27}$$

$$\hat{\sigma}_+ = |e\rangle\langle g| , \hat{\sigma}_- = |g\rangle\langle e|$$

$g = coupling\ strength\ between\ cavity\ and\ emitter$

$\mu = transition\ dipole\ moment\ between\ ground\ and\ excited\ state\ of\ emitter$

$V_m = cavity\ field\ mode\ volume$

$E_{vac} = cavity\ vacuum\ field$

$\hat{c} = cavity\ field\ quantum\ annihilation\ operator$

$\hat{c}^\dagger = cavity\ field\ quantum\ creation\ operator$

$\hat{p} = cavity\ field\ linear\ momentum\ operator$

$\hat{q} = cavity\ field\ position\ operator$

$\hat{\sigma}_+ = emitter - to - cavity\ energy\ transfer\ operator$

$\hat{\sigma}_- = cavity - to - emitter\ energy\ transfer\ operator$

The cavity field mode volume (or effective volume) is a parameter, which quantifies the degree of spatial confinement of the cavity field [61]. The mode volume parameter may further be expressed as

$$V_m = \int \frac{\boldsymbol{E}(r) \cdot \boldsymbol{D}(r)}{max\{\boldsymbol{E}(r) \cdot \boldsymbol{D}(r)\}} d^3r = \int \frac{\varepsilon(r)|\boldsymbol{E}(r)|^2}{max\{\varepsilon(r)|\boldsymbol{E}(r)|^2\}} d^3r \qquad (4.28)$$

Parameters $\varepsilon(r)$, $\boldsymbol{D}(r)$ and $\boldsymbol{E}(r)$ in (4.28) are dielectric function, cavity displacement field and electric field vectors respectively.

Note that in the case of plasmonic metallic nanoparticles, the dielectric function is altered according to $\varepsilon(r) \rightarrow Re\{\varepsilon\} + 2\omega Im\{\varepsilon\}/\gamma$, where the parameter γ corresponds to the Drude damping parameter (see Supporting Information Paper I).

4.3.5 Several cavity quantum excitations coupled to a single quantum emitter

In situations where several cavity excitations are allowed, classical and semi-classical models often mediates inadequate outcomes in describing the resulting dynamics. Under these circumstances a non-classical theoretical approach is needed since the cavity field will be quantized [55].

In the case of near-field mediated coupling (which is the case in plasmon-exciton systems) it is suitable to choose a model, which describes how virtual particles tunnel back and forth between a resonant cavity and a two-level quantum emitter system. The Hamiltonian for such a system, with $N_c \geq 1$ cavity excitations and a single quantum emitter, can be described according to

$$\hat{H} = \hbar\omega_c \hat{c}^\dagger \hat{c} - \frac{1}{2}\hbar\omega_0 \hat{\sigma}_z + \hbar g(\hat{c}|g\rangle\langle e| + h.c.) \qquad (4.29)$$

Here, the operator $\hat{\sigma}_z$ is the Pauli z-matrix. The mode frequencies $\omega_\pm$ are found by solving the time-independent Schrödinger equation with the Hamiltonian in (4.29), which results in eigenvalues of the form

$$\omega_\pm = \omega_c\left(N_c + \frac{1}{2}\right) \pm \sqrt{g^2(N_c + 1) + \frac{\delta^2}{4}} \qquad (4.30)$$

As before, $\delta = \omega_c - \omega_0$ is the frequency detuning between cavity and emitter. To simplify this expression further we may limit ourselves to study the case where cavity and emitter resonance frequencies overlaps, i.e. $\delta = 0$ ($\omega_c = \omega_0 \equiv \omega_R$), which gives

$$\omega_\pm = \omega_R \left(N_c + \frac{1}{2}\right) \pm g\sqrt{N_c + 1} \tag{4.31}$$

Note that the splitting between the hybrid modes $\Omega = \omega_+ - \omega_- = 2g\sqrt{N_c + 1}$, is still rather similar to the same corresponding parameter produced from derivations in Sections 4.3.1 and 4.3.2, where either purely classical or semi-classical theoretical approaches were performed. Notice though that the number of cavity excitations influences the magnitude of splitting between the hybridized states. The applied models in previous sections did not reveal this information. Even though a quantum mechanical approach is required to reveal certain aspects of hybrid systems, it is important to point out how much of the basic dynamics that may be described by the classical and/or semi-classical models.

The corresponding eigenfunctions to the eigenvalues in equations (4.30) and (4.31) are wave functions of so-called *dressed-* or *hybrid states*

$$\begin{aligned}
|\psi_+\rangle &= \cos\theta\, |N_c\,,e\rangle + \sin\theta |N_c + 1\,,0\rangle \\
|\psi_-\rangle &= \cos\theta |N_c + 1\,,0\rangle - \sin\theta\, |N_c\,,e\rangle
\end{aligned} \tag{4.32}$$

The parameter θ is further defined as

$$\theta = \frac{1}{2}\arctan\left(\frac{2g\sqrt{N_c + 1}}{\delta}\right) \tag{4.33}$$

Hence, it is straightforward to deduce the probabilities for cavity and emitter excitation weights, in situations when the emitter is being initially excited/de-excited. The expressions for these probabilities yields

$$P_{+e} = \cos^2\theta\,, P_{-e} = \sin^2\theta$$

$$P_{+0} = \sin^2\theta\,, P_{-0} = \cos^2\theta \tag{4.34}$$

There is yet another interesting phenomenon to pay attention to, in the case where the cavity and emitter resonances completely coincides ($\omega_c \to \omega_0 \Rightarrow \delta \to 0$). From expression (4.33) it is evident that the resulting value of the parameter θ becomes $\frac{\pi}{4}$. By the relations in (4.34),

this indicates that the excitation is delocalized evenly over both cavity and emitter in the case of zero detuning.

Note that this condition is fulfilled for any value of $g > 0$, but it is only when the overlap between the two hybridized modes is negligible ($g > [\gamma_c, \gamma_0]$) that the system is considered to be in a *strong coupling* regime [23]. In such a coupling regime, the rate at which energy is transferred between the cavity and emitter overcomes any of the dissipation rates or decoherence processes within the system. As a result the probability for the excitation to be transferred back to the cavity, after it has been absorbed by the quantum emitter, is sufficiently large. Hence, the energy in the system has the ability to oscillate back and forth between the cavity and emitter several times (Rabi oscillations) before it finally decay and escapes to the surrounding medium.

A graphic illustration of a 2-level system inside an optical resonant cavity, together with energy levels for different amount of photon numbers within the cavity according to the Jaynes-Cummings model, can be seen in Figure 4.6. Note the strong nonlinear behavior of the system with regards to the number of cavity photons.
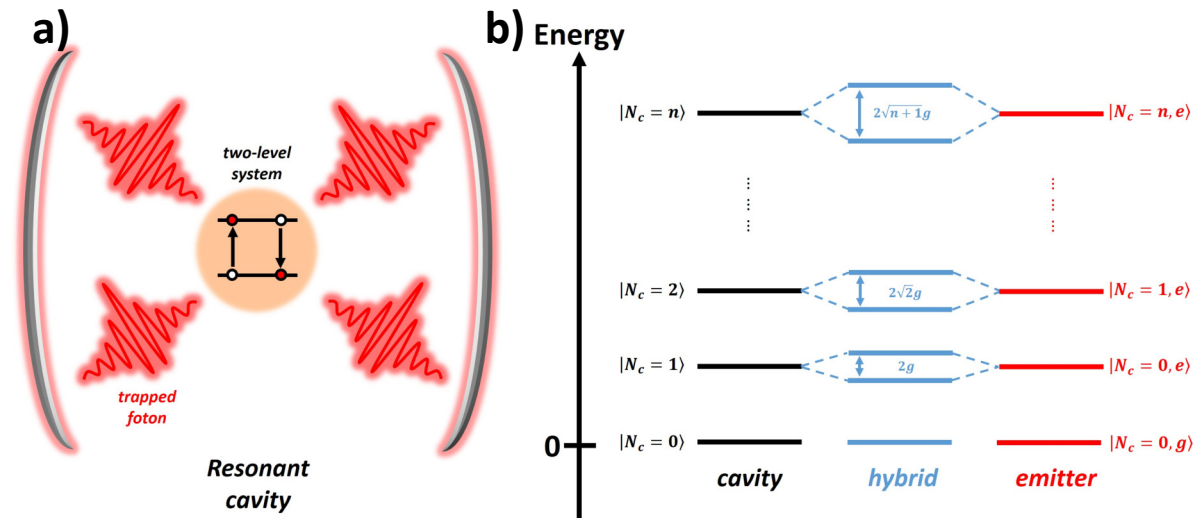

Figure 4.6. *(a) Drawing of a quantum emitter (two-level system) placed inside a resonant optical cavity. (b) The resulting energy ladder of both cavity and emitter as well as energies of resulting hybrid states (blue lines).*

4.3.6 Quantum cavity-emitter coupling with dissipation

The models derived so far in this thesis does not, in a quantum mechanical sense, accurately account for any dissipation process. In order to possess real energy eigenvalues a quantum mechanical Hamiltonian needs to fulfill the requirement of a hermitian operator. Thus, this is

crucial when applying a strict quantum mechanical approach to reveal dynamics within certain hybrid systems.

In order to account for both cavity and emitter energy dissipation (γ_c and γ_0) within quantum hybrid systems in a more accurate manner, it is possible to apply the so-called *Lindblad master equation* [62]. By letting cavity and emission creation/annihilation operators be denoted as in (4.27), this differential equation may generally be written on the form

$$\frac{\partial \hat{\rho}}{\partial t} = -\frac{i}{\hbar}\left[\hat{\rho}, \widehat{H}\right] + \mathcal{L}_{cavity} + \mathcal{L}_{emitter}$$

$$\mathcal{L}_{cavity} = -\frac{\gamma_c}{2}\left(\hat{c}^\dagger \hat{c}\hat{\rho} + \hat{\rho}\hat{c}^\dagger \hat{c} - 2\hat{c}\hat{\rho}\hat{c}^\dagger\right)$$

$$\mathcal{L}_{emitter} = -\frac{\gamma_0}{2}\left(\hat{\sigma}_+\hat{\sigma}_-\hat{\rho} + \hat{\rho}\hat{\sigma}_+\hat{\sigma}_- - 2\hat{\sigma}_-\hat{\rho}\hat{\sigma}_+\right) \tag{4.35}$$

with

$$\hat{\rho} = \sum_{i=1}^{N} p_i |\psi_i\rangle\langle\psi_i|$$

Here $\hat{\rho}$ is the reduced density matrix of the system comprised by N different states. The probability for each state is denoted as p_i. A typical spectral evolvement, and formation of hybrid states as a consequence of increased cavity-emitter coupling when dissipation is taken into account, is shown in Figure 4.7. The different cavity-emitter coupling values are indicated in the figure legend. The resonance energies as well as dissipation values of both cavity and emitter may be seen in the title of the figure.
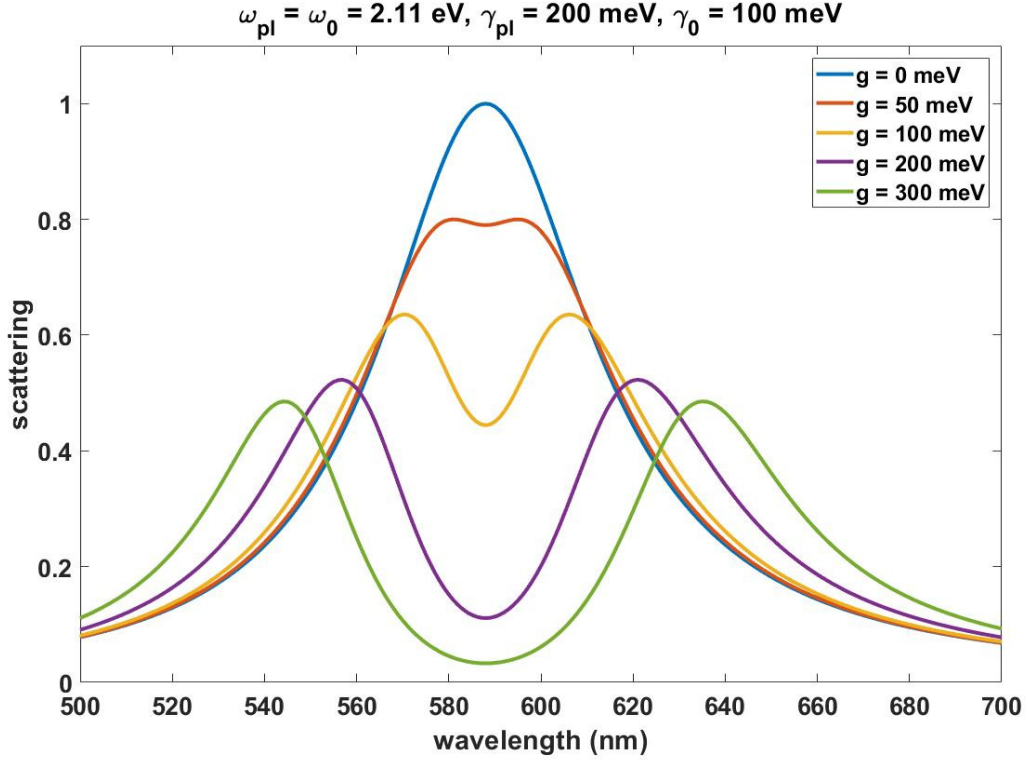
Figure 4.7. *Simulated spectra displaying how the features change from one Lorentzian shape to two distinct new hybrid modes when the coupling strength overcomes the dissipation rates of both cavity and emitter.*

4.3.7 The Dicke-model: The notion of a quantum coherent hybrid state

The previously described models, which mainly accounts for coupling between a resonating cavity and a 2-level system, does not account for the collective polaritonic excitation from a strict quantum mechanical point of view. For plasmon-exciton systems a massive amount of quantum emitters often occupies the cavity mode volume, and interact with a single cavity mode in a collective manner [63].

In this case it is suitable to construct collective quantum mechanical operators, so-called *Dicke-operators*, to describe the excitations within the system. When the number of quantum emitters N_0 is sufficiently large, these operators can be thought of as acting on a giant quantum oscillator system. The collective Dicke-operators may be expressed as

$$\widehat{D}_+ = \hat{b}^\dagger \left(N_0 - \hat{b}^\dagger \hat{b}\right)^{1/2}$$
$$\widehat{D}_- = \left(N_0 - \hat{b}^\dagger \hat{b}\right)^{1/2} \hat{b} \tag{4.36}$$

and

$$\widehat{D}_z = \widehat{b}^\dagger \widehat{b} - \frac{N_0}{2}$$

Operators $\widehat{b}^\dagger$ and $\widehat{b}$ are responsible for the creation and annihilation of the collective emitter quantum.

This theoretical approach is not used in any of the studies on which this thesis is based upon, but is still a rather important concept to be familiar with in order to broaden the knowledge of how hybrid systems are modeled with stricter quantum mechanical approaches. For more detailed information, see reference [63].

4.3.8 Anti-crossing characteristics

One of the most characteristic signatures for strongly interacting cavity-emitter systems is anti-crossing [64]. This entails that the spectral resonance positions of the two hybrid states never coincide, no matter what detuning the cavity-emitter system experiences.

The vacuum Rabi splitting in a hybrid system where dissipation terms are included is, according to (4.11) and (4.12), equal to the expression $\Omega = 2\sqrt{g^2 - \frac{(\gamma_c - \gamma_0)^2}{16}}$ at zero detuning. Parameters g, γ_c and γ_0 describe coupling strength and dissipation rates within the cavity and emitter respectively [59].

In experimental studies, anti-crossing is often based scattering data. It is important though to point out that one has to be a little bit careful when relying on anti-crossing from scattering data. It turns out that the information of anti-crossing in scattering is insufficient in order to conclude whether a system is in a strong coupling regime or not. There are several possible phenomena that give rise to anti-crossing features in scattering, such as *surface enhanced absorption* and *electromagnetically induced transparency (EIT)* [64]. In order to fully conclude what regime the system is operating in, one crucial property to investigate is if there are any simultaneous signs of anti-crossing in both scattering and absorption spectra.

In order to give a broad overview to different types of anti-crossing plots presented in the studies reported in Paper I – Paper V, situations where an optical cavity is coupled to both an exciton and a trion, are considered. A 3×3 Hamiltonian of the following form may then be utilized to simulate such systems according to

$$H = \hbar \underbrace{\begin{bmatrix} \omega_c & 0 & 0 \\ 0 & \omega_{01} & 0 \\ 0 & 0 & \omega_{02} \end{bmatrix}}_{\substack{resonance \\ energies}} - \frac{i\hbar}{2} \underbrace{\begin{bmatrix} \gamma_c & 0 & 0 \\ 0 & \gamma_{01} & 0 \\ 0 & 0 & \gamma_{02} \end{bmatrix}}_{dissipation} + \hbar \underbrace{\begin{bmatrix} 0 & g_{01} & g_{02} \\ g_{01} & 0 & 0 \\ g_{02} & 0 & 0 \end{bmatrix}}_{coupling\ terms} \tag{4.37}$$

The parameters in this matrix are cavity resonance frequency (ω_c) and dissipation rate (γ_c), together with exciton resonance frequency (ω_{01}), dissipation rate (γ_{01}) and cavity-exciton coupling parameter (g_{01}). Parameters $\omega_{02}, \gamma_{02}, g_{02}$ are trion resonance frequency, dissipation and cavity-trion coupling respectively. Note that any exciton-trion interaction is omitted in (4.37).

Simulated anti-crossing behavior for both cavity-exciton and cavity-exciton-trion systems (with various coupling strengths) can be seen in Figures 4.8 and 4.9. Note how the bending of the polariton branches ω_-, ω_m and ω_+ strongly depends on the strength of interaction parameters g_{01} and g_{02}.
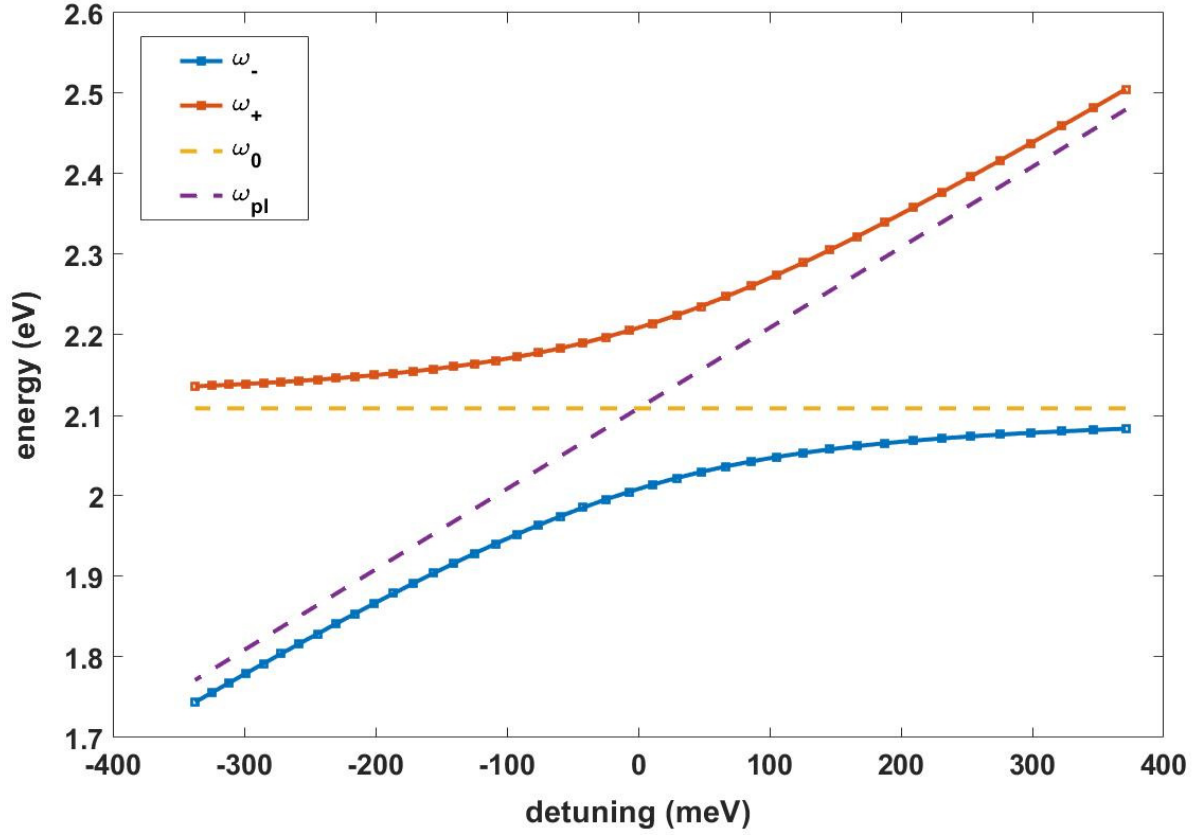
Figure 4.8. *Simulated plasmon-exciton polariton values, which indicates anti-crossing. The lines corresponds to upper/lower hybrid mode resonances (ω_+, ω_-) and plasmon/exciton resonances (ω_{pl}, ω_0) and the detuning is defined as $\delta = \omega_{pl} - \omega_0$.*
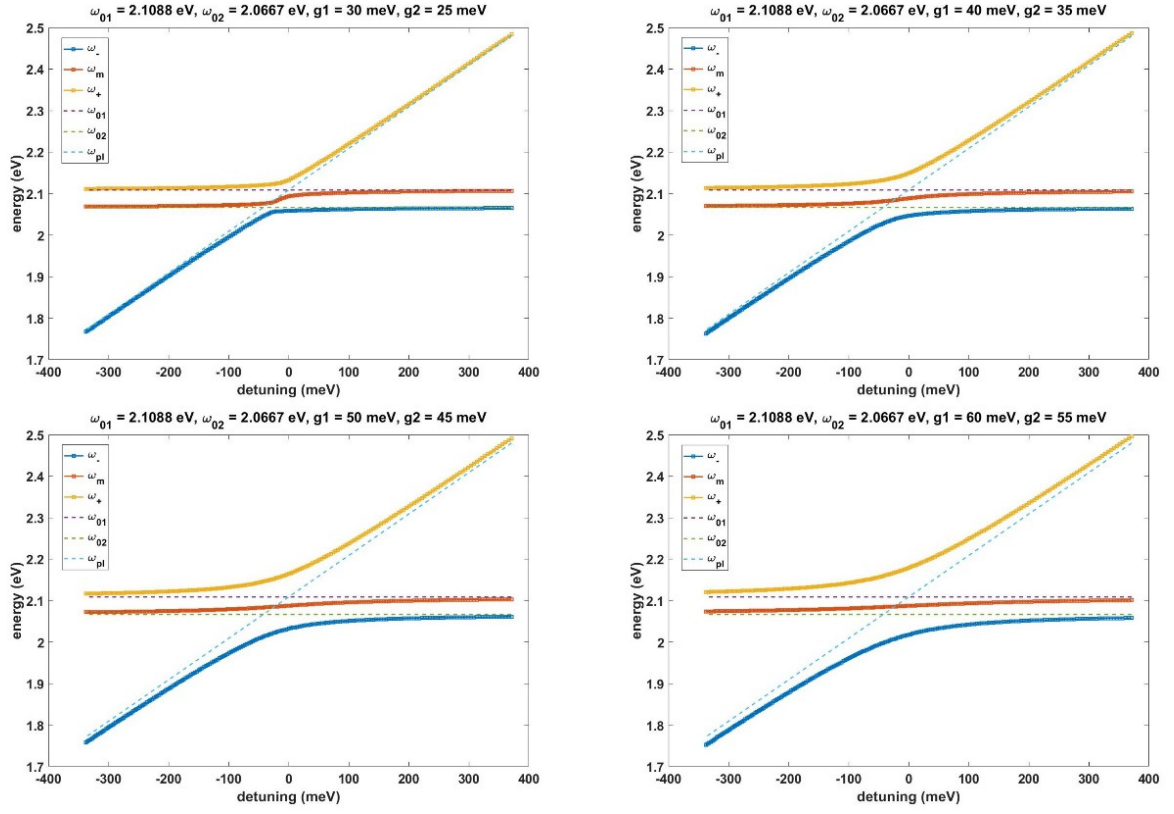
Figure 4.9. *Cavity-exciton-trion polaritons simulations with varying coupling strengths.*

4.4 Photoluminescence from strongly coupled hybrid systems

The excitations of bright polaritonic modes in strongly coupled plasmon-exciton hybrid systems have a lifetime in the range of femtoseconds (10^{-15} s) ($\tau_{\pm} = 1/\gamma_{\pm}$ where $\gamma_{\pm} \approx (\gamma_0 + \gamma_{pl})/2$). Molecular photoluminescence, which is an inelastic process, requires a timespan on the order of picoseconds (10^{-12} s) to occur [65]. However, experimental results indicates that photoluminescence is still observed in strongly coupled systems (see Paper II and III) and [66-68]. This suggests that the underlying inelastic relaxations paths in plasmon-exciton hybrid systems must be much richer than what can be described by the theoretical frameworks presented earlier in this section. In upcoming subsections 4.4.1 − 4.4.2, a plausible theoretical approach on how to describe inelastic energy relaxations within hybrid systems is presented.

4.4.1 Transitions between polariton states in hybrid structures

A suitable theoretical model to describe inelastic processes within a hybrid system is presented by Litinskaya *et al.* and Agranovich *et al.* [69-71].

According to these models we may initiate the derivation by introducing operators which accounts for creation and annihilation of intra-molecular phonons, located on the n:th molecule. Such an operator can be expressed according to

$$\widehat{H}_{phon} = E_{vib} \sum_n \hat{b}_n^\dagger \hat{b}_n \qquad (4.38)$$

Here the parameter E_{vib} describes the energy of a phonon quanta, and $\hat{b}_n^\dagger$ / $\hat{b}_n$ are creation/annihilation operators for phonons located at the n:th molecule.

Furthermore, the interaction between phonons and molecular excitations may be described by using the *Displaced Oscillator Model* [72], according to the following Hamiltonian

$$\widehat{H}_{ex-phon} = \chi E_{vib} \sum_n \widehat{N}_n \big(\hat{b}_n^\dagger + \hat{b}_n \big) \qquad (4.39)$$

In this expression, the parameter χ denotes the interaction strength between phonons and molecular excitations, and $\widehat{N}_n = \hat{B}_n^\dagger \hat{B}_n$ describes the number of incoherent molecular excitations at the n:th molecule.

In this basis, the ground state is simply described as tensor-products of exciton, photon and

phonon vacuum states by the ket-notation $|0\rangle \equiv |0, ..., 0\rangle_{ex} \otimes |0\rangle_{phot} \otimes |0, ..., 0\rangle_{phon}$. The operators described in (4.38) and (4.39) will become useful tools when aiming to develop a solid framework for transitions between coherent and incoherent polariton states, described in the upcoming sections.

4.4.2 Upper polariton decay to incoherent states

In the previously described basis it is straightforward to deduce the wave functions for both upper polariton ($|\psi_{UP}\rangle$) and incoherent molecular excitation states ($|\psi_n^i\rangle$) according to

$$|\psi_{UP}\rangle = \alpha_{UP}\hat{a}^\dagger|0\rangle + \sum_n \beta_n^{UP}\hat{B}_n^\dagger|0\rangle$$

$$|\psi_n^i\rangle = \hat{B}_n^\dagger\hat{b}_n^\dagger|0\rangle$$

(4.40)

The first term in the upper polariton wave function in (4.40) describes the photonic components via a weight parameter α_{UP} and a photonic creation operator $\hat{a}^\dagger$. The coefficients β_n^{UP} describes the excitation weight amplitudes of the n:th molecular excitation, within the upper polariton state [71].

One may further assume that the energy distribution of the molecular excitons, which has a width γ_0 that mainly arise as a result of structural disorder, can be described by a Gaussian function according to

$$\rho(E) = \frac{1}{\sqrt{\pi}\hbar\gamma_0} exp\left[-\frac{(E - E_0)^2}{\hbar^2\gamma_0^2}\right]$$

(4.41)

The parameter E_0 in (4.41) is the exciton resonance energy and the pre-factor is adjusted so that it results in unity when the function is integrated over all possible energy values.

The matrix element, describing how the exciton-phonon interaction term accounts for the transition between the upper polariton and the incoherent molecular states, may then be written by exploiting the expressions in (4.39) and (4.40) as

$$\langle\psi_n^i|\hat{H}_{ex-phon}|\psi_{UP}\rangle = \chi E_{vib}\beta_n^{UP}$$

(4.42)

By furthermore exploiting Fermi's golden rule, together with (4.41) and (4.42), the transition rate between the upper polariton and the incoherent states can be expressed as

$$W_{(UP \to inc)} = \frac{2\pi}{\hbar} \left| \langle \psi_n^{inc} | \hat{H}_{ex-phon} | \psi_u \rangle \right|^2 \rho(E_{UP} - E_{vib})$$

(4.43)

$$= \frac{2\sqrt{\pi} \chi^2 E_{vib}^2}{\hbar^2 \gamma_0} |\beta_{UP}|^2 exp \left[-\frac{[E_{UP} - (E_0 + E_{vib})]^2}{\hbar^2 \gamma_0^2} \right]$$

$$|\beta_{UP}|^2 = \sum_{n=1}^{N} |\beta_n^{UP}|^2 = \frac{g^2}{(E_{UP} - E_0)^2 + g^2}$$

(4.44)

Note that at in the case of zero detuning between the emitter and cavity resonances the term $(E_{UP} - E_0)$ in (4.44) equals g, which implies that the parameter $|\beta_{UP}|^2 = 1/2$ for every value of E_{UP}. This entails that the excitation is distributed evenly over both cavity and emitters at zero detuning. A result in agreement to the theoretical models previously described within this section. Note further that in the case of zero detuning, the transition rate in (4.43) is maximized when $E_{vib} = g$. This indicates that a phonon with vibrational energy equal to g will result in the highest possible transition rate for this particular process. To read more about these results causes implications on certain chemical properties within hybrid systems etc., see Paper IV.

4.4.3 Incoherent molecular excitation decay to lower polariton states

In order to describe the transition rate from an incoherent excited molecular state to the lower polariton state, a similar approach as in subsection 4.4.2 is utilized.

In this case the initial state is described by an incoherent excitation situated at a molecule denoted with number p. If we recollect the description where the excitation was transferred from the upper polariton to the incoherent molecular excitation together with a vibrational quantum, we are now in a situation where the phonon of the vibrational molecular excitation already has been emitted to the surrounding environment [70]. From this initial state the system may relax its energy either by radiative decay from the incoherent molecular states to the ground state, or transfer the energy to the lower polariton state [69]. In this section we focus on the latter process.

The final state in this process is a vibrational excited lower polariton state, with a phonon located at the s:th molecule. The initial and final wave functions in this process may be expressed according to

$$|\psi_p\rangle = \hat{B}_p^\dagger|0\rangle$$
$$|\psi_s\rangle = \hat{\xi}^\dagger\hat{b}_s^\dagger|0\rangle$$

$$(4.45)$$

As previously described, the operators $\hat{B}_p^\dagger$, $\hat{b}_s^\dagger$ and $\hat{\xi}^\dagger$ are incoherent excitation creation operator at molecule p, phonon creation operator at molecule s, and lower polariton creation operator respectively.

In order to simplify things further, we assume that the broadening of the exciton resonances in (4.41) is so small that it may be regarded as negligible. Then all incoherent molecular states will have approximately the same energies $(E_p \approx E_0)$ and we may write the transition rate, from an incoherent molecular excitation to a vibrational excited lower polariton state, as a mean value of the transition rate between all N molecular states and the lower polariton state according to

$$W(E_0) \approx \frac{1}{N}\sum_{p=1}^{N}W(E_p) = \frac{2\pi\chi^2 E_{vib}^2}{N\hbar}\frac{A}{(2\pi)^2}\int_{q_{min}}^{q_{max}}\frac{g^2}{g^2+(E_{LP}-E_0)^2}\delta[E_{LP}-(E_0-E_{vib})]\,dE_{LP} \qquad (4.46)$$

Here, the parameter A denotes the area of the cavity and $q_{min}/\ q_{max}$ is the minimum/maximum momentum for the lower polariton state.

By calculating the integral in (4.46) we arrive in a final expression for the transition rate, between the incoherent molecular excitations and the vibrational excited lower polariton state, as

$$W_{(inc\to LP)} = \frac{\chi^2 A E_{vib}^2}{2\pi\hbar}\frac{g^2}{g^2+E_{vib}^2} \qquad (4.47)$$

Note that in the case of zero detuning, both transition rates $W_{(UP\to inc)}$ and $W_{(inc\to LP)}$ in expressions (4.43) and (4.47) are proportional to the term $\chi^2 E_{vib}^2$, which indicates that both transition rates increases for high frequency phonons, if the vibronic coupling is not negligible.

A graphic sketch of the different relaxation routes, dictated by the previously described theoretical models, may be seen in Figure 4.10. Note that this figure displays the situation where the absorbed photon energies from the incident field are in resonance with upper polariton vibrational ground state. In reality, there is a set of phonon-bands that are available for each state rather than just a single active phonon [73], as well as broadening of energy

states rather than infinitely thin energy lines.

In the picture, illustrated in Figure 4.10, the upper polariton 0:th order vibrational state $|UP\rangle_{v=0}$ is initially populated due to absorbing a resonant photon. Due to the large number of incoherent states $(N-1)$, the energy may transfer rapidly (tens of femtoseconds) [70] to one of the first order vibrational incoherent molecular states $\left[|D\rangle_{v=1}\right]_k$, where $1 \leq k \leq (N-1)$. Applying Fermi's golden rule with a time-independent Hamiltonian requires a transition which preserves energy [35], so the energy of the 0:th order vibrational upper polariton state need to coincide with the energy of the first order vibrational incoherent molecular state. The system then relaxes down to the 0:th order vibrational incoherent state via emission of a phonon. Since the energy content now resides in a single molecular incoherent state, the system now has two main possibilities. Either it may undergo a radiative relaxation to its ground state by emitting a photon, or the energy may be transferred to the first order vibrational lower polariton state $|LP\rangle_{v=1}$. Note that this energy transfer is much slower (tens of picoseconds) [70] than the previously described one $(|UP\rangle_{v=0} \to |D\rangle_{v=1})$ since there is only one lower polariton state, compared with $N-1$ incoherent molecular states. Once the energy is transferred to the vibrational excited lower polariton state it will quickly (tens of femtoseconds) relax to the vibrational excited ground state $|GS\rangle_{v=1}$ via emission by a photon. The final relaxation to the 0:th order vibrational ground state $|GS\rangle_{v=0}$ will be via emission of a phonon.

Even though this picture is simplified it still gives a lot of insights on how inelastic relaxation processes may occur within strongly coupled plasmon-exciton hybrid systems.

Besides this model, there are various other theoretical frameworks that can account for inelastic relaxations within hybrid states.

An alternative model to describe some of the similar dynamics in hybrid systems is presented by F. Herrera & F. Spano, where the concept of so-called *dark vibronic polaritons* is introduced and explained [74].
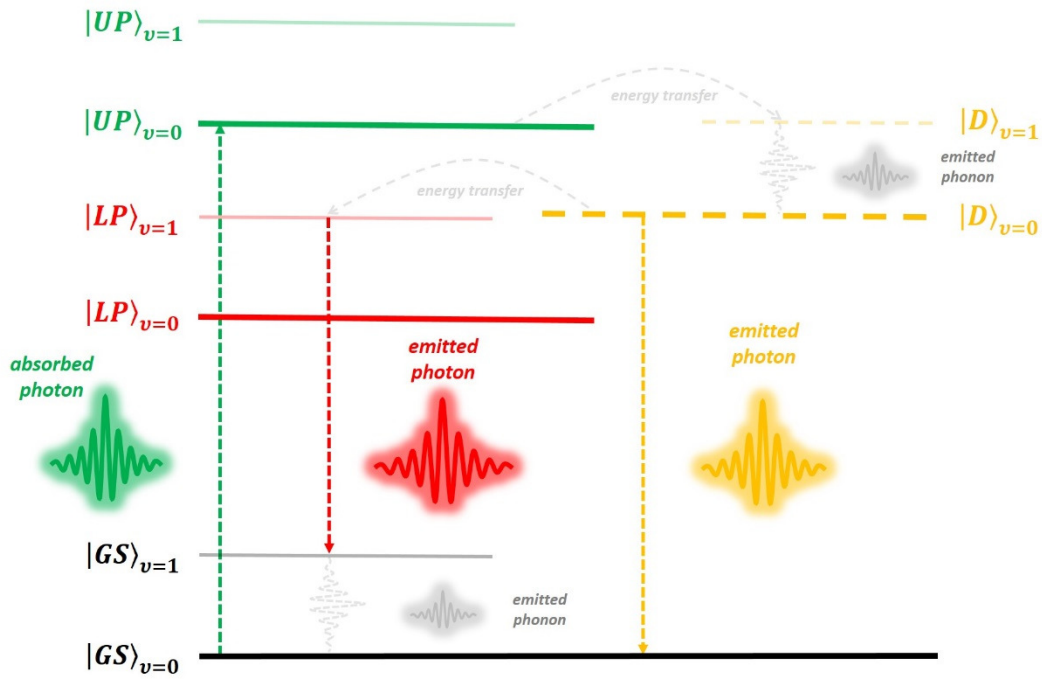
Figure 4.10. *A graphic sketch showing inelastic energy relaxation pathways in a hybrid system, together with both emitted phonons and photons for certain transitions. The different displayed states are: ground state GS, lower polariton LP, upper polariton UP and incoherent molecular states D. Each state has a noted vibrational quantum number attached which is either υ=0 or υ=1.*

4.5 Alterations in material-related properties due to strong coupling

Due to the fact that the coupling strength overcomes any dissipation and decoherence processes in a microscopic plasmon-exciton hybrid system, the coupling mechanism governs the new inherent properties of the system, and new paths for energy relaxation emerges. In the following section some alterations in material-related properties, due to strong light-matter interactions, are presented and described. The main considerations will entail experimental work done by B. Munkhbat *et al.* (see Paper IV) on suppression of photo-oxidation in organic chromophores, as well as work done by J. Cuadra *et al.* (see Paper V) on charged exciton polaritons in 2D monolayers of WS_2.

4.5.1 Suppression of photo-oxidation in organic chromophores

When molecular excitons are strongly coupled to an optical mode of a resonant plasmonic cavity, the possible routes for energy relaxation of that exciton differs substantially from the case with an isolated molecule. The implications of strong coupling on properties such as chemical reactivity, photochemical reactions and charge transport have recently proven to be immense [75, 76] and may be exploited for further use.

As seen in Figure 4.10, formation of polariton states includes both coherent (upper- and lower polaritons) and incoherent states (indicated with $|D\rangle$ in the diagram). Moreover, it turns out that yet another state appears which is lower in energy than the lower polariton (see Paper IV). This state makes the molecular part of the hybrid system highly sensitive to oxidation, and is categorized as a triplet state, which will be further elaborated on in Section 5.1.3. The study reported in Paper IV describes how the competition between transition rates, of the lower polariton and the photo-reactive triplet state, may regulate the photo-degradation mechanisms of the molecules. In the case of an isolated molecule, there are no alternative relaxation routes than those dictated by the intrinsic properties of the molecules energy band structure.

As a result, suppression of photo-oxidation in organic chromophores occurs upon strong plasmon-exciton coupling, which improves the photo-stability of the molecules to as much as 100 times at certain conditions (see Paper IV). This is due to the fact that the depopulation of state $|D\rangle_{v=0}$ becomes more efficient via the lower polariton than via the highly photo-reactive triplet state.

It turns out that the photo-oxidation suppression depends on various properties such as coupling strength between the plasmonic cavity and the emitters, but also on detuning

between the cavity and molecular exciton resonances. These findings may be of importance for the performance and improved stability of optical devices, which incorporate organic dye molecules.

4.5.2 Tuned charged plasmon-exciton polaritons in semiconducting 2D materials

As mentioned in Section 3.3.4, the trion quasiparticle, which is a supported excitation at cryogenic temperatures in many 2D materials (especially in transitional metal dichalcogenides), enables net non-zero charge transportation. Since this type of quasiparticles may be strongly coupled to a plasmonic cavity, its properties may be manipulated and controlled via an external light source (see Paper V). Active control of electrical properties has so far been demonstrated in several studies [77, 78], as well as cooling and lasing of plasmon-exciton polaritons [79, 80].

The properties described above show great promise for construction of macroscopic coherent polariton states that will be composed of a coherent mixture of plasmons, excitons and trions. This might in turn be useful in charge transport and optoelectronic devices by boosting the carrier mobility.

The new degree of freedom of charged polaritons may furthermore be useful for light-harvesting and light-emitting devices, as well as for strong photon-photon interactions (see Paper V). Even though the experimental results, presented by J. Cuadra *et al* (see Paper V), requires cryogenic temperature environments and does not provide direct practical utilization at room temperature, it gives a thorough insight into the dynamics and possible usage of electrically charged polaritons at the single nanoparticle level.

Chapter 5

Experimental Methodology

In this section various experimental techniques and methods, used during my doctoral studies, are presented and explained. This section is divided into parts concerning a diverse set of optical and SEM categorization techniques, as well as fabrication of the nanoscale hybrid systems.

5.1 Optical and spectroscopic measurements

Depending on what type of information you are interested to reveal about a nanoscale system, different optical methods will be applicable. If the sought for properties are elastic photo-response, the concept of dark-field scattering microscopy is most suitable. If the goal on the other hand is to reveal inelastic photo-responses, fluorescent microscopy is to prefer.

In this subsection various optical methods and concepts, exploited to categorize properties within nanoscale hybrid systems at various environmental conditions, are presented and described.

5.1.1 Dark-field scattering microscopy

When studying the optical properties of single nanoparticles it is very crucial to make sure that the registered signal originates from the actual nanostructure rather than from unwanted scattering sources in the nearby surroundings. Due to the remarkable ability of noble metallic nanostructures to strongly interact with certain frequencies of visible light (via LSPR resonances, see Section 3.1), the photons scattered by such nanostructures often considerably outnumbers those of its surrounding regions.

In order to register photons that have been scattered by nanoparticles, rather than photons that have been transmitted through and/or reflected from the substrate etc., one may exploit the following procedure:

By ensuring that the incident photons hits the substrate with and angle greater than that of the corresponding numerical aperture of the collection objective, all purely transmitted photons that didn't interact with the sample will not be collected. Since the path of photons, which wasn't scattered by the sample, will be unperturbed they will proceed with the same angle after hitting the sample as before.

However, photons that did interact with nanoparticles will be scattered in a wide range of angles and a great portion will be collected by the objective. The concept of dark-field scattering is illustrated in Figure 5.1. The illustrated optical path from source to detector in this figure can be described in the following way:

Parts of the light generated by the lamp source are blocked so that the only light that reaches the condenser lens will do so far away from its optical axis. Hence, the light transmitted through the condenser lens will be highly refracted and hits the substrate with nanoparticles at high incident angles. After this point we may divide the light as being either scattered or non-interacting with the plasmonic nanoparticles. As previously described, the non-interacting light will continue its path at same high angles as it previously hit the sample with, whereas the scattered light will consist of photons propagating in a wide range of angles.

As indicated in Figure 5.1, it is only a part of the scattered light that will be collected by the objective. Thereafter the collected light is directed to microscope oculars and/or detectors. A liquid crystal filter together with a CCD (charge-coupled device) camera is moreover depicted, which is the basis for the so-called *hyper spectral imaging technique*. A concept described more thoroughly in sections 5.2 and 5.2.1.
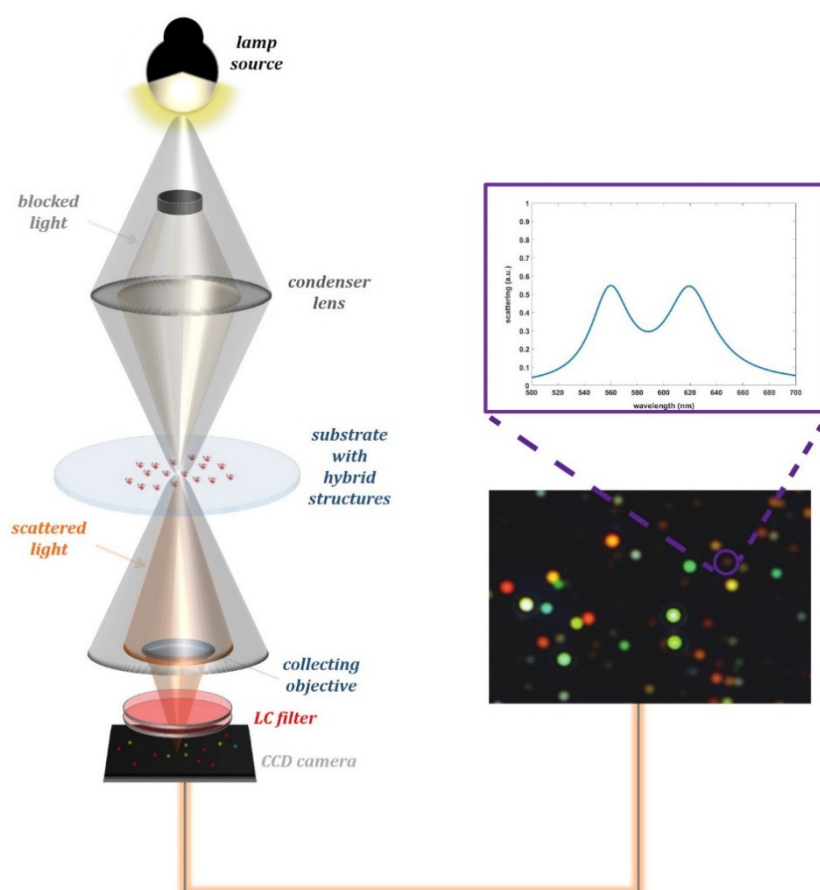
Figure 5.1. *Schematic illustration of the dark-field scattering principle. The incident light hits the substrate at high enough angles so that the collective objective is unable to capture any non-diffracted light.*

5.1.2 Dark-field scattering at cryogenic temperatures

In order to perform dark-field scattering measurements from single nanoscale hybrid structures at cryogenic temperatures, a cryostat chamber is needed (see Figure 5.2 a).

For these types of measurements an opaque silicon substrate with a 55 nm thick layer of SiO_2 on top were used to enable sufficient heat conduction between the cryostat cold-finger and the substrate. To additionally improve the conduction between the substrate and the cryostat cold-finger, a thin layer of cryogenic high vacuum grease was applied. Plasmon-exciton hybrid structures were thereafter applied to the substrate from an aqueous solution by drop casting according to a well-established recipe, which results in well separated isolated single hybrid systems. Afterwards an external light source was introduced from the side at high incident angles. This was done so that the purely reflected light wouldn't be detected by the objective (see Figure 5.2 b). In order to have a high enough signal-to-noise ratio, an intense laser driven white-light source (*Energetiq LDLS^{TM}*) was loosely focused towards the substrate to a region where hybrid nano-structures were dispersed. Then, scattered light was detected by the microscope objective.

To sustain a high vacuum environment, which is needed to avoid temperature leakage and hence also to establish stable cryogenic temperatures, a thick (1.6 mm) glass window is required to separate the inside and outside of the cryostat chamber. The introduction of a thick glass window gives rise to several disadvantages when it comes to optical measurements. First and foremost, the distance between the collection objective and the sample need to be increased since the substrate is located inside the cryostat chamber. Most high magnification dark-field objectives have a rather short working distance, which thus implies that plenty of ordinary microscope dark-field objectives cannot be utilized. Moreover, the glass window acts as a disturbance to the focusing of the incident light, and hence a microscope objective with a correction ring (*Nikon S Plan Fluor ELWD 20x/0.45*) is needed in order to overcome any unwanted optical aberrations. All these requirements need to be fulfilled in order to get a clean detectable optical signal, which makes the amount of possible microscope objectives rather limited.

In our case, the previously mentioned 20× magnification resulted in substantial signal-to-noise to resolve the crucial spectral morphology from light scattered by individual hybrid nanoscale systems. Moreover, this setup enabled thorough studies on alterations in dark-field scattering from nanoscale hybrid systems with respect to changes in temperature, ranging from 4 to 300 K. Most often, dark-field scattering spectra were also compared with inelastic

photoluminescence spectra to get a broader picture of the different relaxation paths within the system.

A more detailed description of how to exploit photoluminescence for microscopic and spectroscopic purposes may be found in the upcoming section.
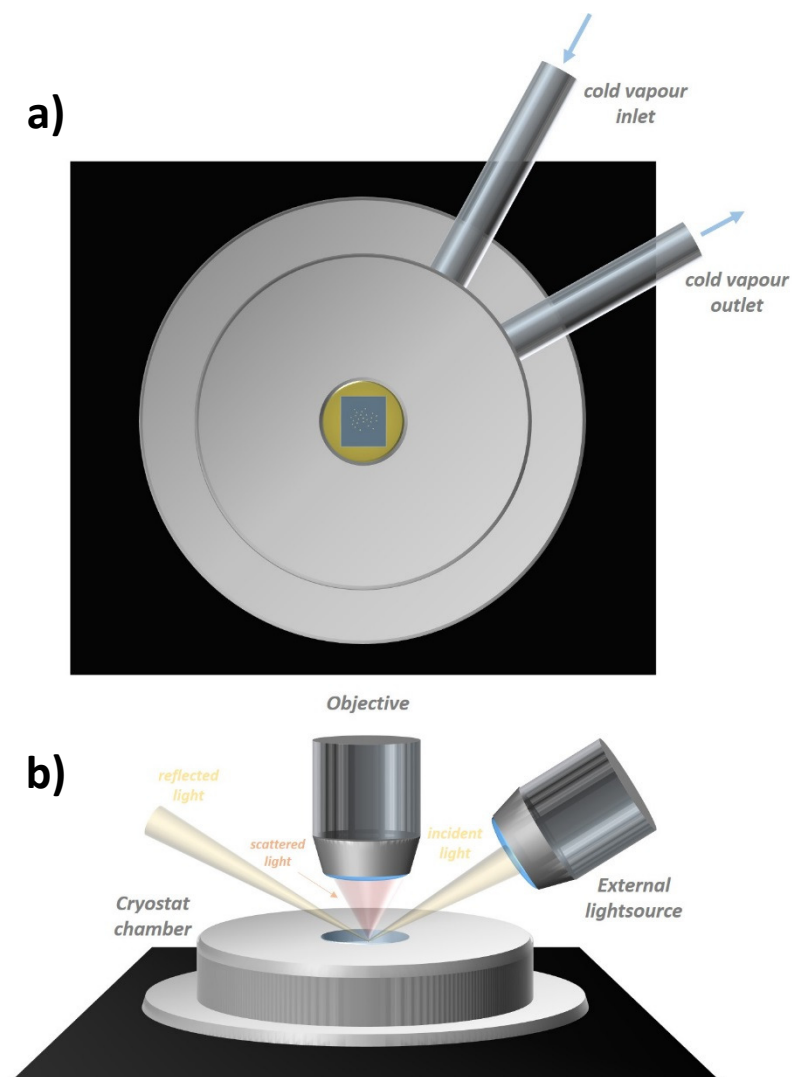

Figure 5.2. *(a) Schematic drawing of a substrate positioned within the cryostat chamber beneath the glass window in the center of the image. The sketch moreover displays how cold liquid N_2/He vapor is inserted to cool the system to cryogenic temperatures. (**b**) Schematic side view of how dark-field scattering can be achieved by using an external light source at rather high incidence angles.*

5.1.3 Fluorescence microscopy and spectroscopy

To get a deeper picture about intrinsic dynamics within microscopic entities, such as molecules and quantum dots, it is important to understand what different possibilities such systems have to relax when it transfer from a higher excited to a lower excited energy quantum state.

The energy levels of such systems are determined by both electronic and vibrational excited states. Each electronic state (ground state as well as excited states) has a multitude of additional vibrational excited states [43]. This entails that a molecular electron may absorb a certain amount of energy that forces it to occupy both a higher electronic and a non-zero vibrational energy level. The energy relaxation from the excited to a lower vibrational level, within the same electronic level, is accompanied with releases of vibrational quanta (*phonon*). These types of mechanisms are referred to as being *non-radiative* relaxations since no photon is emitted during the process.

Different molecules/quantum dots etc. have different abilities to emit fluorescent light due to differences in properties such as molecular band structure [81]. In order to quantify this ability one often uses the notion of *quantum yield* [82]. This term can basically be thought of as the ratio between the amount of emitted photons and amount of absorbed photons.

In order to visualize the different inelastic processes in which excited electrons in a molecule/quantum dot etc. can relax, the so-called *Jablonski diagram* [83] is suitable to use. Such a diagram is displayed in Figure 5.3 (a). The diagram shows absorption (blue arrows), fluorescence (green arrows) and phosphorescence (purple arrows). The latter is the slowest process, which in some cases takes a long time to fully occur [84]. Moreover the diagram illustrates electronic states which all have additional vibrational states. Different possible transitions (internal conversion, intersystem crossing and relaxation of vibrational phonon quanta) within the system are also indicated with arrows. Internal conversion entails the process when a system makes a transition from a higher electronic state to a lower electronic state in a non-radiative manner [85]. Intersystem crossing refers to the process where a system makes a transition from a singlet-state to a triplet state or vice versa [86]. As seen in this figure there are two main divisions within the diagram, that is *singlet-* (S_0, S_1, S_2) and *triplet* (T_1) excited states. What is indicated by these terms is related to the quantum mechanical spin momentum of that particular state. A singlet state simply indicates that all spin-momenta within that state add up to zero [35].

Figure 5.3 (b) illustrates the concept of the experimental setup (exploited in Paper I-V) in

which fluorescent signals were measured and studied. The optical path illustrated in Figure 5.3 (b) may be explained as follows:

Collimated white light (or direct monochromatic light from a laser source) is sent through an excitation filter in order to make sure that monochromatic light excites the nanoscale systems. Depending on which energy state within the system you want to excite, different laser excitation energies may be exploited to resonantly pump a certain transition.

After the excitation filter has extracted monochromatic components from the white light, the beam hits a dichroic mirror, which will reflect photons towards the sample. Next the collimated light beam is focused by the microscope objective on to the substrate where the nanoscale systems reside. After the hybrid systems have been excited with monochromatic light they will both scatter elastically and undergo inelastic relaxation processes. Both processes will produce light radiated in several possible directions, but it is only the part of this light that is captured by the microscope objective that will be detected. The beam collected by the microscopes collecting lens will yet again be collimated and will once again pass through the dichroic mirror. Note that at this stage the light beam is comprised by both elastically scattered light as well as light emitted via inelastic processes.

Finally the light beam will pass through an emission filter that is tuned to only transmit light, which originates from an inelastic energy relaxation. In other words, it differs in wavelengths from the elastically scattered light. In this manner all elastically scattered light will be filtered out and the signal projected on to the detector will consist solely of inelastic components. As mentioned, since plenty of processes will be elastic this technique provides a rather high signal-to-noise value, which is beneficial especially when studying emitted light from isolated single particle nanoscale hybrid systems.

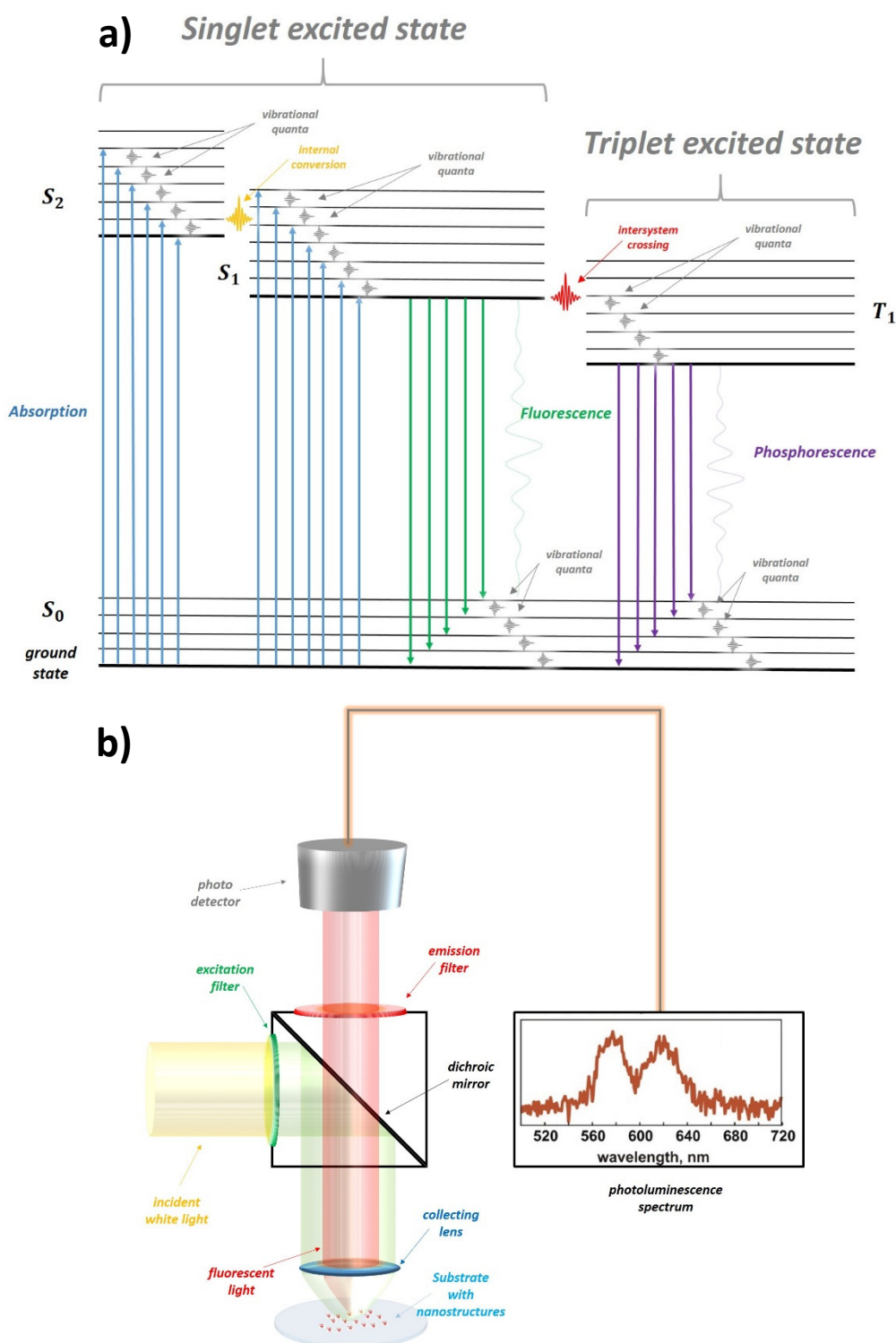In Figure 5.3 (b) a typical fluorescence spectrum from a strongly coupled plasmon-exciton hybrid is displayed.

Figure 5.3. (*a*) *Schematic Jablonski diagram drawing of different inelastic relaxation routes in a microscopic system. (**b**) Set up principle for measuring photoluminescence from single hybrid systems.*

5.1.4 Fluorescence lifetime measurements

The fluorescence lifetime (abbreviated FLT) is an intrinsic property independent on factors such as concentration of fluorophores, excitation laser intensity and absorption cross-sections. This property rather depends on external environmental factors [87, 88]. Such factors are temperature and presence of resonant cavities or other types of fluorescence quenchers [88]. There are some different methods in determining the FLT of a certain fluorophore. This property is possible to measure both in time- and frequency domain. In the time domain the FLT is defined as the timespan it takes for a population to decrease to an exponential fraction ($^1/_e \approx 36.6 \%$) of its initial value. This decay process occurs via losses of energy through fluorescence and other non-radiative relaxations. The decay time-span for dye molecules may vary significantly but usually happens in picoseconds ($\sim 10^{-12}$ s) to hundreds of nanoseconds ($\sim 10^{-7}$ s). A typical spectral feature of a lifetime curve can be seen in Figure 3.6, which was previously presented within section 3.2 when molecular dynamics where presented and discussed.

The study, reported in Paper III, utilized FLT measurements in order to reveal how relaxation processes changes when a dye molecule is strongly coupled to a resonant plasmonic cavity, in contrast to an isolated system. This information might reveal further details on the intrinsic dynamics within nanoscale hybrid systems and is crucial in order to get a deeper picture about strong coupling dynamics in plasmon-exciton systems.

5.1.5 Specifications on optical measurements from single hybrid systems

Dark-field scattering and fluorescence from single particle-dye systems at room temperature were, in studies presented in Paper I and IV, measured in an inverted microscope (Nikon TE-2000E) equipped with variable numerical aperture oil immersion objective (100x, NA = 0.5-1.3, Nikon). A tunable liquid crystal filter (VariSpec, 400-720 nm) that is transparent for light only at certain wavelengths and linear polarization was used together with an iXon EM-CCD detector (Andor) to perform hyper spectral imaging (see further details in subsection 5.2.1). Nearly isotropic in-plane polarization response of the nanoprisms justifies usage of the tunable filter in a single polarization channel. The transmission window of the exploited liquid crystal filter was 10 nm. The liquid crystal filter was set to perform wavelength steps of 1 nm between successive images and synchronized with the CCD-chip. Hyper spectral images (described in detail in section 5.2.1) were recorded in sequences with different wavelength intervals for both dark-field and fluorescence measurements. Only single nanoparticle data was analyzed in all conducted studies (Paper I-V).

For dark-field scattering measurements at room temperature, a tungsten halogen lamp was used as a light source to illuminate the sample. Even when driven at maximum power, the light intensity from the lamp was still low enough to ensure no significant photo-degradation of the dye molecules. For fluorescence measurements all samples were illuminated with either solely 532 nm, or with 532/568/640 nm laser wavelength excitations.

In the case of cryogenic measurements (Paper II, Paper III and Paper V), all dark-field scattering measurements were conducted and recorded according to the procedure described in section 5.1.2. In the case of recording photoluminescence from a sample located within the cryostat chamber depicted in Figure 5.2 (b), a laser beam was sent through the back port of the microscope and the fluorescent signal was thereafter filtered out utilizing the principle displayed in Figure 5.3 (b).

5.1.6 Correlation of dark-field and scanning electron microscopy images

High-vacuum scanning electron microscopy (SEM) with 2-5 kV acceleration voltages were used for imaging single nanoscale hybrid systems. Within the study described in Paper I, the particles were applied on top of a copper-grid substrate containing several distinct hollow quadrants. Each quadrant was supported with a very thin membrane on which the particles, dispersed in a solution, finally landed when a droplet was applied to the substrate. Furthermore, in the center of the copper-grid an asymmetric alignment mark was present which enabled to map out the quadrant of interest where a certain particle was located. Based on SEM imaging, each particle inside a given quadrant was correlated with a corresponding dark-field scattering optical image.

For measurements conducted inside the cryostat chamber (see Papers II, III and V), the nanoscale hybrid systems were instead applied on to a silicon substrate with a ~50 nm SiO_2. As described in section 5.1.2, such substrates were chosen in order to improve the heat conductivity between the cold-finger of the cryostat and the substrate. In a similar manner as with the copper-grid structures, different marked quadrants were marked on to the substrate via electron beam lithography. This is in order to relocate a specific nanoparticle and compare its dark-field scattering optical image with SEM imaging, in a similar manner as with the copper-grids.

A correlation between a dark-field scattering optical image and the corresponding SEM image can be seen in Figure 5.4. This specific example is done when hybrid systems are dispersed on to a Si/SiO_2 substrate. The difference in color between different particles in dark-field scattering is attributed to difference in aspect ratio of different nanoprisms, as dictated by
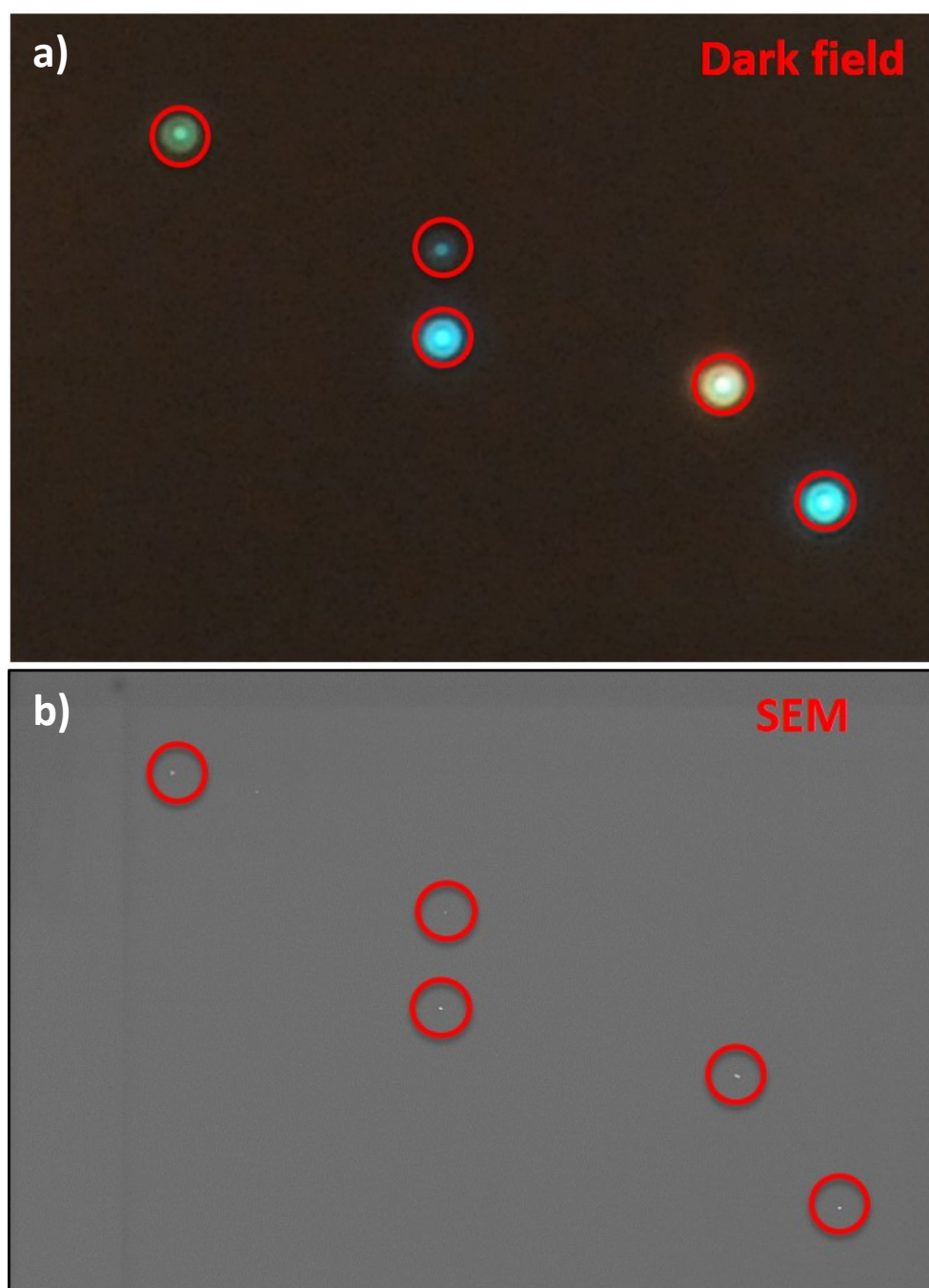
equation (3.10).

Figure 5.4. *Correlation between (**a**) dark-field scattering and (**b**) SEM images. This particular example show five well isolated single nanoscale plasmon-exciton hybrids of varying sizes, located on top of a silicon substrate with 50 nm of SiO₂ evaporated as a top layer.*

5.2 Liquid crystal tunable filter

In optics and spectroscopy it is of great importance to study the intensity of different frequencies in a signal. Ordinary spectrometers do this by utilizing gratings to filter out different frequency components within an optical signal [89]. There is however alternative ways to extract spectral information about light scattered from single nanoscale objects. The measurements conducted throughout my research have often been focusing on studying how spectral information changes for a single nanoscale hybrid system, when factors like temperature are altered. A wise and beneficial technique is then to use what is called *Hyper-spectral imaging technique,* which is described more thoroughly in section 5.2.1.

This technique is based on extracting spectral information from snapshots of images, taken with different transmission filters placed in front of the detector. Rather than having static filters that need to be exchanged between every recorded image, it is highly preferable to use *liquid crystal tunable filters (LCTFs).* Such a device is an electronically tunable transmission filter where it is possible to select monochromatic transmission through the filter via an external input [90-92]. Liquid crystal filters are often based on a so-called Lyot filter, see Figure 5.5. As seen in the figure the Lyot filter consists of a liquid crystal cell, a fixed retarder and two linear polarizers. Note that this figure only shows the basic stage of the Lyot cell and do not describe the liquid crystal device in its entirety. For instance, in a liquid crystal the fixed retarder is replaced with a variable retarder in order to get selective spectral tunability. This tunability aspect is one of the most crucial components of hyper spectral imaging, which will be addressed later on in section 5.2.1 within this thesis.

The net transmission through the filters within the Lyot-cell in Figure 5.5 can be expressed utilizing the following expression

$$T(\lambda) \sim \prod_{n=1}^{N} \cos(nk_s\lambda) \tag{5.1}$$

Here, $k_s = \frac{2\pi}{\lambda_s}$ and N is the target k-vector and number of filters used to create the net transmission profile respectively. The transmission profile for three different values of λ_s with $N = 10$, dictated by expression (5.1), can be seen in Figure 5.6.
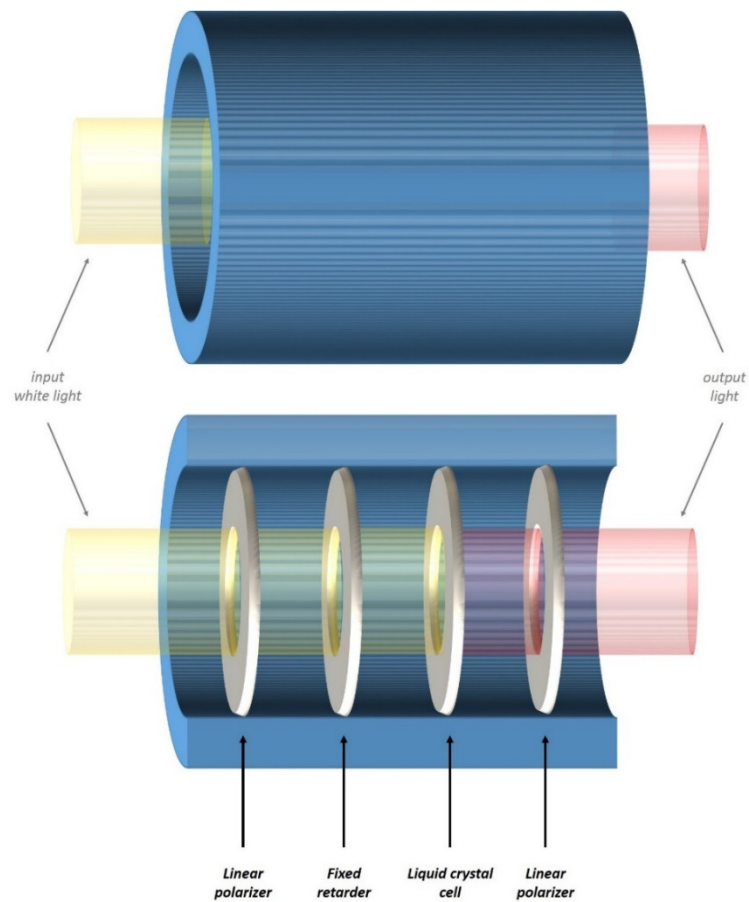
Figure 5.5. *The inner structure of a Lyot filter, used as the principal for the liquid-crystal filter device. The input light consists of white light and the output resembles monochromatic light.*

The linewidths of these transmission peaks are dependent on *N* in a manner that the more filters you chose, the more distinct and narrower the transmission line will be. However, in reality the transmission through each individual filter is not lossless, which indicates that in order to get a sufficient signal the amount of filters cannot be infinite, but rather needs to be restricted.
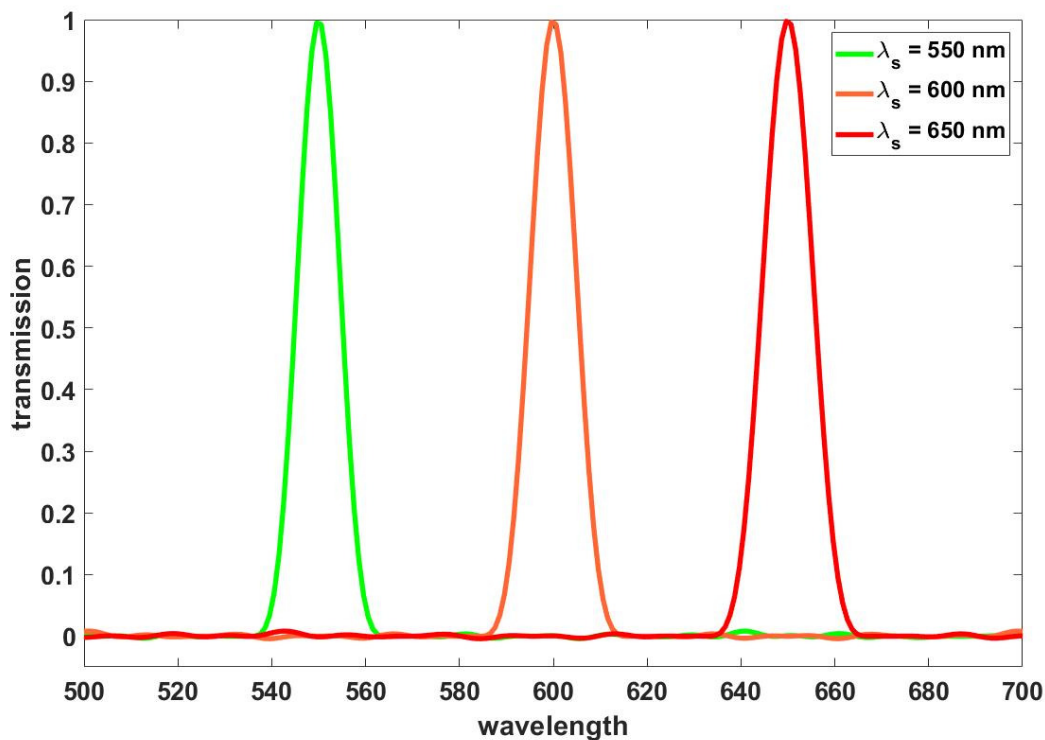
Figure 5.6. *Lyot-cell transmission spectra based on expression (5.1).*
The different target wavelengths are depicted in the figure legend. All
plotted spectra are based on an amount of N = 10 filters.

5.2.1 Utilization of tunable liquid crystal filters for hyper spectral imaging

All experiments presented within this thesis were conducted by using a hyper spectral imaging technique, utilizing a tunable liquid crystal filter. The concept of "spectroscopy by imaging" is illustrated in Figure 5.7.

Rayleigh scattering images in a dark-field configuration were recorded at a number of spectrally narrow intervals controlled by a tunable liquid crystal filter. The scattering spectra were then reconstructed by monitoring the intensity of a given particle as a function of wavelength. This procedure allows for parallel sampling of many isolated particles over the entire visible range and tremendously increases the throughput of single nanoparticle spectroscopy measurements (see Supporting Information, Paper I). Dark-field scattering images of nanoscale hybrid systems were recorded in this way and are shown in the top row of Figure 5.7 (for five different wavelengths 500, 560, 580, 600, and 620 nm). The displayed images are approximately 35 x 35 μm. Two representative single hybrid spectra, together with their SEM images, are furthermore shown in the figure. The first particle (on the left) exhibits a suppressed scattering at around the J-aggregate resonance wavelength; however, the mode

splitting (167 meV) does not overcome the plasmon resonance width. The second particle (on the right), on the other hand, shows much wider splitting which clearly overcomes both plasmon and molecular dissipation rates and therefore can be considered to reside in the strong coupling regime. Vacuum Rabi splitting in this case reaches about 300 meV, well above the plasmon resonance width, as shown in Figure 5.7. These two particles, and the brief analysis of their spectral differences, aim at illustrating the power of hyper spectral imaging for single particle spectroscopy.
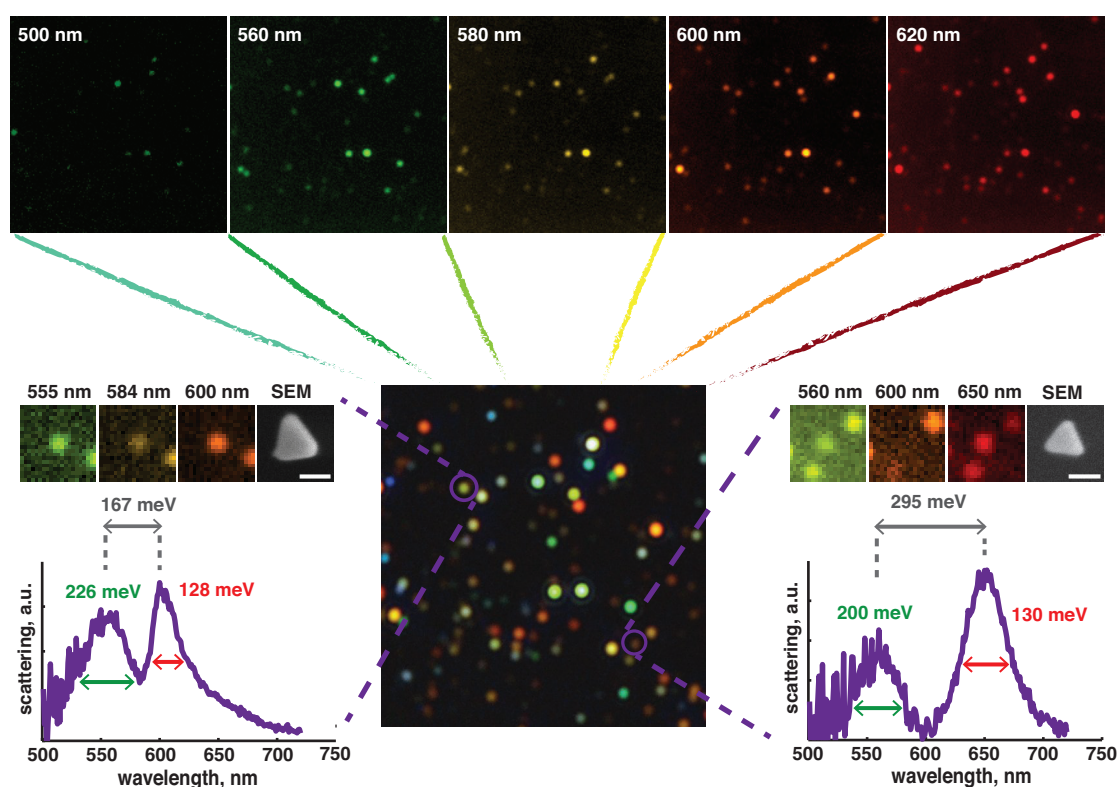

Figure 5.7. *A schematic image explaining how dark-field scattering spectra from single hybrid systems are extracted from a two-dimensional map utilizing the hyper spectral imaging concept. SEM images of the corresponding Ag nanoprisms are furthermore also displayed. Image taken from Paper I Supporting Information.*

5.3 Synthesis and sample preparations

In this section, synthesis and fabrication methodology of plasmon-exciton nanoscale hybrid systems are explicitly presented. Every step from dye-molecule J-aggregates preparation, fabrication of high crystalline silver nanoprisms and finally plasmon-exciton hybrid systems are presented and explained.

5.3.1 J-aggregates of TDBC dye-molecules

The TDBC dye molecule is comprised by a rather complicated atomic structure (5,6-Dichloro-2-   [[5,6-dichloro-1-ethyl-3-   (4-sulfobutyl)-benzimidazol-2-ylidene]-propenyl]-1-ethyl- 3-(4-sulfobutyl) benzimidazolium hydroxide, inner salt, sodium salt). The formation of J-aggregate structures from monomers occurs in solution and depends on a number of factors including dye concentration, ionic environment and pH (see Supporting Information, Paper I).

In order to optimize the conditions for stable J-aggregate formation from TDBC monomers, a concentration of 10 µM was prepared in an aqueous solution containing 5 mM of NaOH. A dry powder of TDBC monomers were simply added to the solution in a small container and stirred rigorously for a couple of seconds to ensure proper mixing. Thereafter, the solution was kept in the dark to avoid any light-induced photo-oxidation from the surrounding environment.

As described in section 3.3.6, a lowering of resonance energy is obtained when the molecules arrange themselves in a head-to-tail configuration, which gives rise to a distinct narrow spectral resonance peak located at 588 nm [93].

The measured extinction cross-section for the prepared J-aggregated TDBC dye molecules is shown in Figure 5.8.
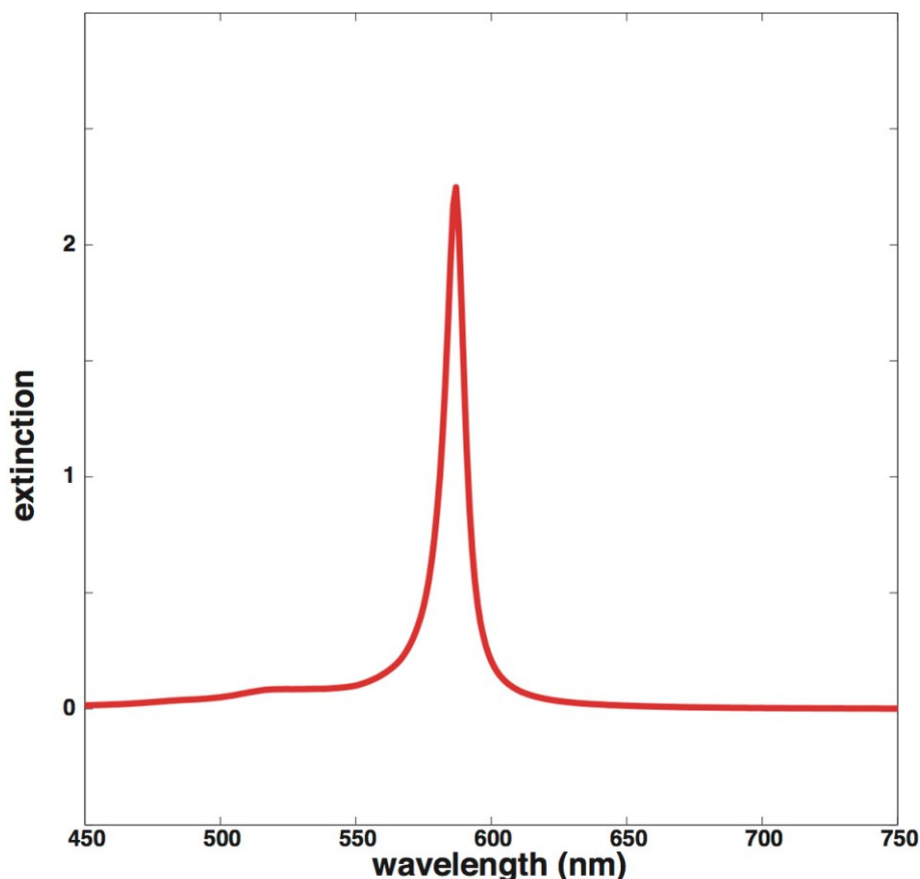
Figure 5.8. *Extinction spectrum of TDBC molecules in solution. Note the distinct J-aggregate line at 588 nm.*

5.3.2 Synthesis of high quality single crystalline Ag nanoprisms

Silver nanoprisms were synthesized according to a well-known method described in previous literature [94-96]. Here, a 3-5 nm silver seed nanoparticles solution was prepared by adding 1 mL of 30 mM trisodium citrate and 0.5 mL of 20 mM silver nitrate ($AgNO_3$) solutions to 95 mL of ice-cold ultra-pure distilled water (MilliQ). The solution was kept bubbling with N_2 under continuous stirring in the dark in contact with an ice-bath for an additional 60 min. Then, 1 mL of ice-cold 50 mM $NaBH_4$ was added into the growth solution, at which point the color of the solution turns pale-yellow. Later on, 100 μL of 50 mM $NaBH_4$ was added to the solution. This procedure was repeated 3 more times with 2 minutes break in between.

The ice-cold and freshly prepared mixture of 1 mL of 5 mM BSPP ($C_{12}H_{34}O_2$) and 1 mL of 50 mM $NaBH_4$ was added in a drop wise manner into the growth solution for seed nanoparticles. The solution was kept for 5 hours in an ice bath under gentle stirring and completed with aging overnight in an ice bath in the dark. For the photo-induced growth of silver nanoparticles, 10 mL of the aged seed solution with pH of 9.5 was irradiated with a 532 nm continuous-wave (CW) laser. The reaction was allowed to proceed for 24 hours, at

which point the silver nanoparticles were washed two times by centrifugation at 3000 rcf for 5 min, removing the supernatant solution, and re-dispersed in aqueous solution containing 0.3 mM of trisodium citrate.

Tunneling electron microscopy (TEM) images of single crystalline Ag nanoprisms, produced in the previously described synthesis, can be seen in Figure 5.9. Figure 5.9 (a) shows homogenous atomic structures, which clearly indicate that the prisms are in fact single crystalline. Figure 5.9 (b) shows stacks of prisms displaying the height distribution, which seem to be rather uniform around a value of ~ 10 nm.
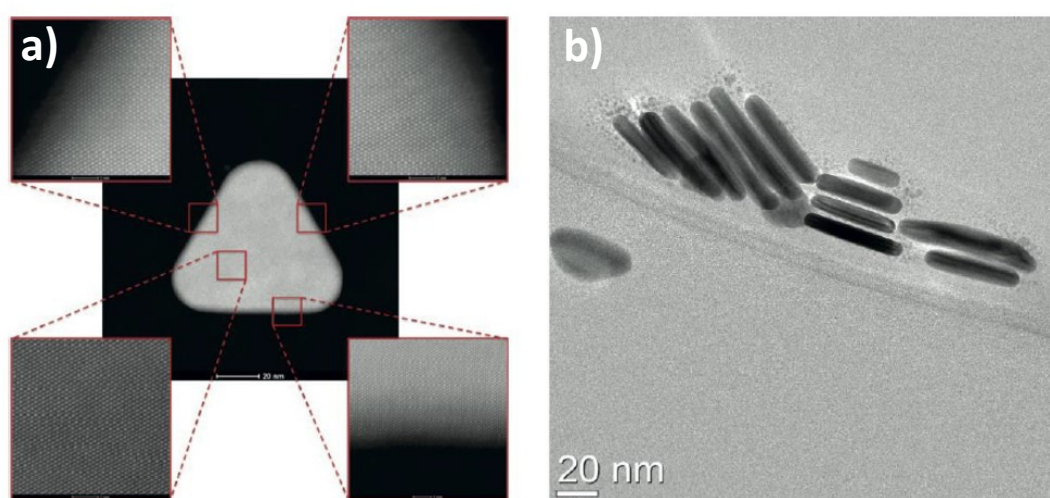

Figure 5.9. *SEM images of single crystalline Ag nanoprisms produced in the irradiation ripening synthesis. **(a)** Atomic crystal structure is visible indicating single crystallinity. **(b)** Image displaying the rather high homogeneity in height distribution between different prisms.*

5.3.3 Particle-dye hybrid sample preparation

In order to optimize the parameters for J-aggregate formation, the aqueous solution of TDBC dye was prepared at concentration of ~ 10 μM in 5 mM sodiumhydroxide (NaOH), see section 5.3.1. Furthermore, 50 μl of Ag solution was mixed with 50 μl of J-aggregate solution. The mixture was let for incubation overnight in order to get an increased probability of attachment between particle and dye-aggregates. In order to remove any free TDBC monomer or free J-aggregates, the solution was centrifuged at 5000 rcf for 5 minutes and the supernatant was replaced with purified water (MilliQ). The J-aggregate/Ag nanoparticles mixture was then applied to either TEM grids or silicon substrates with 50 nm of SiO_2 pre-coated with polylysine $(C_6H_{12}N_2O)_n$ to further improve adhesion between the particle-dye systems and the substrate. The resulting hybrid system is graphically depicted in Figure 5.10

(a) with a single-crystalline Ag nanoprism resting on top of a sheet of J-aggregated TDBC molecules. An SEM image of the actual Ag nanoprism on top of a J-aggregate sheet is shown in Figure 5.10 (b). Note that the coloring of the J-aggregate sheet is not produced by the SEM, but rather adjusted in a post-processing manner.

In the case of hybrid systems, studied and presented in Paper V, single crystalline Ag nanoprisms in a solution were drop casted on to a Si/SiO$_2$ substrate, where a monolayer flake of WS$_2$ had already been exfoliated. As in the case with Ag/J-aggregate hybrids, the substrate together with the monolayer flake was pre-coated with polylysine in order to increase adhesion between particle and monolayer. For more detailed information regarding this procedure, see Paper V.
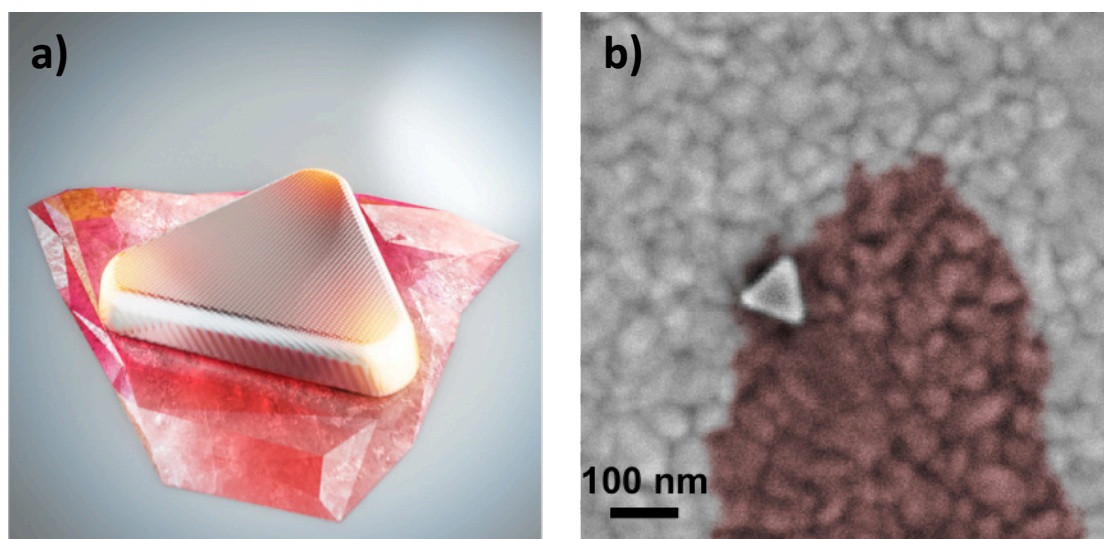

Figure 5.10. *(a) Graphical image of a hybrid structure. A single-crystalline Ag nanoprism in close contact with a sheet of J-aggregated TDBC molecules. (b) SEM image of synthesized hybrid structure on top of a continuous gold film (grainy background).*

Chapter 6

Summary and Future Outlook

In this section follows a brief summary of the content presented so far within this thesis, as well as some examples on additional systems and concepts worth investigating for future studies.

Chapter 1 gave an overall introduction to the research field of plasmonics and especially strong plasmon-exciton coupling.

Thereafter, in Chapter 2 the most basic concepts of coherence was defined and described. It was pointed out that coherence is a crucial concept not only for waves, but also for quantum states.

Later on in Chapter 3, optical resonances in both metallic nanoparticles (localized surface plasmon resonances) as well as resonances in semiconducting nanocrystals and molecules (excitons) were theoretically derived, presented and motivated. The notion and concept of treating certain excitations as quasiparticles was also presented.

In Chapter 4, interaction mechanisms between optical cavities and emitters, with notions of both weak- and strong coupling regimes, were presented and various approaches on how to view the resulting dynamics were discussed. It was furthermore shown that the implications of such interactions creates new types of excitations that cannot be treated neither as solely plasmonic nor solely excitonic entities, but rather as an inseparable mixture of both. Several different theoretical frameworks on how to describe and predict dynamics, within strongly coupled systems, were also presented and discussed. The theoretical methods presented in this thesis have been of both purely classical (coupled oscillator model), semi-classically (diagonalization of a Hamiltonian matrix with discrete energies and coupling parameters) as well as purely quantum mechanical nature (Jaynes-Cummings, Linblad Master Equation and Dicke model). Several different aspects regarding these models have been thoroughly discussed and elaborated on. Both similarities and differences of which predictable outcomes that could be drawn and derived from the different theoretical models were emphasized within this chapter.

In addition, within Chapter 4 it was demonstrated how inelastic relaxation within hybrid systems may occur due to interplay between coherent and incoherent polariton states. This

more complicated framework is crucial in order to understand deeper intrinsic dynamics within strongly coupled plasmon-exciton systems, such as how photoluminescence occurs as a result of phonon assisted energy relaxations. As previously pointed out, this chapter is the most extensive within this thesis. The reason for this is simply to give the reader as broad as possible overview on how to quantify, treat and model dynamics within nanoscale hybrid systems.

Since the vast majority of my doctoral studies have been focusing on experimental measurements, Chapter 5 was devoted to describe different experimental methodologies including optical measurement techniques, data processing, cryostat cooling, SEM imaging and fabrication of nanoscale hybrid plasmon-exciton systems.

Even though plenty of new knowledge has recently appeared within the research field of strong plasmon-exciton coupling, there is still several of work to be done on this matter. For instance, the experimental studies on which this thesis is based on have investigated nanoscale systems comprised of plasmonic cavities coupled to tens or hundreds of excitons (Paper I – Paper V). In order to reveal properties such as certain quantum effects the numbers of excitons involved in the polaritonic states must be rather restricted [24]. In addition, to reveal single photon nonlinear behaviors the system needs to be pumped with intensities drastically larger than in any of the studies we have so far conducted. Secondly, all works presented in this thesis (Paper I – Paper V) exploits coupling to excitons in molecular dyes, which are unable to sustain such high photo-radiation without being photo-inactive [97-99].

There are however alternatives routes in trying to overcome these limitations, which will be presented within the first subsection of this chapter. Moreover, further ideas on how to utilize nanoscale hybrids for temperature related controls are also presented.

6.1 Nonlinear dynamics in an optical cavity coupled to a single quantum emitter

In order to observe nonlinearities, in line with what is illustrated in Figure 4.6, systems comprised by a resonant optical cavity coupled to a single or a few quantum emitters need to be investigated [24, 25, 100]. There is still a rather big challenge to obtain single emitter hybrid systems with high enough coupling strength to overcome the dissipation rates and decoherence processes within the system. However, according to equation 4.27, with high enough transition dipole moment of the quantum emitter and sufficiently low mode volume of the plasmonic cavity one may reach a coupling strength that is adequate to enter a strong coupling regime. Similar situations have already been demonstrated experimentally [101-

102]. In such a case the energy ladder of the system would be highly dependent on the number of cavity excitations and result in nonlinear dynamics, depicted in Figure 6.1 (d).

When exploiting plasmonic cavities the excitations have a lifetime in the femtosecond range. This implies that one needs to externally excite the system with a high enough intensity source, which will result in an irradiance corresponding to more than one photon per plasmon lifetime. This will require emitters that are not sensitive to photo bleaching, for example CdSe/ZnS quantum dots (see Figure 6.1 b). By placing such emitters in a plasmonic cavity with extremely confined mode volume, one could possibly push the system to exhibit strong coupling properties. A potential system for this purpose is presented in Figure 6.1 (a). An SEM image of an initial prototype of such kind can furthermore be viewed in Figure 6.1 (c). A suitable experimental approach to reveal nonlinear dynamics within such systems would be to compare the dark-field scattering spectra obtained by the linear tungsten lamp and for instance a high-intensity white-light driven laser source. In the presence of nonlinear dynamics, as a result of strong cavity-emitter interactions, the outcome of these measurements would reveal distinct differences.
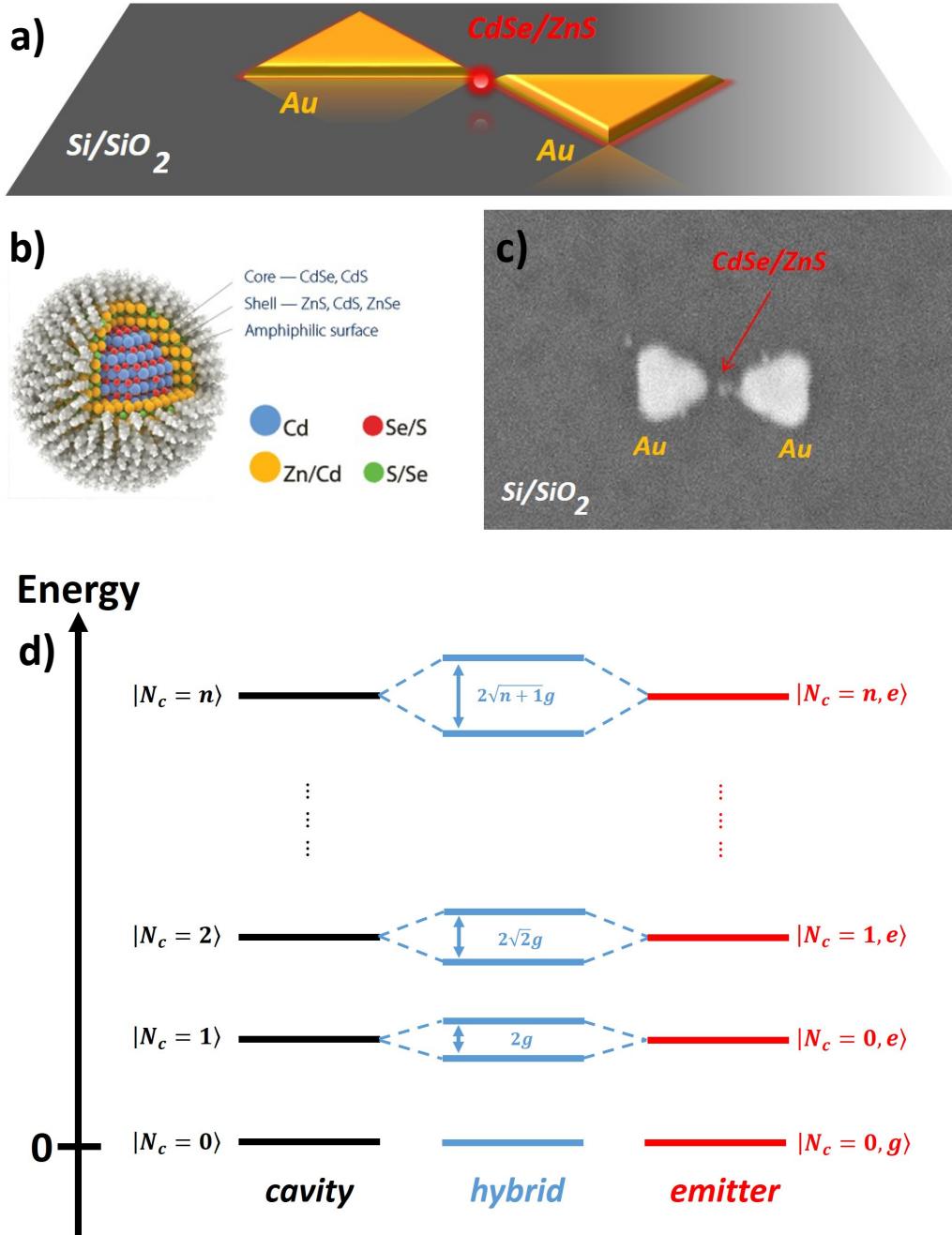
Figure 6.1. *(a) Graphic sketch of a plasmonic Au bowtie structure with a CdSe/ZnS quantum dot positioned in the hot spot region. (b) Graphic sketch of the internal structure of the quantum dot. Picture taken from [49] (c) SEM image of an actual Au bowtie structure with a CdSe/ZnS quantum dot placed in the gap. The whole structure is located on top of a Si/SiO₂ substrate. (d) Energy ladder as a result of solving eigenvalues for Jaynes-Cummings Hamiltonian in (4.27).*

6.2 Temperature controlled scattering suppression in nanoscale systems

The spectral linewidth of emission lines narrows for certain quantum emitters when the surrounding temperature is decreased [103-105]. Especially when reaching cryogenic temperatures such as liquid helium (4 K). Spectral linewidths, originating from plasmonic cavities, on the other hand aren't very much affected by alterations in temperature [106]. The plasmon-exciton coupling strength is moreover rather independent on temperature.

With all this in mind, the plasmon-exciton coupling dynamics from a semi-classical coupled-harmonic oscillator approach [23], results in a spectral dip in the scattering spectrum. This scattering suppression occurs at the spectral position of the quantum emitter emission line and may be quantified as

$$s = \frac{g}{\sqrt{\gamma_0 \gamma_c}} \tag{6.1}$$

By keeping the parameters g and γ_c constant while decreasing γ_0 sufficiently, the spectral dip parameter described in (6.1), will increase and the suppression of scattering will be very much affected. Note that the coupling parameter g can be rather weak as long as the decrease in emitter dissipation γ_0 is substantial.

Thus, it would be interesting to investigate the possibility to construct a nanoscale hybrid system, which supports temperature controlled scattering suppression in this manner. Initial studies have already been performed on a system comprised by an Au nanocube resting on top of an atomically flat continuous Au surface, with quantum dots positioned inside the gap region. Due to the presence of the Au film the out-of-plane LSPR mode will interact strongly with its mirror image, inducing a strong field-enhancement inside the gap region [107-109], and thus hopefully couple strongly to the quantum dots.

The scattering suppression effect, when lowering the emitter dissipation via for example cooling, while keeping the coupling strength and cavity dissipation constant can be seen in Figure 6.2. Observe that suppression in scattering at a certain frequency ($\omega_0 \approx 2.11$ eV, $\lambda_0 \approx$ 588 nm) will occur when the emitter dissipation rate reaches a low enough value. A realization of such a system would lead to a highly tunable hybrid system with respect to temperature, which would be interesting to investigate further.
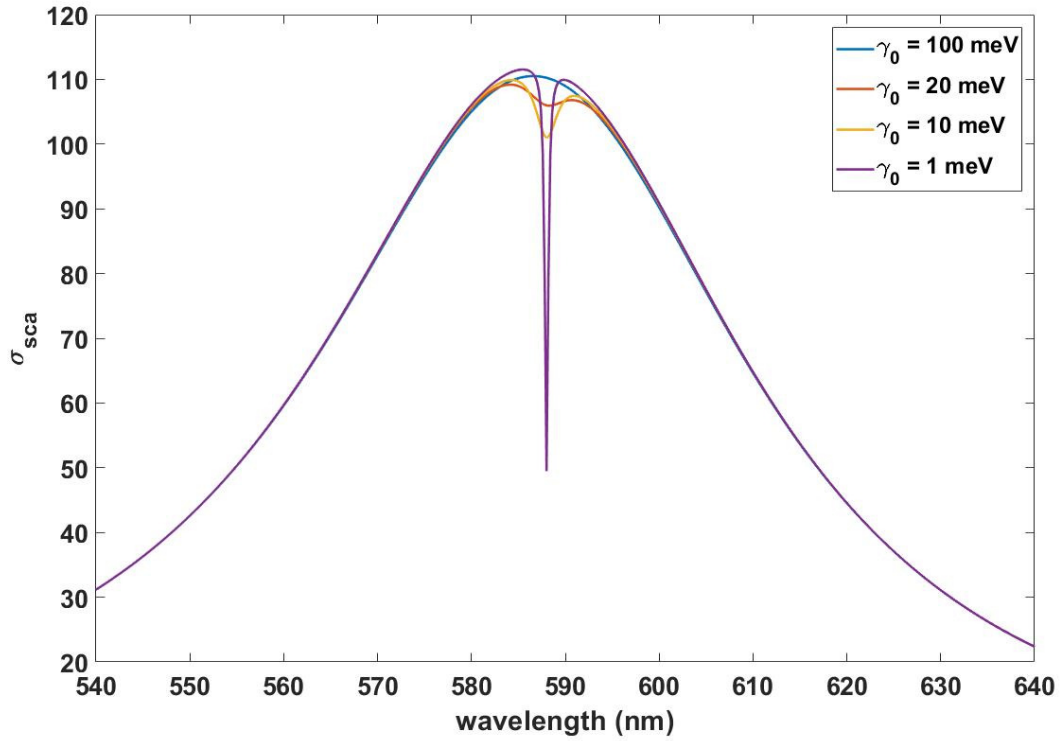
Figure 6.2. *Induced scattering transparency by altering the dissipation linewidth of the emitter. The dissipation parameter value for each curve can be seen in the legend window. The other parameters were kept constant at values of $\omega_c = \omega_0 = 2.11$ eV, $\gamma_c = 200$ meV and $g = 10$ meV.*

Acknowledgements

I would like to take the opportunity to thank several colleagues and other people, whom have been encouraging and supporting during my doctoral studies.

First and foremost, I would like to dedicate a special thank you to my supervisor Associate Professor **Timur Shegai** who has been encouraging, enthusiastic, patient and helpful throughout my entire work. You are a true source of inspiration and I am truly grateful for having had the opportunity to work with you.

- Professor **Mikael Käll**

  Thank you for being encouraging and invigorative regarding the projects, and for all material support.

- **Jorge Cuadra**

  My beloved office mate**.** Thank you for your wisdom, refined manners and your constant ability to enthuse every person around you. Also, thank you for all experimental help and nice discussions. I will forever remember our time as office mates with joy.

- **Battulga Munkhbat**

  Thank you for all nice and rewarding discussions, for all work-related and personal encouragement, for all experimental help, for all particle synthesis and for the Mongolian vodka. You are a true source of inspiration and encouragement and I am truly grateful for having had the opportunity to work with you.

- **Ankit Bisht**

  Thank you for all nice and rewarding discussions, both scientific and non-scientific. Also, thank you for always being helpful and providing nice and solid samples. It has been a pleasure working with you.

- **Michael Stührenberg**

  Mein Herr. Danke für alle netten Diskussionen und Inputs. Danke auch für die persönliche Ermutigung und Unterstützung. Es war eine wahre Freude, Sie als Kollegin zu haben.

- **Denis Baranov**

  Thank you for all rewarding discussions and help with theoretical understanding on various scientific aspects. And thank you for all brilliant graphics you provided. You have a brilliant mind and are an asset in every project you engage in.

- **Benjamin Rosseaux**

  Thank you for all nice discussions and help with theoretical understanding on strong coupling and hybrid states.

- **Adriana Canales Ramos**

  Thank you for all nice discussions and reasoning regarding strong coupling dynamics. You are a very gifted person and will have a bright future within science if you want.

- **Gülis Zengin**

  Thank you for teaching me many experimental skills. Thank you also for all fruitful discussions and inputs.

- **Ruggero Verre**

  Thank you for very nice and rewarding discussions. Thank you for always being nice, helpful, and collaborative and always providing me with nice samples.

- **Tomasz Antosiewicz**

  Thank you for your help and discussions regarding theoretical simulations of plasmon-exciton systems, and all help on general understanding of plasmon dynamics.

- **Lei Shao**

  Thank you for all help and support regarding chemistry, synthesis, experimental systems etc.

- **Sara Nilsson**

  Thank you for all help with experiments, discussions and analysis of data related to Paper I.

- **Andy Yankovich**

  Thank you so much for all your help with TEM measurements and all nice discussions.

- **Samuel Lara Avila**

  Thank you so much for all help regarding the initiation of our low-temperature measurements.

- **Stefan Gustafsson**

  Thank you for everything you provided regarding TEM measurements.

- **The Bionanophotonics Group (Jade, Pawel, Partha, Daniel, Steven, Nils, Peter, Tom, Aili, Noemi)**

  The rest of my talented and fantastic colleagues. Thank you all for fruitful and rewarding discussions and encouragement.

- My father **Claes-Johan Wersäll**

  Thank you for always being encouraging and supportive of my work. You always had a true interest for my projects even though you only comprehended small part of what I was doing. I am sad that you cannot be with us today, but I am sure that you would have made your best effort to read and enjoy this thesis.

- My mother **Margareta Wersäll**

  Thank you for being supportive and caring throughout my entire life, and also for trying to understand my research field. I do think you understand more than you think yourself but some concepts need time to grow, and we still have some time to discuss certain aspects.

Martin Wersäll

Göteborg, Sweden, July 3 2018

Bibliography

[1]   J. Weiner & F. Nunes, *Light-Matter Interaction: Physics and Engineering at the Nanoscale*. Oxford: Oxford University Press **2012**.

[2]   Y. R. Shen, *Principles of Non-linear Optics*. New York: Wiley-Interscience **1984**.

[3]   E. F. Schubert, T. Gessmann, and J. K. Kim, *Light-Emitting Diodes*. New York: Kirk-Othmer Encyclopedia of Chemical Technology **2005**.

[4]   J. Nelson, *The Physics of Solar Cells*. London: Imperial College Press **2003**.

[5]   J. Faye, *Copenhagen Interpretation of Quantum Mechanics*. Stanford: Stanford Encyclopedia of Philosophy **2014**.

[6]   L. Vaidman, *Many-Worlds Interpretation of Quantum Mechanics*. Stanford: Stanford Encyclopedia of Philosophy **2015**.

[7]   E. Hecht, *Optics: 4th Edition*. Boston: Addison-Wesley **2001**.

[8]   L. Novotny & B. Hecht, *Principles of Nano-Optics*. New York: Cambridge University Press **2006**.

[9]   C. Bohren & D. Huffman, *Absorption and Scattering of Light by Small Particles*. New York: John Wiley & Sons **1998**.

[10] N. J. Halas, *Plasmonics: An Emerging Field Fostered by Nano Letters*. Nano Lett. **2010**, 10, 3816-3822.

[11] C. Chang, C. Yang, Y. Liu, P. Tao, C. Song, W. Shang, J. Wu, and T. Deng, *Efficient Solar-Thermal Energy Harvest Driven by Interfacial Plasmonic Heating-Assisted Evaporation*. ACS Appl. Mater. Interfaces **2016**, 8, 35, 23412-23418.

[12] T. Shegai, M. Svedendahl, S. Chen, A. Dahlin, M. Käll, *Nanoantennas for Refractive Index Sensing*, In: M. Agio & A. Alù, *Optical Antennas*. New York: Cambridge University Press **2013**, p. 340-356.

[13] S. Lal, S. Link, and N. J. Halas, *Nano-Optics from Sensing to Waveguiding*. Nat. Photonics **2007**, 1, 641-648.

[14] C. Vieu, F. Carcenac, A. Pépin, Y. Chen, M. Mejias, A. Lebib, L. Manin-Ferlazzo, L. Couraud, and H. Launois, *Electron Beam Lithography: Resolution Limits and Applications*. Appl. Surf. Sci. **2000**, 164, 111-117.

[15] H. Fredriksson, Y. Alaverdyan, A. Dmitriev, C. Langhammer, D. S. Sutherland, M. Zäch, and B. Kasemo, *Hole-Mask Colloidal Lithography*, Adv. Mat. **2007**, 19, 4297-4302.

[16] P. G. Martínez-Torres, Monica Monserrat Martínez-García, P. E. Cardoso-Ávila, and J. L. Pichardo-Molina, *Facile Nanostructured Substrate Preparation Using Gold Nanocuboids for SERS*. Nanomat. and Nanotech., **2015**, 5:12.

[17] E. Cao, W. Lin, M. Sun, W. Liang, and Y. Song, *Exciton-Plasmon Coupling Interactions: From Principle to Applications*. Nanophotonics, **2018**, 7(1): 145-167.

[18] E. M. Purcell, H. C. Torrey, and R. V. Pound, *Resonance Absorption by Nuclear Magnetic Moments in a Solid*. Phys. Rev. **1946**, 69, 37.

[19] S. Balci, *Ultrastrong Plasmon-Exciton Coupling in Metal Nanoprisms with J-aggregates*. Opt. Lett. **2013**, 38, 4498.

[20] A. I. Väkeväinen, R. J. Moerland, H. T. Rekola, A. P. Eskelinen, J. P. Martikainen, D. H. Kim, and P. Törmä, *Plasmonic Surface Lattice Resonances at the Strong Coupling Regime*. Nano Lett. **2014**, 14 (4), pp 1721-1727.

[21] W. Ni, T. Ambjörnsson, S. P. Apell, H. Chen, and J. Wang, *Observing Plasmonic-Molecular Resonance Coupling on Single Gold Nanorods*. Nano Lett. **2010**, 10, 77.

[22] A. E. Schlather, N. Large, A. S. Urban, P. Nordlander, and N. J. Halas, *Near-Field Mediated Plexcitonic Coupling and Giant Rabi Splitting in Individual Metallic Dimers*. Nano Lett. **2013**, 13, 7, 3281-3286.

[23] G. Zengin, G. Johansson, P. Johansson, T. J. Antosiewicz, M. Käll, and T. Shegai, *Approaching the Strong Coupling Limit in Single Plasmonic Nanorods Interacting with J-aggregates*. Sci. Rep. **2013**, 3, 3074.

[24] K. Hennessy, A. Badolato, M. Winger, D. Gerace, M. Atatüre, S. Gulde, S. Fält, E. L. Hu, and A. Imamoglu, *Quantum Nature of a Strongly Coupled Single Quantum Dot-Cavity System*. Nature (London) **2007**, 445, 896.

[25] A. Faraon, I. Fushman, D. Englund, N. Stoltz, P. Petroff, and J. Vukovic, *Coherent Generation of Non-Classical Light on a Chip via Photon-Induced Tunnelling and Blockade*. Nat. Phys. **2008**, 4, 859.

[26] X. Wu, S. K. Gray, and M. Pelton, *Quantum-Dot-Induced Transparency in a Nanoscale Plasmonic Resonator*. Opt. Express **2010**, 18, 23633.

[27] S. Savasta, R. Saija, A. Ridolfo, O. Di Stefano, P. Denti, and F. Borghese, *Nanopolaritons: Vacuum Rabi Splitting with a Single Quantum Dot in the Center of a Dimer Nanoantenna*. ACS Nano **2010**, 4, 6369.

[28] A. Imamoglu, D. D. Awschalom, G. Burkard, D. P. DiVincenzo, D. Loss, M. Sherwin, and A. Small, *Quantum Information Processing Using Quantum Dot Spins and Cavity QED*. Phys. Rev. Lett. **1999**, 83, 4204.

[29] G. Kithrova, H. M. Gibbs, M. Kira, S. W. Koch, and A. Scherer, *Vacuum Rabi Splitting in Semiconductors*. Nat. Phys. **2006**, 2, 81.

[30] D. E. Chang, V. Vuletic, and M. D. Lukin, *Quantum Nonlinear Optics – Photon by Photon*. Nat. Phot. **2014**, 8, 685.

[31] H. –K. Lo and H. F. Chau, *Unconditional Security of Quantum Key Distribution over Arbitrarily Long Distances*. Science **1999**, 283, 2050.

[32] T. Volz, A. Reinhard, M. Winger, A. Badolato, K. J. Hennessy, E. L. Hu, and A. Imamoglu, *Ultrafsat All-Optical Switching by Single Photons*. Nat. Phot. **2012**, 6, 605.

[33] Online Etymology Dictionary, www.etymonline.com, **2001-2015**.

[34]   R. G. Driggers, *Encyclopedia of Optical Engineering*. Florida: CRC Press, **2003**.

[35] J. J. Sakurai and J. Napolitano, *Modern Quantum Mechanics 2nd Edition*. Cambridge: Cambridge University Press, **2017**.

[36] M. Schlosshauer, *Decoherence, the Measurement Problem, and Interpretations of Quantum Mechanics*. arXiv **2005**, arXiv:quant-ph/0312059v4

[37] O. Penrose and L. Onsager, *Bose-Einstein Condensation and Liquid Helium*. Phys. Rev. **1956**, 104, 576.

[38] N. W. Ashcroft and N. D. Mermin, *Solid State Physics*. Boston: Cengage Learning, **1976**.

[39] M. Meier and A. Wokaun, *Enhanced Fields on Large Metal Particles: Dynamic Depolarization*. Opt. Lett., **1983**, 8, 11.

[40] V. D. Miljkovic, T. Pakizeh, B. Sepulveda, P. Johansson, and M. Käll, *Optical Forces in Nanoparticle Dimers*. J. Phys. Chem. C, **2010**, 114, 7472-7479.

[41] P. Pavaskar, J. Theiss, and S. B. Cronin, *Plasmonic Hot Spots: Nanogap Enhancement vs. Focusing Effects from , Nanoparticles*. Opt. Exp. **2012**, 20, 13, 14656-14662.

[42] I. Freestone, N. Meeks, M. Sax, and C. Higgitt, *The Lycurgus Cup – A Roman Nanotechnology*. Gold Bulletin **2007**, 40/4.

[43] B. H. Bransden and C. J. Joachain, *Physics of Atoms and Molecules: 2nd Edition*. Harlow: Pearson Education Limited **2003**.

[44] D. Bera, L. Qian, T. Tseng, and P. H. Holloway, *Quantum Dots and Their Multimodal Applications: A Review*. Materials, **2010**, 3, 2260-2345.

[45] A. Imamoglu, R. J. Ram, S. Pau, and Y. Yamamoto, *Nonequilibrium Condensates and Lasers without Inversion: Exciton-Polariton Lasers*. Phys. Rev. A, **1996**, 53, 4250.

[46] R. S. Knox, *Theory of Excitons*. New York: Academic Press, **1963**.

[47] M. D. Leistikow, J. Johansen, A. J. Kettelarij, P. Lodahl, and W. L. Vos, *Size-Dependent Oscillator Strength and Quantum Efficiency of CdSe Quantum Dots Controlled vi the Local Density of States*. Phys. Rev. B, **2009**, 79, 045301.

[48] K. F. Mak, K. He, C. Lee, G. H. Lee, J. Hone, T. F. Heinz, and J. Shan, *Tightly Bound Trions in Monolayer MoS$_2$*. Nat. Mater. **2013**, 12 (3), 207-211.

[49] Tao Patch, Human Upgrade Device, www.taopatch.com

[50] PlasmaChem, www.plasmachem.com

[51] S. Rudin and T. L. Reinecke, *Size Effects in the Temperature Dependence of Exciton Linewidths*. Phys. Stat. Sol. **2002**, 190 (3), 677-681.

[52] Y. Wang, *Resonant Third-Order Optical Nonlinearity of Molecular Aggregates with Low-Dimensional Excitons*, JOSA B. **1991**, 981-985.

[53] M. Van Burgel, D. A. Wiersma, and K. Duppen, *The dynamics of One-Dimensional Excitons in Liquids*. J. Chem. Phys. **1995**, 102, 20-33.

[54] M. Kasha, H. Rawls, and M. El-Bayoumi, *The Exciton Model in Molecular Spectroscopy*. Pure Appl. Chem. **1965**, 11 (3-4), 371-392.

[55] C. C. Gerry & P. L. Knight, *Introductory Quantum Optics*. New York: Cambridge University Press, **2005**.

[56] M. O. Scully and M. S. Zubiary, *Quantum Optics*. Cambridge: Cambridge University Press, **1997**.

[57] E. M. Purcell, *Spontaneous Emission Probabilities at Radio Frequencies*. Phys. Rev. **1946**, 69, 681.

[58] A. González-Tudela, P. A. Huidobro, L. Martín-Moreno, C. Tejedor, and F. J. García-Vidal, *Theory of Strong Coupling between Quantum Emitters and Propagating Surface Plasmons*. Phys. Rev. Lett. **2013**, 110, 126801.

[59] D. G. Baranov, M. Wersäll, J. Cuadra, T. J. Antosiewicz, and T. Shegai, *Novel Nanostructures and Materials for Strong Light-Matter Interactions*. ACS Photonics **2018**, 5 (1), 24-42.

[60] E. T. Jaynes and F. W. Cummings, *Comparison of Quantum and Semiclassical Radiation Theories with Application to the Beam Maser*. Proc. IEEE **1963**, 51, 1, 89-109.

[61] S. A. Maier, *Optical and Quantum Electronics*. New York: Springer Publishing, **2006**.

[62] J. M. Torres, *Closed-Form Solution of Lindblad Master Equation without Gain*. Phys. Rev. A, **2014**, 89, 052133.

[63] B. M. Garraway, *The Dicke Model in Quantum Optics: Dicke Model Revisited*. Philosophical Transactions of the Roayal Society A, **2011**, 369, 1137-1155.

[64] T. J. Antosiewicz, S. P. Apell, and T. Shegai, *Plasmon-Exciton Interactions in a Core-Shell Geometry: From Enhanced Absorption to Strong Coupling*. ACS Photonics, **2014**, 1 (5), 454-463.

[65] Y. Akutagawa, K. Miyasue, T. Sekiya, S. Kurita, M. Nakajima, and T. Suemoto, *Time Resolved Response of Photoluminescence on Cyanine Dye J-aggregates*. Phys. Stat. Sol. **2006**, 10, 3404-3407.

[66] D. Melnikau, R. Estaban, D. Savateeva, A. Sánchez-Iglesias, M. Grzelczak, M. K. Schmidt, L. Liz- Marzán, J. Aizpurua, and Y. P. Rakovich, *Rabi Splitting in Photoluminescence Spectra of Hybrid Systems of Gold Nanorods and J-aggregates*. J. Phys. Chem. Lett. **2016**, 7 (2), 354-362.

[67] S. Wang, T. Chervy, J. George, J. A. Hutchison, C. Genet, and T. W. Ebbesen, *Quantum Yield of Polariton Emission from Hybrid Light-Matter States*. J. Phys. Chem. Lett. **2014**, 5 (8), 1433-1439.

[68] J. George, S. Wang, T. Chervy, A. Canaquier-Durand, G. Schaeffer, J.-M. Lehn, J. A. Hutchison, C. Genet, and T. W. Ebbesen, *Ultra-Strong Coupling of Molecular Materials: Spectroscopy and Dynamics*. Faraday Discuss. **2015**, 178 (0), 281-294.

[69] M. Litinskaya, P. Reineker, and V. M. Agranovich, *Fast Polariton Relaxation in Strongly Coupled Organic Microcavities*. J. Lumin. **2004**, 110 (4), 364-372.

[70] M. Litinskaya, P. Reineker, and V. M. Agranovich, *Exciton-Polaritons in Organic Microcavities*. J. Lumin. **2006**, 119-120, 277-282.

[71] V. M. Agranovich, M. Litinskaya, D. G. Lidzey, *Cavity Polaritons in Microcavities Containing Disordered Organic Semiconductors*. Phys. Rev. B **2003**, 67, 085311.

[72] P. Scherer & S. F. Fischer, *Theoretical Molecular Biophysics*. Berlin, Heidelberg: Springer-Verlag, **2010**.

[73] D. M. Coles, A. J. H. M. Meier, W. C. Tsoi, M. D. B. Charlton, J.-S. Kim, and D. G. Lidzey, *A Characterization of the Raman Modes in a J-aggregate Forming Dye: A Comparison between Theory and Experiment*. J. Phys. Chem. A **2010**, 114, 11920-11927.

[74] F. Herrera & F. C. Spano, *Dark Vibronic Polaritons and the Spectroscopy of Organic Microcavities*. Phys. Rev. Lett. **2017**, 118, 223601.

[75] A. Thomas, J. George, A. Shalabney, M. Dryzhakow, S. J. Varma, J. Moran, T. Chervy, X. Zhong, E. Devaux, C. Genet, J. A. Hutchison, and T. W. Ebbesen, *Ground-State Chemical Reactivity under Vibrational Coupling to the Vacuum Electromagnetic Field*. Angew. Chem. Int. Ed. Engl. **2016**, 55 (38), 11462.

[76] J. A. Hutchison, T. Schwarz, C. Genet, E. Devaux, and T. W. Ebbesen, *Modifying Chemical Landscapes by Coupling to Vacuum Fields*. Angew. Chem. Int. Ed. Engl. **2012**, 51, 1592.

[77] P. Vasa, R. Pomraenke, G. Cirmi, E. De Re, W. Wang, S. Schwieger, D. Leipold, E. Runge, G. Cerullo, and C. Lienau, *Ultrafast Manipulation of Strong Coupling in Metal-Molecular Aggregate Hybrid Nanostructures*. ACS Nano **2010**, 4 (12), 7559-7565.

[78] P. Vasa, W. Wang, R. Pomraenke, M. Lammers, M. Maiuri, C. Manzoni, G. Cerullo, and C. Lienau, *Real-time Observation of Ultrafast Rabi Oscillations between Excitons and Plasmons in Metal Nanostructures with J-aggregates*. Nat. Phot. **2013**, 7 (2), 128-132.

[79] S. R. K. Rodruigez, J. Feist, M. A. Verschuuren, F. J. Garcia-Vidal, and J. Gómez-Rivas, *Thermalization and Cooling of Plasmon-Exciton Polaritons: Towards Quantum Condensation*. Phys. Rev. Lett. **2013**, 111, 166802.

[80] M. Ramezani, A. Halpin, A. I. Fernández-Domínguez, J. Feist, S. R.-K. Rodruigez, F. J. Garcia-Vidal, and J. Gómez-Rivas, *Plasmon-Exciton-Polariton Lasing*. Optica **2017**, 4 (1), 31-37.

[81] V. Pilla, L. P. Alves, J. F. de Santana, L. G. da Silva, R. Ruggiero, and E. Munin, *Fluorescence Quantum Efficiency of CdSe/ZnS Quantum Dots Embedded in Biofluids: pH Dependence*. J. Appl. Phys. **2012**, 112, 104704.

[82] F. Träger, *Springer Handbook of Lasers and Optics*. Berlin, Heidelberg: Springer-Verlag, **2012**.

[83] J. W. Lichtman & J. −A. Conchello, *Fluorescence Microscopy*. Nat. Methods **2005**, 2, 910-919.

[84] G. Baryshnikov, B. Minaev, and H. Ågren, *Theory and Calculation of the Phosphorescence Phenomenon*. Chem. Rev. **2017**, 117, 6500-6537.

[85] M. Bixon & J. Jortner, *Intramolecular Radiationless Transitions*. J. Chem. Phys. **1968**, 48, 715-726.

[86] T. Sato, R. Hayashi, N. Haruta, and Y. -J. Pu, *Fluorescence via Reverse Intersystem Crossing from Higher Triplet States in a Bisanthracene Derivative*. Sci. Rep. **2017**, 7, 4820.

[87] H. Szmacinski & J. R. Lakowicz, *Fluorescence Lifetime-Based Sensing and Imaging*. Sensors and Actuators B, **1995**, 29, 16-24.

[88] M. Y. Berezin & S. Achilefu, *Fluorescence Lifetime Measurements and Biological Imaging*. Chem. Rev. **2010**, 110, 2641-2684.

[89] J. C. D. Brand, *Lines of Light: The Sources of Dispersive Spectroscopy 1800-1930*. Philadelphia: Gordon and Breach Science Publishers, **1995**.

[90] J. Beeckman, K. Neyts, and P. J. M. Vanbrabant, *Liquid-Crystal Photonic Applications*. Opt. Eng. **2011**, 50 (8), 081202.

[91] G. A. Kopp, *Tunable Birefringent Filters Using Liquid Crystal Variable Retarders*. Polariz. Anal. Meas. **1994**, 193, 193.201.

[92] H. R. Morris, C. C. Hoyt, and P. J. Treado, *Imaging Spectrometers for Fluorescence and Raman Microscopy: Acousto-Optic and Liquid Crystal Tunable Filters*. Appl. Spec. **1994**, 48, 7.

[93] K. Takatori, T. Okamoto, K. Ishibashi, and R. Micheletto, *Surface Exciton Polaritons Supported by a J-aggregate-Dye/Air Interface at Room Temperature*. Opt. Lett. **2017**, 42, 19.

[94] J. Zhang, M. R. Langille, and C. A. Mirkin, *Photomediated Synthesis of Silver Triangular Bipyramids and Prisms: The Effect of pH and BSPP*. J. Am. Chem. Soc. **2010**, 132 (35), 12502-12510.

[95] G. S. Métraux and C. A. Mirkin, *Rapid Thermal Synthesis of Silver Nanoprisms with Chemically Tailorable Thickness*. Adv. Mater. **2005**, 17, 4.

[96] R. Jin, Y. Cao, C. A. Mirkin, K. L. Kelley, G. C. Schatz, and J. G. Zheng, *Photoinduced Conversion of Silver Nanospheres to Nanoprisms*. Science **2001**, 294, 5548, 1901-1903.

[97] E. K. L. Yeow, S. M. Melnikov, T. D. M. Bell, F. C. De Schryver, and J. Hofkens, *Characterizing the Fluorescence Intermittency and Photobleaching Kinetics of Dye Molecules Immobilized on a Glass Surface*. J. Phys. Chem. A. **2006**, 110, 1726-1734.

[98] C. Eggeling, J. Widengren, R. Rigler, and C. A. M. Seidel, *Photobleaching of Fluorescent Dyes under Conditions Used for Single-Molecule Detection: Evidence of Two-Step Photolysis*. Anal. Chem. **1998**, 70, 2651-2659.

[99] A. Renn, J. Seelig, and V. Sandoghdar, *Oxygen-Dependent Photochemistry of Fluorescent Dyes Studied at the Single Molecule Level*. Mol. Phys. **2006**, 104, 3, 409-414.

[100] S. Gröblacher, T. Paterek, R. Kaltenbaek, C. Brukner, M. Zukowski, M. Aspelmeyer, and A. Zeilinger, *An Experimental Test of Non-Local Realism*. Nature (London) **2007**, 446, 871.

[101] R. Chikkaraddy, B. de Nijs, F. Benz, S. J. Barrow, O. A. Scherman, E. Rosta, A. Demetriadou, P. Fox, O. Hess, and J. J. Baumberg, *Single-Molecule Strong Coupling at Room Temperature in Plasmonic Nanocavities*. Nature **2016**, 535, 127-130.

[102] K. Santosh, O. Bitton, L. Chuntonov, and G. Haran, *Vacuum Rabi Splitting in a Plasmonic Cavity at the Single Quantum Emitter Limit. Nat.* Commun. **2016**, 7, 11823.

[103] W. Ouerghui, A. Melliti, M. A. Maaref, and J. Bloch, *Dependence on Temperature of Homogeneous Broadening of InGaAs/InAs/GaAs Quantum Dot Fundamental Transitions*. Physica E **2005**, 519-524.

[104] I. Sychugov, R. Juhasz, J. Valenta, and J. Linnros, *Narrow Luminescence of a Silicon Quantum Dot*. Phys. Rev. Lett. **2005**, 94, 087405.

[105] M. Bayer & A. Forchel, *Temperature Dependence of the Exciton Homogeneous Linewidth in $In_{0.60}Ga_{0.40}As/GaAs$ Self-Assembled Quantum Dots*. Phys. Rev. B **2002**, 65, 041308.

[106] M. Liu, M. Pelton, and P. Guyot-Sionnest, *Reduced Damping of Surface Plasmons at Low Temperatures*. Phys. Rev. B **2009**, 79, 035418.

[107] J. J. Mock, R. T. Hill, A. Degiron, S. Zauscher, A. Chilkoti, and D. R. Smith, *Distance-Dependent Plasmon Resonant Coupling between a Gold Nanoparticle and a Gold Film*. Nano Lett. **2008**, 8 (8), 2245-2252.

[108] M. Hu, A. Ghoshal, M. Marquez, and P. G. Kik, *Single Particle Spectroscopy of Metal-Film-Induced Tuning of Silver Nanoparticle Plasmon Resonances*. J. Phys. Chem. C **2010**, 114, 7509-7514.

[109] F. Le, N. Z. Lwin, J. M. Steele, M. Käll, N. J. Halas, and P. Nordlander, *Plasmons in the Metallic Nanoparticle-Film System as a Tunable Impurity Problem*. Nano Lett. 2005, 5 (10), **2009**-2013.